Title
Hybrid Simulation of Corroded Hybrid Fiber Reinforced Concrete Structures Exposed to Seismic Loading

Permalink
https://escholarship.org/uc/item/6k8475jq

Author
Duncan, Jacob Fuller

Publication Date
2019

Peer reviewed|Thesis/dissertation

Hybrid Simulation of Corroded Hybrid Fiber Reinforced Concrete Structures Exposed to
Seismic Loading

by

Jacob Fuller Duncan

A dissertation submitted in partial satisfaction of the

requirements for the degree of

Doctor of Philosophy

in

Engineering - Civil and Environmental Engineering

in the

Graduate Division

of the

University of California, Berkeley

Committee in charge:

Professor Claudia P. Ostertag, Chair
Professor Paulo J.M. Monteiro
Assistant Professor Hayden Taylor

Summer 2019

Hybrid Simulation of Corroded Hybrid Fiber Reinforced Concrete Structures Exposed to
Seismic Loading

Copyright ©2019

by

Jacob Fuller Duncan

Abstract

Hybrid Simulation of Corroded Hybrid Fiber Reinforced Concrete Structures Exposed to
Seismic Loading

by

Jacob Fuller Duncan

Doctor of Philosophy in Engineering - Civil and Environmental Engineering

University of California, Berkeley

Professor Claudia P. Ostertag, Chair

Given the state of aging infrastructure in the United States, reinforcement corrosion is proving to be costly in direct maintenance and replacement costs, as well as indirect costs, such as traffic delays and loss of productivity. Seismicity complicates this issue due to the looming threat of extreme loading on the heavily-used bridge structures that connect our communities. It is important to understand mechanisms of corrosion damage and their impacts on structural behavior in order to ensure that future repairs and new designs are sustainable, long-term solutions. The research presented in this dissertation investigates the combined action of corrosion and seismic loading on bridge columns. Fiber reinforcement is proposed as a means of extending the service life of reinforced concrete components and providing resistance to damage from environmental and mechanical action. Hybrid Fiber Reinforced Concrete (HyFRC) and its self-consolidating variant, SC-HyFRC, were utilized in these experiments to investigate their durability against the expansion of corrosion products and their ductility during mechanical loading. Of specific interest in this research is the intersection between corrosion damage in reinforced concrete and HyFRC column elements and mechanical behavior under seismic loading.

Steel reinforced self-consolidating concrete (SCC) and SC-HyFRC columns are exposed to corrosion damage through long term exposure in a chloride-contaminated environment, in which 2% chloride by weight of binder materials was admixed when column elements were cast to investigate the corrosion propagation phase in isolation. Corrosion rate and surface cracking behavior was monitored during a 125-week corrosion exposure period. Mechanical behavior was then investigated through compressive testing of corrosion-damaged column elements and tensile testing of corroded reinforcing steel. While the SC-HyFRC clearly exhibited less corrosion damage compared to the SCC control specimen, the large difference in compressive strength between the SC-HyFRC and SCC implies that a difference in their matrix/rebar interfaces made a comparison in their crack propagation behavior less conclusive.

Hybrid Simulation (HS) is utilized to investigate the system-level seismic performance of reinforced concrete structures with corrosion damaged components. This technique combines physical testing with computer simulation to impose realistic, dynamic loading conditions on a physically manageable test-specimen. An HS test procedure was developed to investigate the seismic behavior of a single-column highway bridge, where the lower portion of the column serves as the experimental element. The setup was validated and calibrated using a steel hollow structural

section (HSS) column element. The HS procedure was also utilized with reinforced concrete and HyFRC column elements that were exposed to an applied current to accelerate corrosion damage prior to testing. HyFRC columns were more effective at preventing spalling as well as retaining their stiffness following severe seismic damage, even with pre-existing corrosion damage.

Many reinforced concrete bridges are simultaneously exposed to the combined hazard of seismicity and corrosion damage. It is of great importance to improve the understanding of existing infrastructure so that we can develop efficient and long-lasting repair or replacement strategies to keep communities safe while more effectively utilizing innovative materials to extend the service lives of structures. HS improves accuracy by incorporating the true behavior of a physical specimen into a numerical model to capture the full response of the structure, even if some components are difficult to explicitly model. This also increases efficiency of experimental testing as a large portion of the structure can remain as a computational model, eliminating the need perform expensive system-level tests.

Table of Contents

List of Figures

List of Tables

Acknowledgements

To my advisor, Professor Claudia Ostertag, thank you for your unending support and guidance through the curve balls that both research and life have thrown at me. Thank you for allowing me to explore new research areas and helping me to see the bigger picture in my all my experiments.

To the members of my dissertation committee, Professors Paulo Monteiro and Hayden Taylor, thank you for working with my aggressive schedule. Your feedback and support were greatly appreciated, and certainly improved the quality of this dissertation.

To my family and friends, thank you for all your love and support. I couldn't have accomplished this without your encouragement. A special thank you to my parents for all the help along the way.

To Wilson Nguyen, Ian Williams, Parham Aghdasi, Gabe Jen, Alex Lin, Rotana Hay, Daniela Martinez, Jiaqi Li, Rae Taylor, Miklos Zoller, George Greer, Fayad Rahman, Donovan Llanes, and countless others who made my graduate school experience such an exciting and fulfilling ride. I couldn't have asked for a more supportive group of colleagues/friends/labmates/mentors. Thanks for all your advice throughout grad school and helping me stay motivated and on track.

To the Davis Hall staff: Matt Cataleta, Cruz Carlos, Phil Wong, Llyr Griffith, Shakhzod Takhirov, Jacqueline Garcia, Negassi Hagdu, Jeff Higginbotham, Shelley Okimoto and the entire AAO. Thank you for your friendship and guidance and for helping me clean up my messes (both literal and figurative).

To Selim Gunay and Andreas Schellenberg, a huge thanks for all your help with the Hybrid Simulation experiments and the writing that went into this dissertation. An additional thank you to Ian Williams for his contributions to these experiments.

To the wonderful undergraduate research assistants, including Jackson Le, Vanessa Ibarra, German Perea, Andy Jung, Jalen Loche, Christian Chung, Tamika Bassman and Brian Tam, who went above and beyond to make this research a reality, thank you so much for your contributions and I hope you gained at least as much as you put in!

And last but certainly not least, to my lovely wife, thank you for putting up with all the late nights, supporting me in all aspects of my life, keeping me focused when I had a deadline, and distracting me when I needed a break.

1 Introduction

Corrosion of embedded steel in reinforced concrete (RC) impacts the sustainability of infrastructure systems by reducing service life and increasing maintenance costs of structures around the world. The formation of expansive corrosion products leads to cracking and spalling of the concrete cover, ultimately exposing reinforcement to the environment and increasing the risk for further corrosion damage. Bridge structures are particularly susceptible to corrosion damage due to their exposure to salt spray in marine environments and deicing salt in regions where roadways freeze. This risk is compounded in seismic regions, as the behavior of these deteriorated structures is not well-understood, yet bridges serve as critical infrastructure for emergency services following a disaster such as an earthquake. As we move to rebuild, repair and retrofit our aging infrastructure, we have an opportunity to incorporate innovative materials and implement improved modeling and simulation techniques to increase service life and better understand seismic performance of the built environment. These innovations will allow engineers to provide the public with safer and more sustainable infrastructure.

1.1 Reinforced Concrete Infrastructure in the United States

The United States Federal Highway Administration (FHWA) collects and reports data on the more than 616,000 highway bridges in the United States, of which, over 417,000 (67.7%) are supported by either conventional reinforced concrete or prestressed concrete (PSC) superstructures. If any bridge with at least one major concrete component is considered (deck, superstructure or approach structures), this figure jumps to over 545,150 (88.5%) (NBI 2018). These bridge structures hold together the critical arterial network that serves as the foundation of a safe and economically prosperous society. Given their importance, bridge structures are inspected every other year, with all data compiled annually in the National Bridge Inventory (NBI). Data from the 2018 NBI reveals that the average age of a bridge structure in the United States is 43.2 years, which brings concern given that many of these structures were designed with an intended service life not exceeding 50 years. In many structures, advanced age and deferred maintenance have brought about deterioration. Based on the 2018 NBI report, 7.6% percent are of bridges are rated as "Structurally Deficient," meaning that at least one component of the bridge is determined to be in "Poor" condition and that the structure must either be repaired or replaced. Table 1 - 1 shows the NBI condition assessment for all bridges in 2012, 2015 and 2018.

Table 1 - 1: National highway bridge count by condition, 2012-2018 (NBI 2018).

Year	All	Good	Fair	Poor
2012	607,380	287,194 (47.3%)	262,878 (43.3%)	57,049 (9.4%)
2015	611,845	289,158 (47.3%)	271,690 (44.4%)	50,917 (8.3%)
2018	616,096	283,316 (46.0%)	285,676 (46.4%)	47,054 (7.6%)

While the number of deficient bridges has declined in recent years, it should be noted that the number of bridges in the 'Fair' condition category is steadily rising and that in 2018, the number of 'Fair' bridges in the U.S. passed the number of bridges in 'Good' condition. While these bridges do not require immediate action, they do demonstrate observable damage and will inevitably become the next wave of 'Structurally Deficient' bridges demanding resources for repair or replacement.

The American Society of Civil Engineers (ASCE) has acknowledged that bridge infrastructure in the U.S. requires significant investment and has given the sector a "C+" grade in their most recent infrastructure report card (2017). They have also estimated that the backlog of repair and replacement of deficient bridge structures come with a US$123 billion price tag (ASCE 2017). One of the major deterioration mechanisms in reinforced concrete highway bridges is reinforcement corrosion. The National Association of Corrosion Engineers (NACE) has performed studies on the cost of corrosion damage across all major sectors of the US economy as well as other major economies around the world (Koch et al. 2002; Koch et al. 2016). According to these reports, the U.S. spends 2.7% of its GDP on corrosion related issues, with infrastructure-related corrosion accounting for 16.4% of this total. Based on the fraction of RC and PSC bridges, this means that approximately $17 billion is spent annually on maintenance of corrosion damage in RC bridge structures. The report also notes that indirect costs associated with corrosion damage (i.e. loss of productivity, traffic delays, etc.) are much harder to quantify and could be 10 times as high as the direct costs (Koch et al. 2002).

Efforts by the engineering community to illuminate the importance of maintaining our bridge infrastructure have led to a bipartisan consensus in Congress that investment in upgrading and improving infrastructure is a chief priority in the coming years (Puzzanghera 2018). As new infrastructure projects are designed and implemented, engineers seek increased service life to improve the economy of projects and to reduce the environmental impact associated with the construction of new infrastructure. This requires developments in innovative construction materials as well as a better understanding of the performance of deteriorated structures.

1.2 Concrete, Corrosion and the Environment

Portland cement, the primary binder material in modern concrete has allowed for the production of infrastructure over the last 100 years on a scale unrivaled in human history. The impressive rate of construction activities comes with a cost, as it has taken a large toll on the environment. For every tonne of portland cement produced, approximately one tonne of carbon dioxide (CO_2) is released into the atmosphere. With the over 300 billion metric tonnes of concrete produced around the globe each year, it has been established that the concrete industry is responsible for approximately 6-7% of man-made CO_2 (Mehta and Monteiro 2014). The aforementioned calls for renewed infrastructure in the U.S. will lead to a new generation of bridges and roadways that bring with them an environmental toll, increasing the need for a greener cement industry. In order to sustainably replace infrastructure, care must be placed in utilizing materials and designs that will result in extended service lives for structures in order to delay the next required replacement that will burden a future generation.

An additional note should be made regarding the changing global climate, which has contributed to unprecedented flooding, hurricanes and coastal storm surge events, etc. and is marked by increased CO_2 levels in the atmosphere and rising sea levels, all of which are going to impact the environmental loading we see on our infrastructure, particularly regarding corrosion. As bridge structures are exposed to more extreme variations in climate and to unanticipated

wetting, drying, freezing and extreme heat, the effort required to maintain these structures will undoubtedly increase. Environmental conditions associated with climate change must be considered and accounted for to effectively design new structures and repair and maintain existing structures.

1.3 Organization of this Dissertation

This dissertation presents research aimed at quantifying the effects of corrosion damage on the structural behavior of reinforced concrete column elements. The research focuses on chloride-induced corrosion and utilizes multiple techniques to accelerate corrosion damage in column specimens. Hybrid Simulation (HS) is utilized to investigate the seismic response of bridge structures with corrosion-damaged columns. An additional focus of the research is understanding how fiber-reinforcement can alter the behavior of these corroded elements.

Chapter Two provides an in-depth background on topics covered in this dissertation, including the principles of corrosion in reinforced concrete, hybrid fiber reinforced concrete (HyFRC) materials, and hybrid simulation (HS) testing methods.

Chapter Three contains experiments regarding the compressive behavior of reinforced concrete and reinforced HyFRC column elements before and after exposure to more than two years of corrosion propagation. The tensile behavior of corroded reinforcing bars is also investigated. Electrochemical properties were tracked over a 125-week corrosion propagation period. One set of columns was designated for compression testing, while another set had rebars excavated for tensile testing. Results show the ductility of HyFRC both before and after corrosion damage has led to cracking of the cover.

Chapter Four describes the development of an experimental setup to perform hybrid simulation (HS) on a single-column bridge structure where the lower portion of the column is replaced with a physical experimental element. This involved updating an Experimental Setup command in the Open Framework for Experimental Setup and Control (OpenFRESCO) to control three degrees of freedom, namely lateral translation, vertical translation and rotation, for a three-dimensional bridge model. This development provides a generalized test procedure for a column element experiencing a lateral loading event. Calibration experiments were conducted on a steel HSS column as an experimental specimen to demonstrate the accuracy of the test method.

Chapter Five describes an experiment where HS is used to assess the seismic performance of corrosion-damaged bridge columns. These columns are similar in cross-section to those described in Chapter Three but are modified for compatibility with the test setup described in Chapter Four. Reinforced HyFRC and reinforced concrete column elements with and without corrosion damage were utilized as experimental specimens. Corrosion damage was accelerated via applied current.

Chapter Six summarizes all results and provides recommendations for future research in corrosion-damaged reinforced concrete, HS and applications of HyFRC.

2 Background

2.1 Corrosion in Reinforced Concrete

Corrosion of reinforcing steel is an electrochemical process that takes place at the interface between embedded steel and the surrounding concrete. Free electrons in the steel can lower their potential energy by participating in an oxidation-reduction (redox) reaction involving iron present in the steel, water in the concrete and, when available, oxygen. This reaction is driven by a potential difference at the interface between the bulk metal and pore solution of the concrete. The overall reaction can be split into two electrochemical processes, an oxidation (anodic) reaction and a reduction (cathodic) reaction. In the oxidation reaction, atomic iron dissociates into an iron ion and two electrons, shown in Eq. 2 - 1.

$$Fe \rightarrow Fe^{++} + 2e \tag{2 - 1}$$
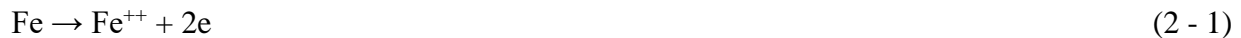
Oxygen at the steel surface may take up these liberated electrons to undergo the reduction reaction shown in Eq. 2-2.

$$\tfrac{1}{2} O_2 + H_2O + 2e^- \rightarrow 2(OH)^- \tag{2 - 2}$$

In the absence of oxygen, hydrogen is reduced in one of two cathodic reactions, shown in Eq. 2 - 3 and 2 - 4:

$$H_2O + 2e^- \rightarrow \tfrac{1}{2} H_2 + (OH)^- \tag{2 - 3}$$

$$2H^+ + 2e^- \rightarrow H_2 \tag{2 - 4}$$
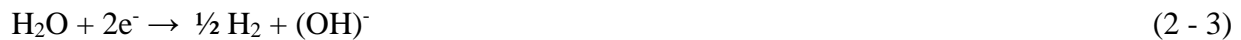
The high internal pH in concrete makes the reaction in Eq. 2 - 3 more favorable than that in Eq. 2 -4. In the presence of oxygen (Eq. 2 - 2), the potential difference that exists at the steel-concrete interface is much greater than if the reduction reaction follows either Eq. 2 - 3 or Eq. 2 - 4. For this reason, corrosion has a much greater effect on reinforcing steel in areas where concrete is exposed to both air and water.

Given a sufficient concrete cover, steel embedded in uncracked, chloride-free concrete is well protected from corrosion due to the high internal pH of 13.0-13.7 that is achieved in the pore fluid of concrete (Mehta and Monteiro 2014). The basic nature of this pore fluid allows for a passive film of iron oxides to form on the steel surface, which reduces corrosion to a negligible rate. This passive film, as described by Nagayama and Cohen (1963), is a highly effective coating, generally only a few nanometers thick, and only stable in an alkaline environment that is free of chlorides.

Concrete's ability to protect reinforcing steel from corrosion is naturally opposed by the environment. Over time, carbon dioxide in the atmosphere penetrates into concrete and reacts with calcium hydroxide. This process, known as carbonation, lowers the internal pH of concrete to a value around 8.5, causing the passive film protecting reinforcing steel to become unstable. Without the protection of a passive film, reinforcing steel becomes susceptible to non-negligible corrosion rates inside the concrete. Given ample time and appropriate moisture conditions, concrete will naturally carbonate, making internal reinforcement sensitive to moisture and oxygen that exists in pore space near the rebar surface (Gonzalez et al. 1980). Though globally relevant in aging structures, the research presented in this dissertation will not focus on corrosion in carbonated concrete and will focus rather on chloride-induced corrosion and accelerated corrosion via applied current.

Chloride ions serve to catalyze the breakdown of the passive film that forms on reinforcing steel and promote the dissolution of iron ions. While regulated and limited in the production of concrete, chlorides are readily encountered during the service life of concrete structures, as they are plentiful in atmospheric moisture and seawater spray in marine environments and are present in deicing salts used to thaw frozen roadways in cold weather regions. Chlorides are particularly harmful as they are not consumed during the corrosion process, thus a relatively small chloride content near the rebar surface can cause a large amount of damage until some remedying action is taken to remove the chlorides either by replacing the cover (Vorster et al. 1992), or electrochemically extracting chloride (Elsener et al. 1993; Fajardo et al. 2006). The American Concrete Institute (ACI) places a limit on the chloride concentration in a given concrete at 0.15% by weight of cement. Above this limit, reinforcing steel is at risk of depassivation and is expected to have a shortened service life due to corrosion. Though research has shown that more important than the chloride content is the Cl^-/OH^- ratio, for which the ACI prescribes a critical value of 0.3 at pH = 13.0 (ACI 222-R1 2001), others have shown that this value is not simply deterministic and depends on multiple factors (Angst et al. 2009).

Once the passive film has been compromised, steel corrosion can proceed more rapidly and iron ions are readily released from the steel surface. The moist concrete cover acts as an electrolyte creating a corrosion cell between the anode region where the oxidation reaction occurs and the cathode region where the reduction reaction occurs. The process is diagrammed in Figure 2 - 1 for the case of chloride-induced corrosion.
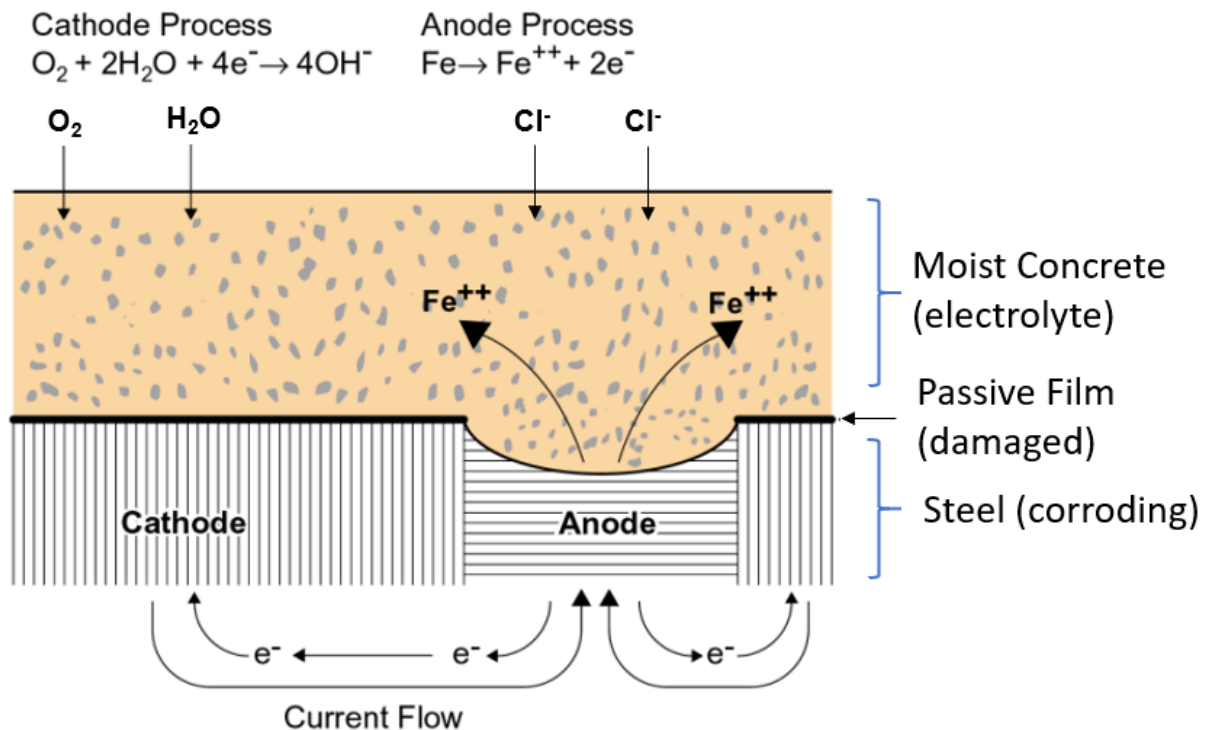
Figure 2 - 1: Diagram of chloride-induced corrosion of reinforcing steel embedded in concrete (After Mehta and Monteiro 2014).

As iron cations are released during the corrosion reaction and subsequently migrate away from the bar surface, they react with anions in the concrete pore solution to form iron oxides that occupy a

larger volume than their original volume in the bulk metal. Due to the tendency of these iron oxides to imbibe water molecules, they can expand to over 600 percent of the volume of the original iron ion (Mehta and Monteiro, 2014). A chart of various species of iron oxides and their associated volume change can be seen in Figure 2 - 2.
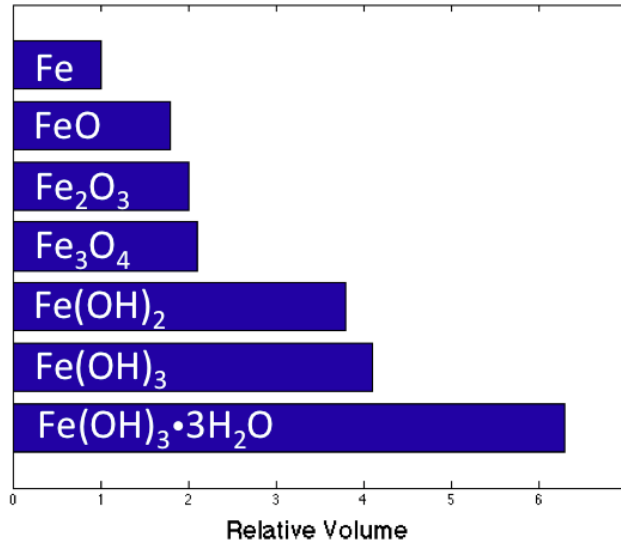
Figure 2 - 2: Various corrosion products and their relative volume compared to atomic iron (After Mehta and Monteiro 2014).

The internal expansion associated with rust formation creates tensile stresses in the concrete, ultimately leading to cracking. As corrosion products push outward, tensile hoop stresses are created in the surrounding concrete. Cracking in the cover then negates the protective nature of concrete, allowing harmful agents to reach reinforcing steel more easily and contribute to the propagation of corrosion, accelerating deterioration. While cracking of the cover depends on the relative sizes of reinforcing bar and cover thickness as well as the porosity of concrete, experiments have shown that only a 0.1 mm thick layer of corrosion products is sufficient to crack the concrete cover, which correlates to as little as 0.02 mm loss of rebar section (Andrade et al. 1993). Additionally, cracks can form in concrete under service conditions before corrosion has initiated. Cracks in the cover have been shown to greatly increase the permeability of concrete to air, water and chloride, which reduces concrete's effectiveness as a protective barrier (Wang et al. 1997; Şahmaran and Yaman 2008; Jaffer and Hansson 2008; Nguyen et al. 2018).

2.1.1 Corrosion Mechanisms

The penetration of chloride ions through the concrete cover can be modeled as a diffusive process and has been modeled by researchers using Fick's Second Law (Costa and Appleton 1999). Additionally, capillary suction has also been found to play a role in the transport of chlorides, and thus regions exposed to wetting and drying are susceptible to a higher rate of permeation of chlorides (Hong and Hooton 1999; Nygaard and Geiker 2005). Because chloride penetration is not uniform, these ions tend to attack reinforcing steel in localized areas. This can leave a small depassivated anodic region surrounded by a large passivated cathodic region, as shown in Figure 2 - 3. This is especially true in the case where pre-cracking leaves a highly permeable pathway to reinforcement (Jaffer and Hansson 2008; Nguyen et al. 2018).
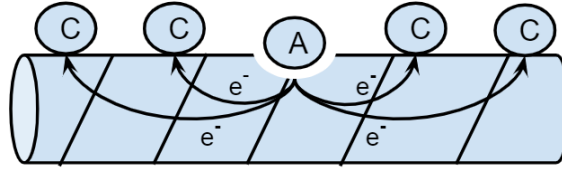
Figure 2 - 3: Diagram of pitting corrosion, where a small anode is surrounded by a large cathode.

This mechanism can develop a localized form of corrosion known as pitting or macrocell corrosion, in which a small area is depassivated, creating a pit. A localized acidic environment inside the pit then forms due to excess iron ions attracting chlorides preferentially over hydroxide ions. This effect, combined with the large cathodic area surrounding the pit creates a galvanic cell. As pitting corrosion is very localized, it can lead to the loss of significant rebar cross section. This can be very detrimental to structures and can result in the loss of strength and ductility of reinforcing steel (Cairns et al. 2005; Du et al. 2005; Apostolopoulos and Papadakis 2008).

Over time, if significant cracking and spalling occur or if a large section of the bar becomes depassivated, microcell or general corrosion can become the dominant mechanism. In this case, the anode and cathode are found near each other, in many repeating cells. This corrosion mechanism produces very uniform products over the length of the reinforcing steel. A simplified diagram of microcell corrosion can be found in Figure 2 - 4. Under this mechanism of corrosion there is no preferential location for anode and cathode.
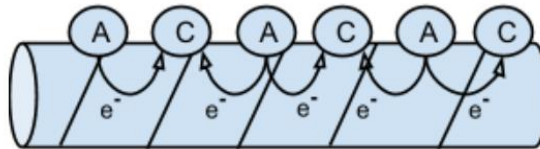
Figure 2 - 4: Diagram of microcell corrosion; repeating adjacent cells of anode and cathode occur along the bar surface, creating a uniform corrosion surface.

Microcell, or general corrosion appears as a uniform surface of corrosion products, which can be more detrimental to cover concrete, as uniform expansive stresses can lead to large splitting cracks or spalling, once corrosion damage has sufficiently progressed (Jen and Ostertag 2016; Nguyen et al. 2018). Once a splitting crack or spalling occurs, the concrete can offer little to no protection to steel, which becomes fully exposed to the environment.

2.1.2 Corrosion Initiation

In order to understand how corrosion affects reinforced concrete structures, it is useful to separate the process into an initiation stage and a propagation stage. First proposed by Tuutti (1982), the two-stage corrosion model defines an initiation period, during which aggressive agents penetrate into the concrete toward passivated reinforcements. This stage culminates in the depassivation of a portion of the reinforcement, thus beginning a propagation stage, during which reinforcements enter an active state of corrosion and lead to damage in the surrounding concrete. Once reinforcing steel is depassivated, it enters an active state of corrosion and the propagation stage begins. Corrosion products form at a higher rate, eventually cracking the concrete and allowing further infiltration of aggressive agents until some serviceability limit is reached and the structure must either be repaired or replaced. Figure 2 - 5 shows the two-stage corrosion model, where the initiation stage can clearly be differentiated from the propagation stage by the sharp increase in corrosion rate.
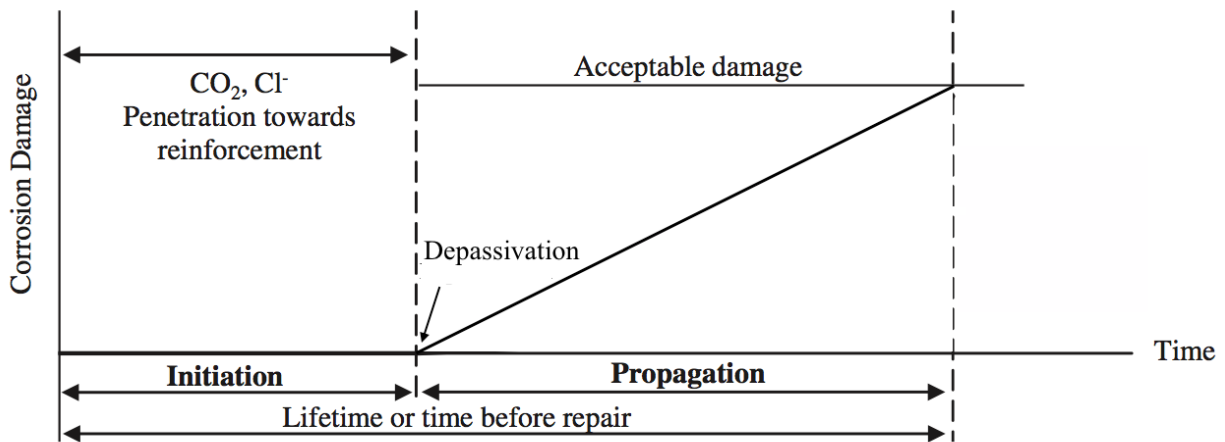
Figure 2 - 5: Plot of corrosion damage vs time for a rebar embedded in concrete (After Tuutti 1982).

In a well-protected environment such as pristine, high-quality concrete with a sufficient cover, the initiation stage can be on the timescale of years, even decades, but in the presence of cracks, the initiation stage can be drastically shortened (Francois and Maso 1988). Cracking is common during the service life of a concrete structure from a variety of sources (e.g. shrinkage, alkali-silica reaction, overloading, small seismic events, etc.). Wang et al. (1997) have shown that cracking can change the permeability of concrete by several orders of magnitude. Experiments have also shown that pre-cracking can greatly shorten the initiation period in reinforced concrete beams (Şahmaran and Yaman 2008; Jaffer and Hansson 2008; Jen and Ostertag 2016; Nguyen et al. 2018). Multi-linear models (as shown in Figure 2 - 6) have also been proposed, to account for significant damage that occurs due to the formation of splitting cracks and spalling and the influence this has on the rate of damage accumulation (*fib* 2006).
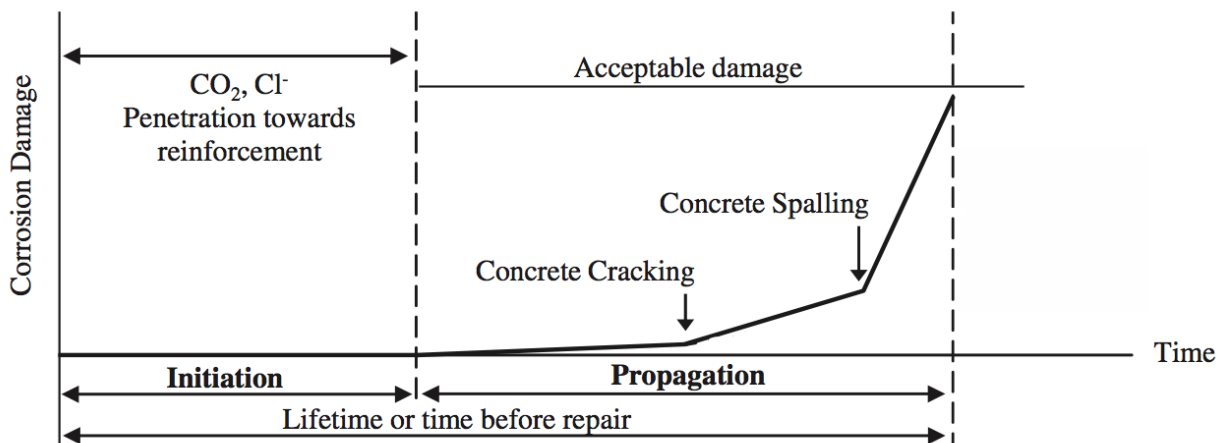
Figure 2 - 6: Modified plot of corrosion damage vs time for a rebar embedded in concrete (After *fib* 2006).

2.1.3 Corrosion Kinetics and the Determination of the Corrosion Rate

The kinetics of oxidation and reduction reactions that occur at the steel surface are a function of the interface potential difference. There is an exponential relationship between the

8

current density and the interface potential, this relationship is described by the Butler-Volmer equation shown in Eq. 2 - 5.

The equation consists of a negative cathodic component and a positive anodic component. A semilog plot of these components (E vs *log(I)*) will yield two linear curves, one describing the

$$I = I_{corr} \times [exp\{\frac{2.303}{\beta_a}(E - E_{corr})\} - exp\{\frac{-2.303}{\beta_c}(E - E_{corr})\}] \qquad (2 - 5)$$

oxidation of iron (anodic reaction) and one describing the reduction of hydrogen or oxygen (cathodic reaction). Where β_a and β_c determine the slopes of the anodic and cathodic curves, respectively, as shown in Figure 2 - 7.
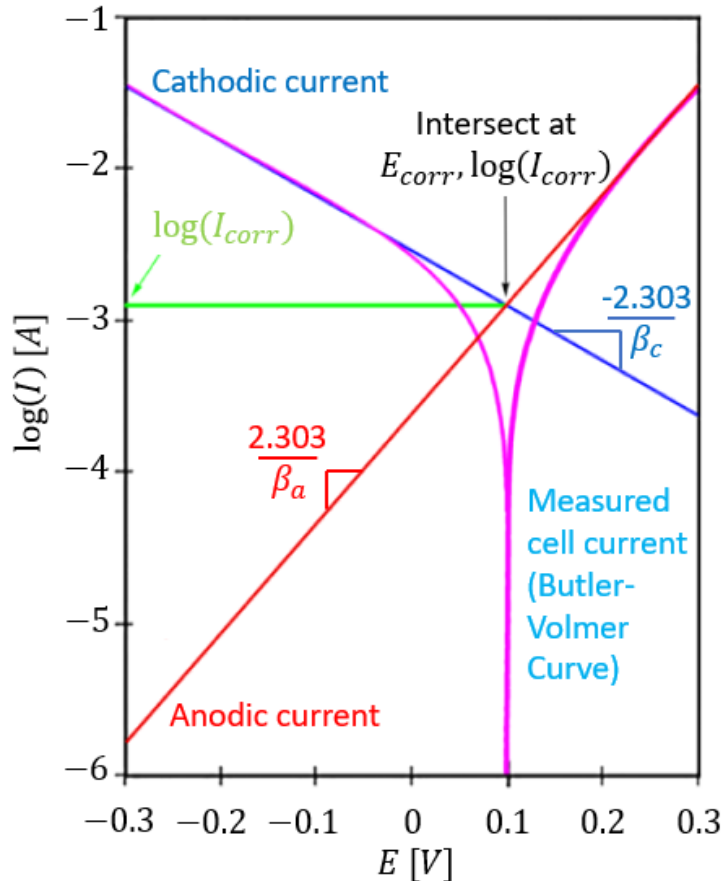
Figure 2 - 7: Components of the Butler-Volmer equation plotted (magenta curve), anodic component (red curve) and cathodic component (blue curve) (Image modified from https://www.gamry.com/application-notes/corrosion-coatings/basics-of-electrochemical-corrosion-measurements/. Sourced on 8/10/19).

The intersection of these curves gives the corrosion potential, E*corr* [V], and the *log* of the corrosion current, I_{corr} [A] (shown in Figure 2 - 7). At values near the corrosion potential, the change in measured cell current versus the change in applied potential gives Eq. 2 - 6.

$$\frac{dI}{dE}|_{E=E_{corr}} := R_P = I_{corr} \times [\frac{2.303}{\beta_a} + \frac{2.303}{\beta_c}] \qquad (2 - 6)$$

9

The slope of the polarization curve at this point is known as the polarization resistance, R_P (shown in Figure 2 - 7), and it follows that Eq. 2 - 6 can be manipulated to achieve the Stern-Geary equation, shown in Eq. 2 - 7.

$$I_{corr} = [\frac{\beta_a \times \beta_c}{2.303 \times (\beta_a + \beta_c)}] \times \frac{1}{R_P} = \frac{B}{R_P} \qquad (2 - 7)$$

Where B is known as the Stern-Geary Constant (Stern and Geary 1957). To determine R_P, a potentiostat with IR compensation is used to polarize the system against a counter electrode to +/- 10 mV of E_{corr} while measuring the net cell current. The regression slope of the data, centered at $I_{net} = 0$, gives the polarization resistance, R_p. To determine the corrosion rate, the B value can either be assumed to have a value of 26 mV/decade (Andrade and Alonso 1996) or the slopes of the anodic and cathodic curves, β_a and β_c, can be determined by through a wider polarization scan (Tafel), which polarize the sample to values further away from the corrosion potential (+/- 75 mV of E_{corr}), where either the anodic or cathodic behavior will dominate the data (Nguyen et al. 2018). Once β_a, β_c, and R_P have been determined the corrosion rate, I_{corr} [mA], can be found using Eq. 2 - 7. This value is commonly normalized by the reinforcement surface area in the region of interest to yield the corrosion current density, i_{corr} [mA/cm^2].

2.1.4 Accelerated Corrosion

Corrosion damage in a well-constructed reinforced concrete structure can take years or even decades to manifest. Accelerated corrosion methods have been utilized for research purposes to control the propagation stage of corrosion (Rodriguez et al. 1997; Lee et al. 2000; El Maaddawy and Soudki 2003; Yuan et al. 2007; Care et al. 2007; Šavija et al. 2013; Meda et al. 2015). By exposing samples to salt water, chlorides can penetrate into the concrete, eventually depassivating the reinforcing steel. However, this can be a slow process, as chlorides must reach the bar via diffusion and exceed the threshold Cl$^-$/OH$^-$ ratio before corrosion can initiate. In order to shorten the initiation period, chlorides can be cast in with the concrete mix (Liu and Weyers 1998). Yuan et al. (2007) has shown that casting chlorides into the mix can affect the geometry of corrosion damage, as corrosion products fully cover the reinforcement, rather than first initiating at the surface closest to the chloride front. Poursaee and Hansson (2009) also noted that this method does not allow reinforcing steel to develop a passive film, which can create experimental artifacts, especially if chemical information about corrosion products is desired.

Due to the nature of the polarization curve and the oxidation and reduction reactions occurring in the corrosion process, if an overpotential is applied, a net cell current is induced that is equal to an increase in the rate of one reaction and a decrease in the rate of the other, as shown in Figure 2 - 8. If an applied current supplies electrons to the anode (i.e. the rebar) this lowers the oxidation rate and thus slows the corrosion process. This is known as cathodic protection and is a well-established method of corrosion protection for civil engineering structures such as bridge decks, and can be applied to prestressed tendons and bridge columns (Glass and Buenfeld 1997; Ishii et al. 1998; Wilson et al. 2013). If polarization of the reinforcing steel takes electrons away from the anode, the oxidation rate increases, thus accelerating the corrosion process. This is the fundamental process behind accelerated corrosion by applied current, by removing electrons from the reinforcing steel, iron ions are oxidized at a higher rate and released into solution. A potentiostat can be used to either apply a potential and measure the resulting cell current, or it can be used as a galvanostat to apply a current and measure the resulting cell potential.
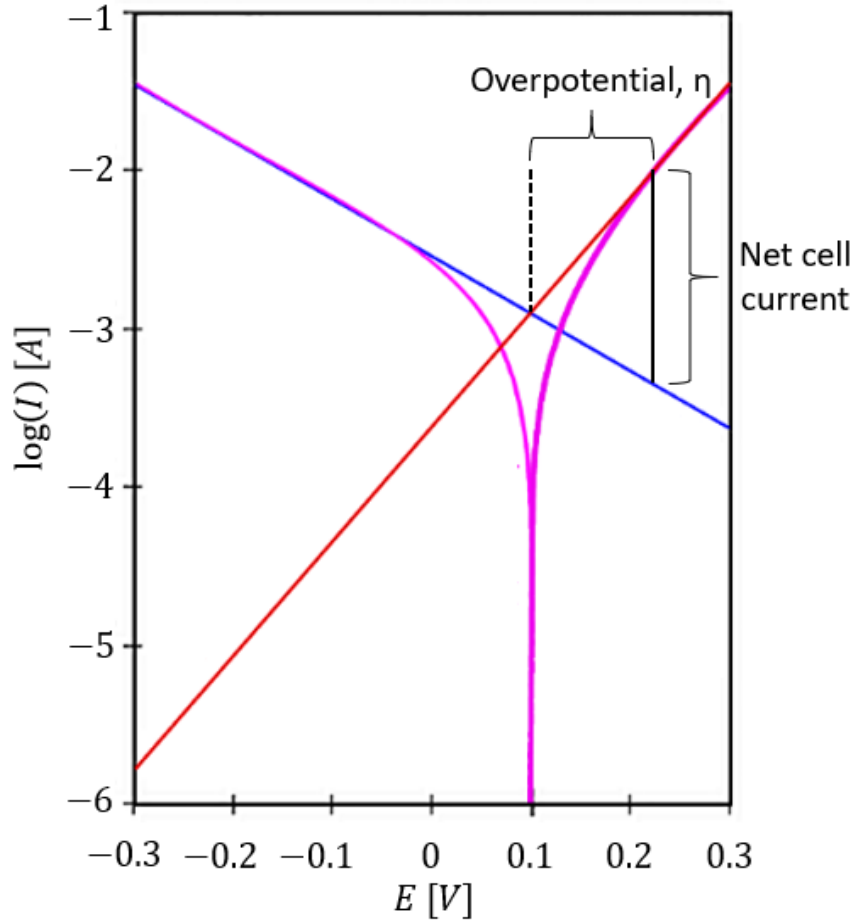
Figure 2 - 8: Polarization curve and principle of accelerated corrosion. (Image modified from https://www.gamry.com/application-notes/corrosion-coatings/basics-of-electrochemical-corrosion-measurements/. Sourced on 8/10/19).

Applied current methods of accelerated corrosion have been used in research as a means of controlling or accelerating propagation damage to study the effects of reinforcement corrosion on the surrounding concrete (Alonso et al. 1998; Lee et al. 2000; Yuan et al. 2007). By applying a current to the reinforced concrete system, corrosion reactions may proceed at a predetermined rate, allowing for greater control over corrosion propagation and the ability to increase the corrosion rate to shorten experimental time scales.

Practical limits to applied current used in accelerated corrosion have been suggested by El Maaddawy and Soudki (2003). By measuring strain in the concrete cover during experiments, the authors were able to find that above a critical current density, there was a stark increase in strain rate developed in the section, shown in Figure 2 - 9. This indicates that the development of corrosion products at the bar surface was being affected by the intensity of applied current. A cell current density lower than 0.2 mA/cm^2 is recommended, as a current density higher than this will result in strains that are not typical of natural corrosion (Andrade et al. 1993).
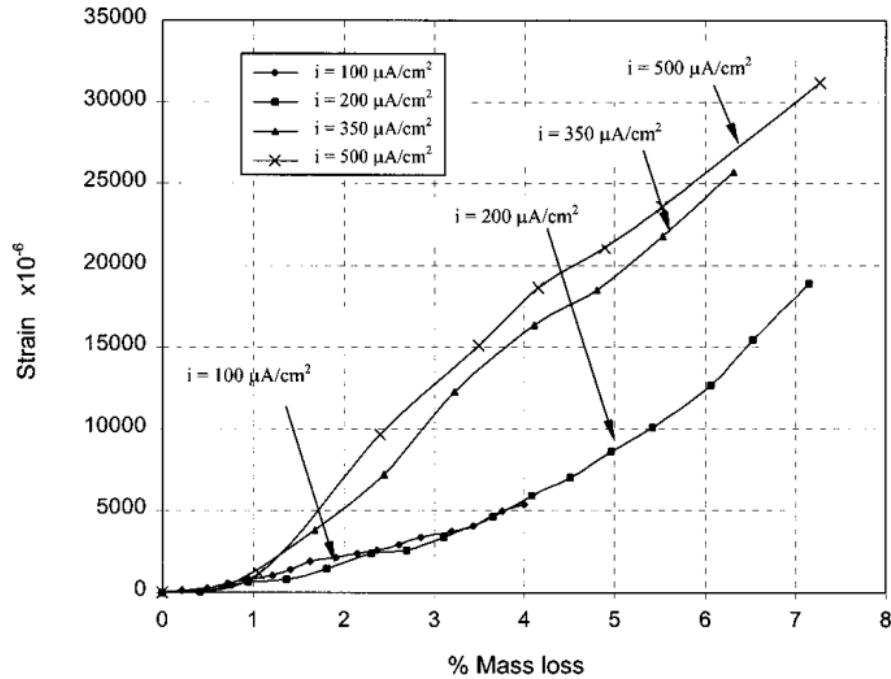
Figure 2 - 9: Strain development vs rebar mass loss for various current densities (El Maaddawy and Soudki 2003).

Caré and Raharinaivo (2007) found that while under high values of impressed current, corrosion products were less likely to migrate into cracks, providing some explanation for the increased strain rate shown in Figure 2 - 9. Yuan et al. (2007) observed differences in color of corrosion products, suggesting that an increased corrosion rate can influence the formation of iron oxide species. Poursaee and Hansson (2009) also found that an impressed current leads to acidification of the pore solution at the rebar surface, based on the hydrolysis of iron ions, shown in Eq. 2 - 8:

$$Fe^{++} + 2H_2O \rightarrow Fe(OH)_2 + 2H^+ \tag{2 - 8}$$
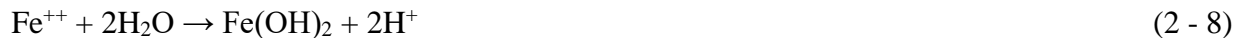
Internal acidic conditions would change the reaction kinetics by introducing new oxidation reactions to the system. A local change in pH would also influence the corrosion products that form. Figure 2 - 10 shows the Pourbaix diagram of iron, which describes the stable species of a metal in an aqueous solution of varying pH and shows that the formation of solid corrosion products is sensitive to the pH of concrete pore solution (Pourbaix 1974).
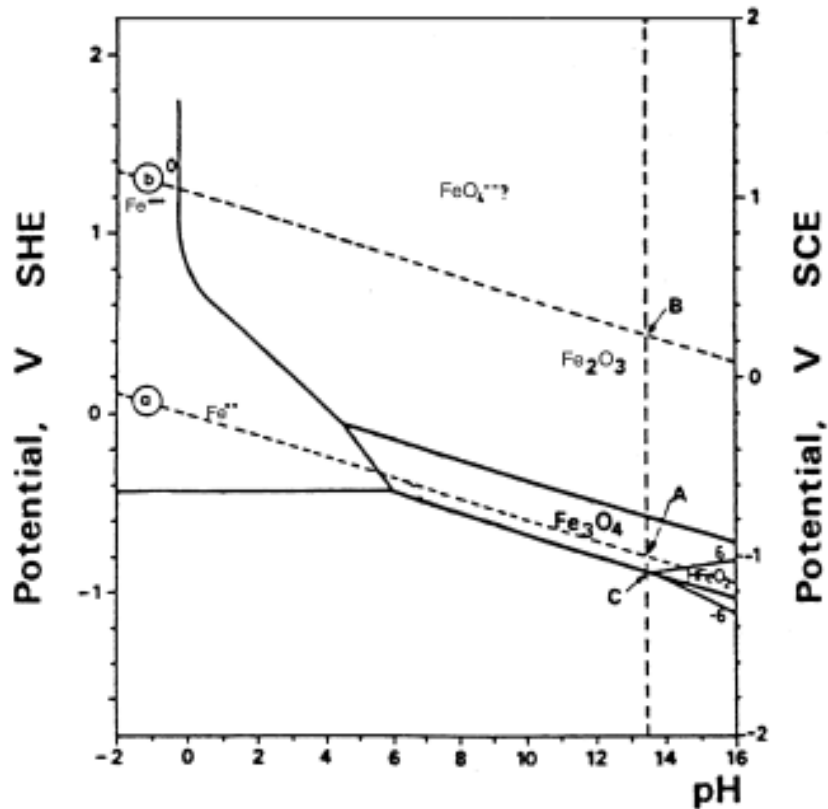
Figure 2 - 10: Pourbaix diagram of iron, vertical dashed line indicating the expected pH in fresh concrete. (After Pourbaix 1974, image sourced from ACI 222-R1 2001).

While the goal of applied current methods is to accelerate the corrosion process, results are less useful if the corrosion products that form and strain conditions are not analogous to those that form under natural conditions. However, if left to natural processes, observing corrosion damage in reinforced concrete elements takes years to produce useful results. While this is a beneficial quality for reinforced concrete as a building material, it creates problems for research into the behavior of deteriorated RC structures and structural elements and can make it difficult to propose methods to improve service life. The research presented in this dissertation thus utilizes accelerated corrosion to impose damage on a structure or element to better understand the influence of deterioration on corrosion damaged column elements within reasonable time-frames expected in an experimental investigation.

2.2 Fiber Reinforced Cementitious Composites

As a structural material, concrete has no expected tensile strength. While it does have some small amount strength in tension, its quasibrittle nature and relatively low strength make it unreliable as a means of tensile resistance in most civil engineering applications. While this deficiency can be offset in structural design through the addition of reinforcing steel, concrete's tendency to crack still creates a vulnerability in terms of durability. By enriching concrete with fiber reinforcement, crack resistance can be improved in the normally brittle cementitious matrix of concrete, resulting in a tougher material capable of tensile strain hardening and/or deflection hardening. Naaman and Reinhardt (2006) proposed a categorization scheme for fiber-reinforced

13

cement-based composites (FRCC) based on their performance in tension and flexure. The mechanical performance of a FRCC depends on its volume fraction (V_f) of fiber-reinforcement. For any given composite, there exists a critical volume fraction $V_{f\,cri}$, above which the FRCC will demonstrate hardening behavior after the onset of composite cracking. If the FRCC achieves hardening behavior in flexure, it is known as a Deflection Hardening FRCC or DFRCC. The corresponding $V_{f\,cri}$ is referred to as $(V_{f\,cri})_{bending}$. Beyond this value is the $(V_{f\,cri})_{tension}$, at which point the FRCC is expected to achieve both deflection hardening and tensile strain hardening. These composites are known as High Performance FRCC or HPFRCC (Naaman and Reinhardt 2006). A diagram of the categorization methodology is shown in Figure 2 - 11.
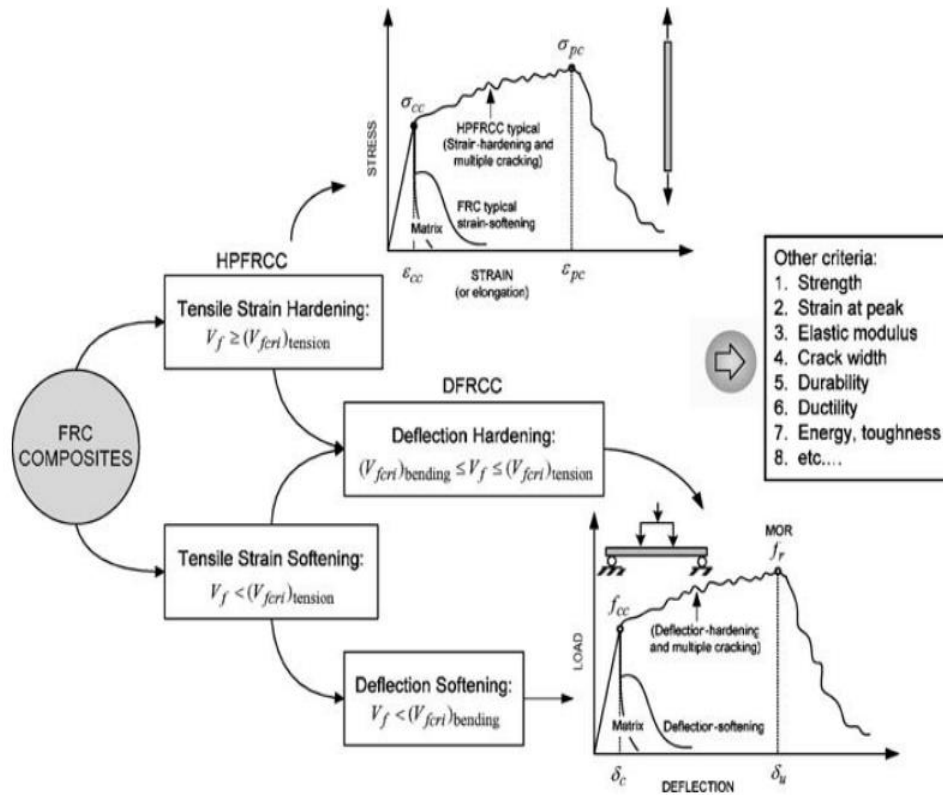
Figure 2 - 11: Categorization of FRC composites based on mechanical performance (Naaman and Reinhardt 2006).

A wide array of FRCCs have been shown to improve ductility over conventional cement-based composites in compression (Ezeldin and Balaguru 1993; Nataraja et al. 1999), and increase both ductility and strength in tension and flexure (Maalej and Li 1994; Blunt and Ostertag 2009). By preventing the propagation of cracks, FRCCs have been demonstrated to improve durability considering permeability (Rapoport et al. 2001; Banthia and Bhargava 2007), alkali-silica reaction (Yi and Ostertag 2005) and corrosion (Berrocal et al. 2015; Jen and Ostertag 2016; Nguyen et al. 2018).

2.2.1 Hybrid Fiber Reinforced Concrete

Hybrid fiber reinforced concrete (HyFRC), as described by Blunt and Ostertag (2009), utilizes two or more scales of short, discontinuous fibers to limit the initiation of cracks at the micro-scale and their subsequent propagation at the macro-scale, which allows for more ductile

deformation beyond peak load under mechanical loading (Blunt and Ostertag 2009; Panagiotou et al. 2015) and has also been shown to improve behavior under environmental degradation such as corrosion (Jen and Ostertag 2016; Nguyen et al. 2018). HyFRC's resistance to crack propagation in durability applications and improved mechanical behavior in seismic applications make it well-suited to address the durability-related problems that plague aging RC structures and is therefore selected for use in this dissertation. Steel-reinforced HyFRC beams have been shown to prevent the formation of a longitudinal splitting crack under both mechanical loading and environmental exposure and were thus also able to control the propagation of corrosion damage compared to conventional RC beams (Jen and Ostertag 2016; Nguyen et al. 2018).

HyFRC promotes ductility through the formation of diffuse microcracking rather the formation of a few dominant cracks (Blunt and Ostertag 2009). This multiple cracking behavior is the result of a toughened matrix that retains tensile strength even after cracking has initiated. The cracking resistance of HyFRC has been shown to improve the corrosion performance in two ways. First, by preventing cracking during service loading, the initiation period is extended, as high permeability pathways to reinforcement are prevented from forming in the matrix, thus stifling the ingress of aggressive agents. Second, after the corrosion propagation phase has begun, the matrix continues to resist crack formation, further preventing exposure of embedded steel to the environment (Jen and Ostertag 2016). The enhancements to corrosion propagation behavior provided by HyFRC are diagrammed in Figure 2 - 12.
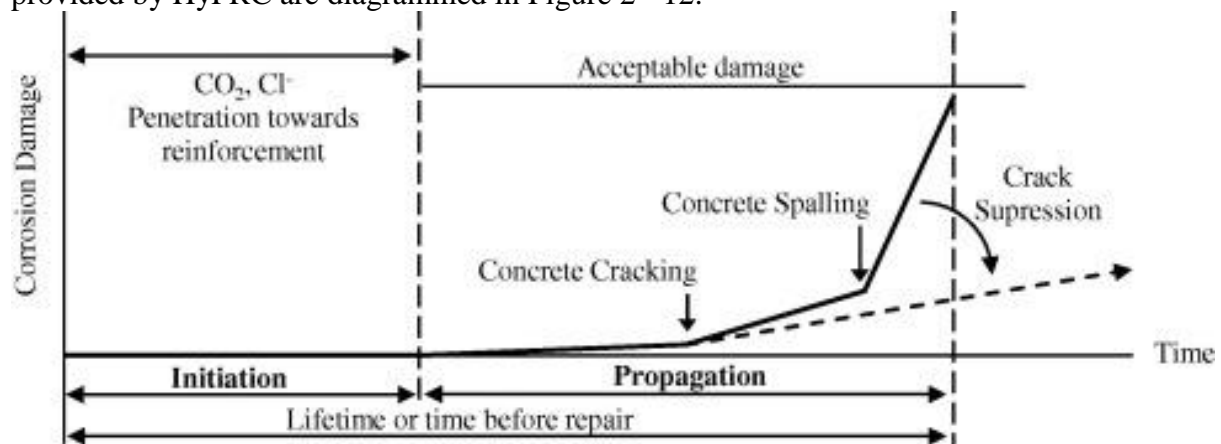
Figure 2 - 12: Corrosion propagation behavior enhancements provided by HyFRC (Jen and Ostertag 2016).

In modern infrastructure design, it is not uncommon to see a designed service life of 200 years (van der Wegen et al. 2012; Markeset and Kioumarsi 2017). Advanced construction materials are required to meet sustainability goals for the construction industry and to advance structural performance for infrastructure subjected to extreme loading. In the research presented, HyFRC is selected for comparison with conventional concrete in steel-reinforced column elements for its demonstrated benefits in durability and mechanical performance. This dissertation advances this research by combining the effects of environmental degradation with extreme loading events under both conventional uniaxial mechanical testing and with Hybrid Simulation (HS).

2.3 Hybrid Simulation

Capturing the nonlinear behavior associated with large deformations and extreme loading in structures is challenging with pure analytical simulation, as highly nonlinear behavior and softening behavior are difficult to predict and model in an accurate and stable manner.

Additionally, models must be verified through system-level experimental testing, usually on a shaking table, which can be both cumbersome and expensive. Large-scale testing becomes increasingly complicated if experimental goals include testing environmentally-damaged specimens, as time scales for this type of damage can be years or even decades. Hybrid simulation (HS) combines physical testing and computer modeling, such that a small portion of a structure can be tested in a physical test setup, while the portions of the structure with predictable behavior can be modeled analytically. By segmenting the overall structure into an analytical substructure and a physical substructure, realistic loading conditions of a system-level test can be applied to a smaller, more manageable physical test specimen, while incorporating the behavior of highly nonlinear components into the response of the overall structure. The overall result is increased accuracy over pure analytical modeling and cheaper and more efficient experimental testing over a system-level experimental test.

To perform HS, a structural model must be segmented to isolate a region of interest that will experience large amounts of inelastic behavior, called the experimental substructure. A physical test specimen representing this portion of the model must be constructed and placed into a test setup so that one or more servo hydraulic actuator can control any experimental degrees of freedom (DOFs) of interest. A compatible finite element software can then be used to apply an extreme loading event such as an earthquake ground motion to the computer model, which interfaces with the experimental test setup through a middleware. A simplified diagram explaining the HS procedure is shown in Figure 2 - 13.
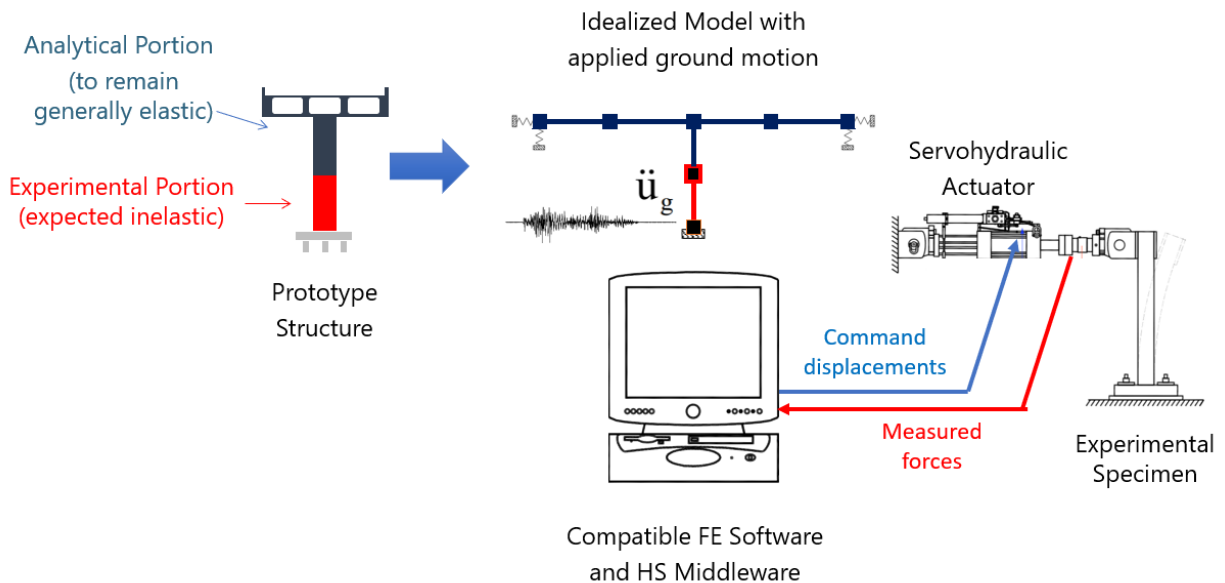
Figure 2 - 13: Schematic diagram of HS procedure.

HS requires the segmentation of a structure into smaller components through a process called substructuring. Individual substructures can then be either modeled numerically in a computer, or physically tested. Physically tested substructures are those that cannot be modeled accurately, while the numerically modeled substructures are those that are expected to remain elastic and/or those with a well-defined geometry, as these substructures can be modeled with greater confidence. Rather than imposing a predetermined displacement history on the physical test specimen(s), the dynamic response of the overall structure is numerically integrated and imposed on the system at each time step of a numerically applied ground motion. Measured forces

from the experimental substructure are communicated into the overall analysis to provide a realistic response of the overall structure.

The principles underlying HS were first developed by Japanese researchers as 'on-line' testing or 'pseudodynamic' testing as an alternative to real-time shaking table tests and were conducted on either simplified models or full structures (Takanashi et al. 1975; Okada et al. 1977; Takanashi et al. 1978). The ideas of utilizing substructuring were introduced later to incorporate the performance of a full structure while only requiring a smaller, more manageable physical substructure (Mahin and Shing 1985; Dermitzakis and Mahin 1985) and also to promote the feasibility of geographically distributed testing (Stojadinovic et al. 2006). HS can be conducted pseudodynamically, in which dynamic effects are taken into account numerically, with testing performed at a slower rate (Dermitzakis and Mahin 1985), or in real-time, in which case the computed displacements are applied with a rate equal to computed velocities (Mercan and Ricles 2007; Shao et al. 2011; Mosalam and Günay 2013) The research presented in this dissertation focuses on pseudodynamic HS.

2.3.1 Substructuring and Equations of Motion

Hybrid Simulation relies on the principle of substructuring, in which the stiffness matrix of a structure is reorganized such that the stiffness of one component is decoupled from the remainder of the structure so force-displacement relations can be used independently (Dermitzakis and Mahin 1985). Given an applied ground motion a_g, the equations of motion for the discretized structural system (shown in matrix form in Eq. 2 - 9) are then numerically integrated to solve for the displacements, velocities and accelerations at each time step (Chopra 2013).

$$\mathbf{m}\underline{a} + \mathbf{c}\underline{v} + \mathbf{k}\underline{d} = -\mathbf{m}\underline{a}_g \tag{2 - 9}$$

Where $\mathbf{m}$, $\mathbf{c}$, and $\mathbf{d}$, are the nxn mass, damping and stiffness matrices of the system, respectively, and $\underline{a}$, $\underline{v}$ and $\underline{d}$ are the nx1 vectors describing the acceleration, velocity and displacement of the degrees of freedom of the system. On the right-hand side of the equation, $\underline{a}_g$ is the ground acceleration imposed on the structure. Due to substructuring, the stiffness matrix can be decomposed such that when multiplied by the displacement vector will result in two decoupled vectors, one for restoring forces of the computational substructure and one for the restoring forces of the experimental substructure, as shown in Eq. 2 - 10.

$$\mathbf{m}\underline{a} + \mathbf{c}\underline{v} + \underline{r} + \underline{r}^* = -\mathbf{m}\underline{a}_g \tag{2 - 10}$$

Where $\underline{r}$ and $\underline{r}^*$ are the restoring forces of the computational substructure and experimental substructure, respectively (Dermitzakis and Mahin 1985).

2.3.2 Numerical Integration Techniques

Various algorithms have been tested and used to numerically integrate this system of equations, including the central difference method (Okada et al. 1977; Takanashi et al. 1978), Explicit Newmark method (Mahin and Shing 1985; Dermitzakis and Mahin 1985; Mosalam and Günay 2013), and Generalized- α method (Chung and Hulbert 2019; Bonelli and Bursi 2004). These methods do not require iterations, making them adequate for HS. A robust and HS compatible finite element analysis program must be used to perform hybrid simulation. Given its vast library of material models, elements of specific interest in structural engineering, and HS compatible integration methods, the Open System for Earthquake Engineering Simulation, OpenSEES, was used for all HS experiments presented in this research (McKenna et al. 2002). In addition to the analysis software, an additional communication software must be used to

communicate displacements to and receive force feedback from the experimental setup. The Open Framework for Experimental Setup and Control, or OpenFRESCO, was selected for the communication software to interface between OpenSEES and the experimental test setup (Schellenberg et al. 2009).

2.3.3 Error Identification and Reduction

Error identification and quantification is done in both computational and experimental research. Because hybrid simulation utilizes both computational and experimental components, it is subject to errors from both of these sources as well as additional errors due to interaction between substructures, and since each time step depends on data from the previous step, these errors can propagate and build if not addressed (Mosalam and Günay 2013; Chae et al. 2018).

Broadly, there are two types of errors that can affect the accuracy of HS: The first type is random error which include roundoff and random noise in measurement devices. This type of error generally cannot be controlled. The second type is systematic error(s), which are those that depend on computational methods (e.g. integration method, time step size, etc.) and experimental methods (e.g. PID controller, actuators, test frame, DAQ, etc.) and are thus specific to a given experiment (Thewalt and Mahin 1987). Measures should be taken to minimize these types of errors to maximize accuracy. Displacement errors are quantified by comparing commanded displacements with measured displacements imposed on the test specimen, while force errors have to do with time delays in restoring force measurement. Root mean square (RMS) can be used for cumulative error analysis (Dermitzakis and Mahin 1985), though this method neglects the signs of error. Mercan and Ricles (2008) introduced a tracking indicator to sum the cumulative error in the analysis while accounting for sign changes during error propagation. Reduction of errors in the system should include measures such as: (a) using high quality mechanical equipment, including controllers, servovalves, actuators and stiff reaction frames; (b) minimizing backlash and friction in the experimental setup; and (c) addressing feedback errors that excite higher modes through numerical damping (Mahin and Shing 1985).

2.3.4 Hybrid Simulation of RC Bridge Columns

Terzic et al. (2014) performed HS on a multi-span bridge with single-column bents. The lower half of one column was taken to be the experimental element to determine the post-earthquake truck-load capacity of the structure. Vertical load was applied via a spreader beam with two jacks while lateral displacement and rotation of the top node was applied with four actuators connected to a rigid link (two actuators controlling lateral displacement and rotation in the longitudinal direction of the bridge and two in the transverse direction). They used hybrid simulation to successfully apply gravity loading, earthquake motions and truck loading to verify the post-earthquake truck-carrying capacity of RC bridges. Chae et al. (2018) used real-time hybrid simulation (RTHS) to apply horizontal and vertical ground motions to a bridge column. They found that resonance with the oil column and the axially stiff bridge column led to the unstable growth of errors during testing. They were able to improve their results by resorting to force control in the axial component while remaining in displacement control for the lateral component.

Hybrid simulation (HS) presents a unique solution to better understand the combined hazard of seismicity and corrosion damage in bridge columns. Corrosion damage has been shown to deteriorate the bond between steel and concrete and reduce the flexural capacity of reinforced concrete elements (Fang et al. 2004; Jen and Ostertag 2016; Nguyen et al. 2018). While researchers have attempted to model this process (Bažant 1979; Molina, Alonso, and Andrade 1993; Tapan and Aboutaha 2011) and others have performed large-scale structural testing on corrosion-

damaged components (Okada et al. 1988; Pantazopoulou et al. 2001; Meda et al. 2015), system-level seismic behavior of corrosion-damaged structures has not been investigated. The research presented will utilize HS to develop a method for testing corrosion damaged components and quantify their implications on system-level performance.

3 Uniaxial Behavior of Corrosion-Damaged Reinforced HyFRC Columns

3.1 Introduction

The actual capacity of corrosion-damaged bridges is of great importance for understanding existing infrastructure and for decision-making about repair and replacement. The behavior of HyFRC materials in this type of application is not well understood. Additionally, while the corrosion initiation behavior of HyFRC materials has been investigated elsewhere (Jen and Ostertag 2016; Nguyen et al. 2018), the corrosion propagation behavior of HyFRC has not been well observed due to the long corrosion initiation time associated with the composite. This chapter contains axial performance of corrosion-damaged columns in a long-term corrosion propagation experiment. Columns were constructed of steel-reinforced self-consolidating concrete (SCC) and self-consolidating HyFRC (SC-HyFRC) and were cast with a chloride concentration of 2% by weight of binder to bypass the corrosion initiation period. To drive corrosion reactions, specimens were cyclically exposed to wet and dry environments simulating field conditions over a 125-week period. Surface crack formation and growth was monitored, and electrochemical measurements were conducted to determine the corrosion rate. Axial stiffness was measured at the beginning, middle and end of the corrosion exposure period. Following corrosion exposure, one subset of column elements was tested to failure under uniaxial compression and compared with pristine column elements that were tested to failure before the onset of corrosion damage. The reinforcing steel from a second subset of columns was excavated and tested under uniaxial tension. Behavior of corroded rebar was compared with that of pristine reinforcing steel.

3.2 Materials and Specimens

3.2.1 Self-Consolidating Hybrid Fiber Reinforced Concrete (SC-HyFRC)

A self-consolidating variant of HyFRC (SC-HyFRC) is compared with a non-fiber reinforced self-consolidating concrete (SCC) in steel-reinforced column elements to investigate corrosion propagation of rebar in a crack resistant matrix and the impacts on uniaxial performance. Mix designs used in this experiment, shown in Table 3 - 1, are based on those described by Jen et al. (2016). The SC-HyFRC mix employed two tiers of fibers, namely 8-mm long polyvinyl alcohol (PVA) fibers with a length-to-diameter aspect ratio of 200 and 30-mm long hooked-end steel fibers with a length-to-diameter aspect ratio of 55. A total fiber volume fraction of 1.5% of concrete volume and the material has been shown to demonstrate strain hardening and deflection hardening characteristics (Jen et al. 2016).

Table 3 - 1: Mix proportions for SC-HyFRC and SCC [per 1 m^3].

	SC-HyFRC	SCC
Cement (Type II/V) [kg]	397	397
Fly ash (Class F) [kg]	131	131
Coarse aggregate [kg]	418	497
Fine aggregate [kg]	1044	1006
Batched water [kg]	237	237
PVA fibers [vol. %]	0.2	-
30mm Steel fiber [vol. %]	1.3	-
Water to binder ratio	0.45	0.45
Superplasticizer[c] [wt. % of binder]	0.93	0.42
Viscosity modifier [wt.% of binder]	2.21	0.40
Cl$^-$ [wt.% of binder]	2.0	2.0
f'_c [MPa]	38[a]/33[b]	54

[a] – SC-HyFRC used for high transverse reinforcement ratio columns (H1)
[b] – SC-HyFRC used for low transverse reinforcement ratio columns (H2)
[c] – Polycarboxylate Superplasticizer used in all mixes

The SCC control mix was designed with similar matrix proportions and the same water-binder ratio (0.45) as SC-HyFRC but resulted in a higher compressive strength. Additionally, casting of the SC-HyFRC material was done in two separate batches, resulting in some variation in compressive strength between the two mixes. Sodium chloride (NaCl) was added to the mixing water such that the chloride content was two percent of the weight of binder in order to achieve rapid depassivation of longitudinal reinforcement. Similar values of sodium chloride addition have been used in other propagation tests (Gonzalez et al. 1980; Y. Liu and R. E. Weyers 1998). It has been noted that the addition of sodium chloride can influence the strength development of concrete (Lui and Weyers, 1998), which, combined with interactions with chemical admixtures may have led to the varied strength development in the various mixes (Shanahan, 2016). The large difference in compressive strength in the SCC vs SC-HyFRC may also indicate different matrix conditions at the rebar-matrix interface, which will impact corrosion behavior.

3.2.2 Column Design

Prismatic column specimens with a square cross section and dimensions of 178x178x483 mm dimensions were utilized to simulate a scaled bridge column that would serve in a marine environment. One set of reinforced SCC columns were created as a control for the experiment, referred to herein as C, while two sets of reinforced SC-HyFRC columns were cast. The first,

referred to herein as H1, contained identical reinforcement details to the C specimens, while the second set, referred to as H2, contained a reduced transverse reinforcement ratio (reduced by a factor of 3). The set of low-transverse reinforcement ratio columns serve to demonstrate the ability of HyFRC materials to confine the column core, reducing the required transverse reinforcement to provide lateral stability to longitudinal reinforcement (Panagiotou et al. 2014). A drawing of a typical column can be found in Figure 3 - 1, and reinforcement properties can be found in Table 3 - 2. All specimens used ASTM type A706 grade 60 steel for longitudinal reinforcement and had mill scale removed via abrasion to promote corrosion initiation (ASTM 2016).
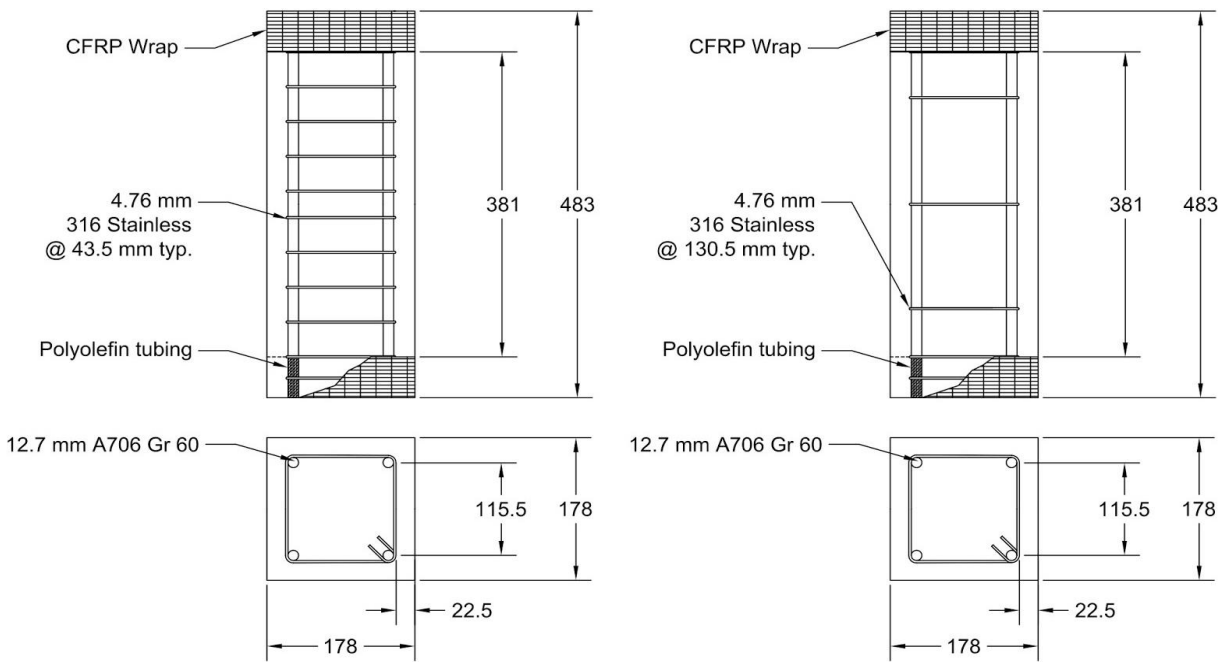
Figure 3 - 1: Details of column specimens [mm]. C and H1 (left), H2 (right).

Table 3 - 2: Reinforcement ratios of column specimens.

	C	H1	H2
Longitudinal reinforcing ratio	1.6%	1.6%	1.6%
Transverse reinforcing ratio	1.2%	1.2%	0.4%

Transverse reinforcement was provided by hoops made from spring-tempered type 316 stainless steel for improved corrosion resistance in a chloride-rich environment (when compared to 304 stainless steel or A706 reinforcing steel). Stainless steel was selected to limit corrosion damage to transverse reinforcement. Each hoop was isolated from the longitudinal reinforcement at 90° corners via electrical tape to prevent bars from becoming galvanically connected to one another. Hoops were in contact with longitudinal bars at the 135° hook to allow for increased cathodic area to further drive corrosion reactions. A 50mm section at both ends of each longitudinal bar was treated with a coating of polytetrafluoroethylene (teflon) tape, electrical tape and polyolefin heat shrink tubing to isolate a region of interest in the central 380 mm of the specimen. Externally, this 50mm end section was treated with a carbon fiber reinforced polymer (CFRP) wrap to provide

additional confinement at the ends during compressive loading to concentrate damage within the region of interest. All column specimens were cast horizontally and subsequently tilted upright after demolding.

3.3 Methods

3.3.1 Damage Monitoring

Surface cracks were visually inspected and measured with a crack comparator. The growth of cracks in concrete increases the permeability of the cover to air, moisture and further infiltration of chlorides (Jaffer et al. 2009). Fiber reinforcement has been shown to limit crack growth in concrete and improve corrosion propagation behavior (Jen and Ostertag 2016; Nguyen et al. 2018). It is of interest to understand how crack growth due to reinforcement corrosion impacts the corrosion rate during the propagation stage. In this experiment, crack patterns were observed and maximum crack openings were measured for all specimens to compare the cracking behavior of SCC and SC-HyFRC and to further relate this to corrosion rates in column specimens. It is of interest to observe the formation of splitting cracks due to the growth of corrosion products.

3.3.2 Environmental Conditioning and Electrochemical Measurements

Column elements were cyclically exposed to wet and dry cycles to simulate service conditions. During wet cycles, columns were placed in a 100% RH fog room and were subsequently placed in ambient laboratory conditions (23ºC, 50% RH) to simulate 'dry' conditions. This cycle involved two weeks wet followed by two or more weeks dry. Immediately following a two-week wet cycle, the corrosion potential of each reinforcing bar was measured and, in alternating cycles, polarization resistance measurements and tafel scans were taken to determine the corrosion rate of each longitudinal reinforcing bar in a given column. In instances where only corrosion potential was measured, specimens were removed from the fog room and wrapped in wet burlap while a saturated calomel reference electrode (SCE) was placed on a moist sponge at the concrete surface. All corrosion measurements were taken with either a Gamry G750 or Gamry Interface 1000 potentiostat, both of which act as a zero-resistance ammeter (ZRA). Each individual bar was separately taken as the working electrode to measure corrosion potential. In instances where the corrosion rate was determined, columns were placed in a PVC dam such that the length of the column could be submerged in 3.5% NaCl solution while the ends of the column remained dry. After a 12 to 24-hour period to allow conditions to reach a steady state, corrosion potential, polarization resistance and Tafel curves were measured to determine the corrosion rate for each bar, as described in Section 2.1.3. During these measurements the SCE was immersed in the NaCl solution along with a stainless steel mesh that was used as the counter electrode. Schematic drawings of the corrosion measurement setups are shown in Figure 3 - 2.
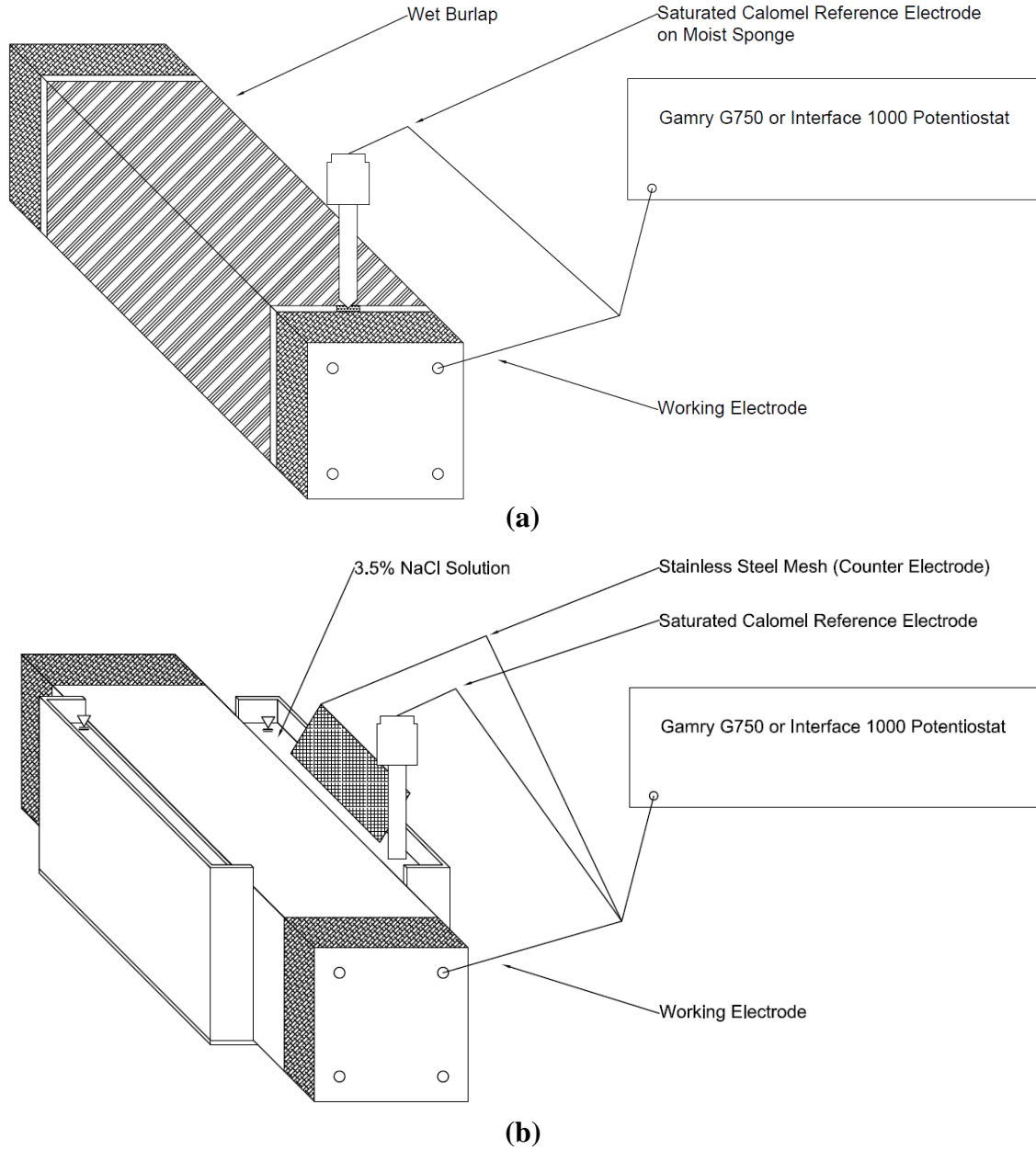
Figure 3 - 2: Electrochemical measurement setups: corrosion potential only (a) and corrosion rate (b).

Once a corrosion rate has been determined, this information can be used to determine the theoretical mass loss of a given rebar (Andrade et al. 1993). By integrating the corrosion rate over time, one can determine the charge transfer, Q, which can then be used with Faraday's First Law of Electrolysis, shown in Eq. 3 - 1, to determine the total mass lost.

$$\Delta m = \frac{Q \cdot M}{z \cdot F}$$

(3 - 1)

Where Q is the total charge transferred [C], M is the molar mass [g/mol], z is the valency and F is Faraday's constant [C/mol] (Andrade et al. 1993).

3.3.3 Mechanical Testing

Stiffness measurements were performed using a 1.8 MN universal testing machine (UTM) by loading the columns elastically to a predetermined load approximately 30% of the ultimate strength in five consecutive cycles. This was performed at four weeks, 24 weeks, and at approximately 140 weeks to track any changes in elastic stiffness. Sacrificial specimens were also cast and tested to failure for each sample set at 28 days in order to validate the elastic range, as well as for comparison purposes for future testing. Displacements at the 28-day mark were measured using displacement transducers epoxied to the concrete surface. Subsequently, at the 24-week measurement, linear variable differential transformers (LVDT) were added via a bracket system in order to achieve an improved signal. Images of the bracket system used during mechanical testing can be seen in Figure 3 - 3. All LVDTs were removed from the bracket prior to the final loading to failure at the conclusion of the experiment. For the final loading for specimens C-a and H1-a, the strength of the columns had exceeded the capacity of the testing machine, so these columns were tested using a 17.8 MN universal testing machine.
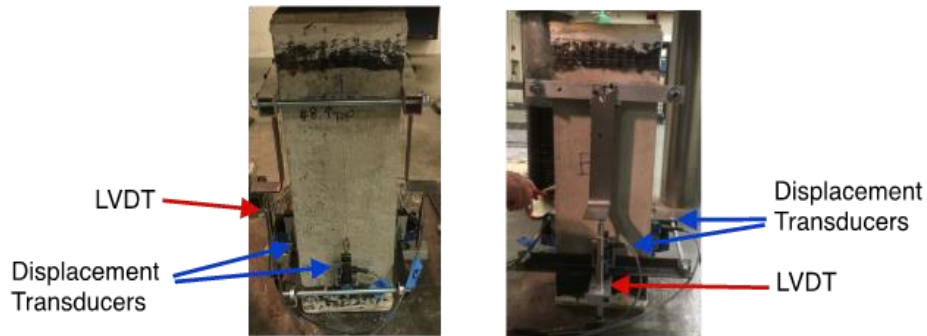
Figure 3 - 3: Typical stiffness test setup for a column.

3.3.4 Rebar Excavation, Cleaning, and Tensile Testing

Following the corrosion exposure period and final mechanical testing, rebars were excavated by mechanically removing the concrete cover with a hammer-drill. After the transverse reinforcement was cut away, the longitudinal reinforcement could be separated from the concrete core. The rebar was subsequently cleaned with a solution of HCl and hexamethylene tetramine according to ASTM G1-03 (ASTM 2017). The mass of each bar was recorded to determine the gravimetric mass loss over the duration of the experiment.

Reinforcing steel from columns that did not undergo full compression testing was then tested in tension on a 534 kN UTM. Testing was performed using displacement control with a strain rate of 0.0017 per min (set by using an initial load rate set at 44.5 kN/min during the elastic regime). Pristine bars were also tested in this setup as a control. Data collection was done via a digital extensometer. An image of the tensile testing setup can be seen in Figure 3 - 4.

Figure 3 - 4: Tensile testing of reinforcing steel. The digital extensometer (Green) is attached to the rebar via clips. Rebar is loaded into UTM. (Image courtesy of Ian Williams).

3.4 Results and Discussion

3.4.1 Damage Monitoring

Surface cracking was first inspected at 28 days, at which point no cracking was observed in any specimens. First cracking was observed in C column specimens at 12 weeks. Detail images in Figure 3 - 5 of a sample crack progression in a C column specimen show crack growth and how crack widths were determined using a crack comparator. A summary of maximum measured crack width and number of full-length splitting cracks at various times during the corrosion exposure period are shown in Table 3 - 3.

| 12 Weeks | 26 Weeks | 56 Weeks | 82 Weeks |
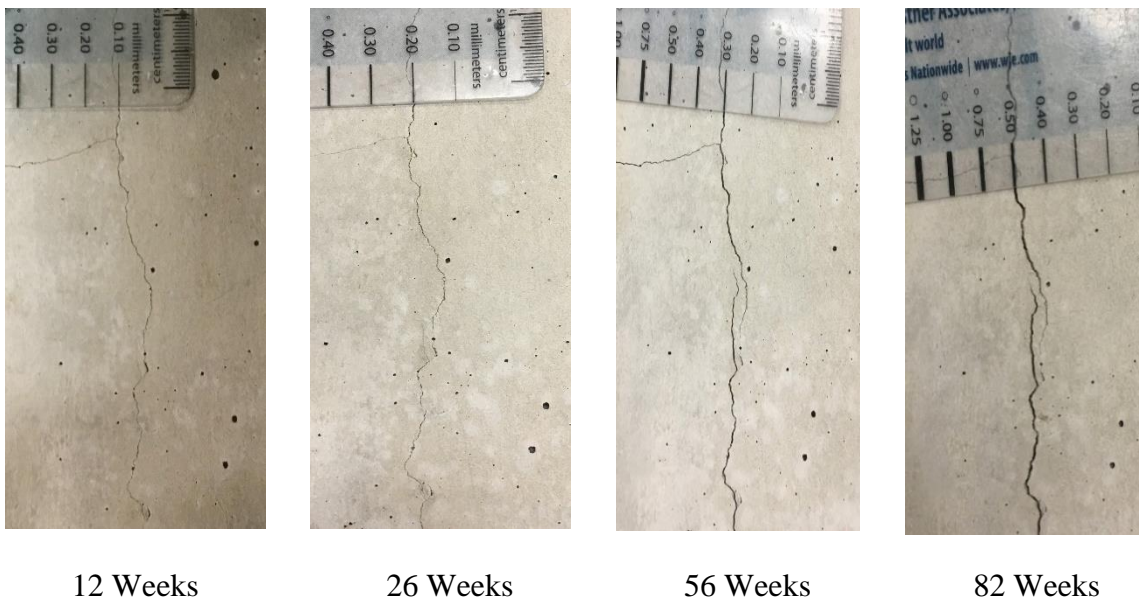
Figure 3 - 5: Crack growth in C column specimen.

Table 3 - 3: Cracking observations in column specimens.

	C	H1	H2
Time to first observed cracking [weeks]	12	56	56
Max. crack width at 12 weeks [mm]	0.1	--	--
Max. crack width at 26 weeks [mm]	0.2	--	--
Max. crack width at 56 weeks [mm]	0.4	0.1	0.1
Max. crack width at 82 weeks [mm]	0.75	0.2	0.2
Max. crack width at 123 weeks [mm]	0.8	0.3	0.4

Since specimens were cast horizontally, cracking patterns were dependent on orientation and are referred to according to the diagram shown in Figure 3 - 6. The first cracking observed in C specimens manifested as full-length splitting cracks along the longitudinal reinforcement oriented closest to the casting surface on the sides adjacent to the top surface during casting (along the 'top' bars on sides B and D in Figure 3 - 6). First cracking in both H1 and H2 specimens occurred later, at 56 weeks and manifested as short, discontinuous cracks. These cracks eventually extended and, in some cases, connected to form partial-length splitting cracks by 82 weeks. Corrosion of fibers at the surface was observed in both H1 and H2 specimens. A flatbed scanner was used to collect high resolution images of each surface of column specimens following the corrosion exposure period. Images of representative cracking patterns in different specimen types are shown in Figure 3 - 7.
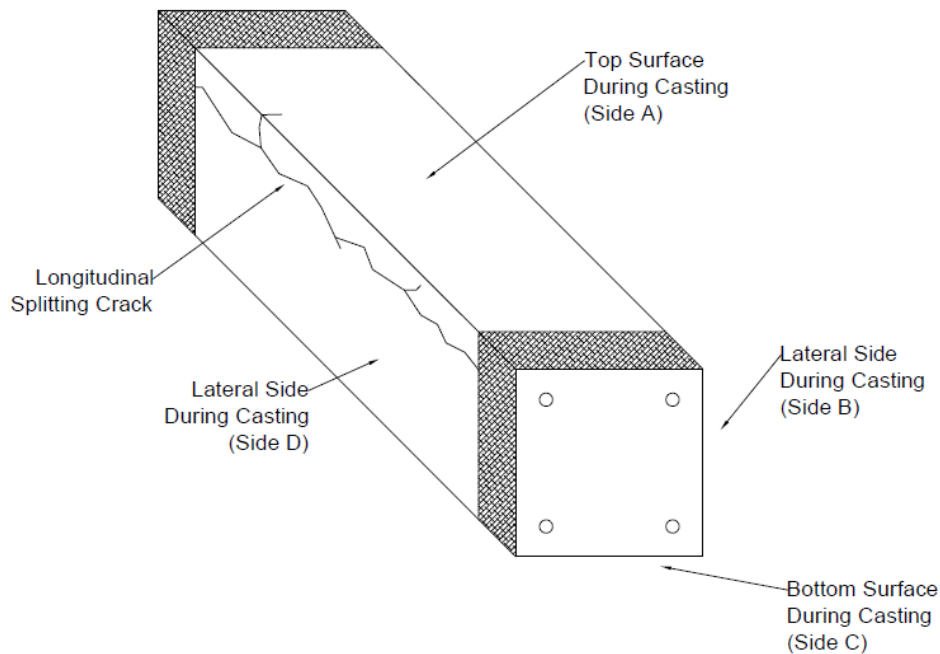
Figure 3 - 6: Diagram showing casting orientation of column specimens.

| C | H1 | H2 |
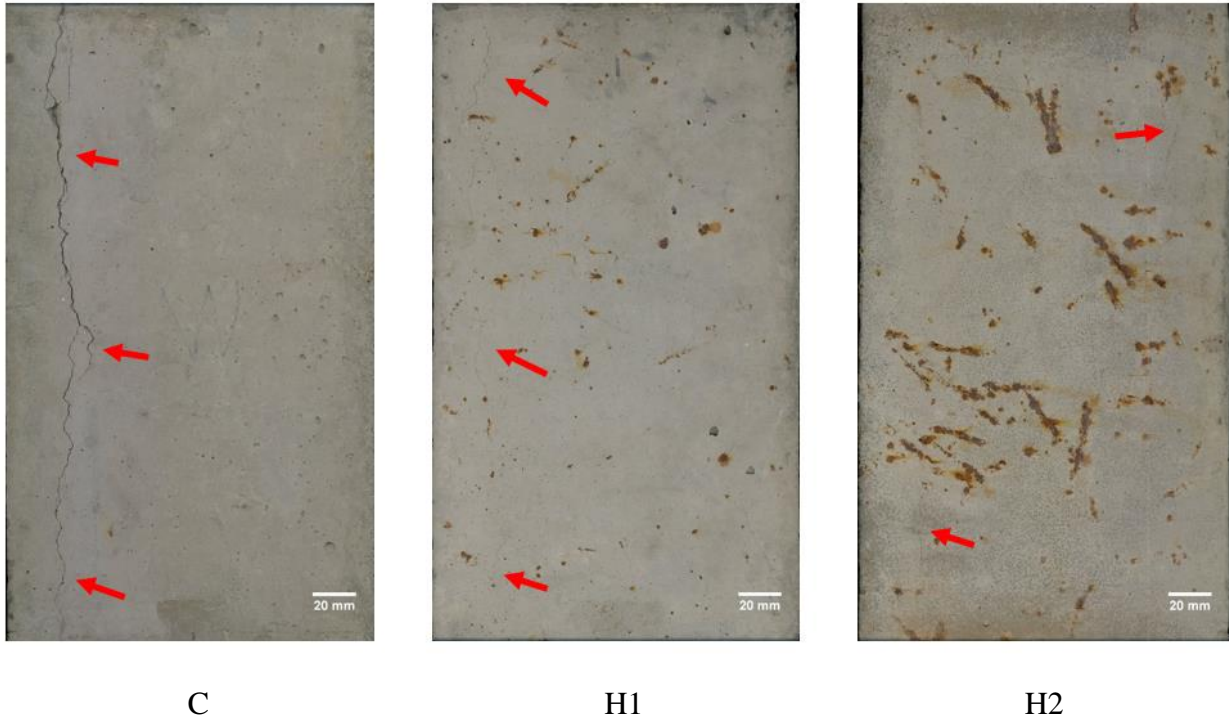
Figure 3 - 7: Images of typical crack morphology on lateral (B or D) sides of column specimens. Red arrows indicate full or partial length splitting cracks.

Splitting cracks in C specimens had the greatest width and extended the full length of the column, though cracking was limited to bars closest to the casting surface. The bars closest to side 'A' in Figure 3 - 6 will herein be referred to as 'top' bars, while rebars closer to side 'C' will be referred to as 'bottom' bars. In H1 and H2 specimens, short discontinuous cracking was first found along 'top' bars, though was later also found along 'bottom' bars. Cracks eventually lengthened and connected to form partial length splitting cracks.

During corrosion propagation, cracking and damage to the cover is expected in all specimens due to the introduction of a high concentration of Cl⁻ during casting. Fiber-reinforced concrete has been shown to limit crack growth during corrosion propagation (Nguyen et al. 2018). In this study, because chlorides were cast into the concrete, the entire length of reinforcing steel is expected to be subjected to a corrosive environment, though the local threshold for corrosion may be different depending on local porosity, resistivity, pH, defects, etc. (Angst et al. 2009).

As the SCC mix was highly flowable, it is possible that segregation may have occurred in C specimens during casting, leading to a higher proportion of mortar with less coarse aggregate along the reinforcing steel near the top surface (Side A). This would create a propensity toward shrinkage cracking at the 'top' bars that would encourage corrosion activity. Fiber-reinforcement has been shown to prevent shrinkage cracking, and so this would not be as much of a problem in H1 and H2. HyFRC limited the growth of splitting cracks during corrosion propagation, though cracking was observed at the surface in both H1 and H2 specimens. Additionally, since the compressive strength of the H1 and H2 specimens was much lower, this indicates a more porous rebar-matrix interface, which would accommodate more corrosion products growth before developing large tensile strains in the surrounding matrix.

28

Plots for all electrochemical measurements show bars from each column averaged according to their position relative to the top surface during casting, as shown in the diagram in Figure 3 - 6, with 'top' bars shown with a dashed line, and 'bottom' bars with a solid line. Following each 2-week wet cycle during the corrosion exposure period, the corrosion potentials (vs SCE) of each longitudinal reinforcing bar within each column specimen are shown in Figure 3 - 8.
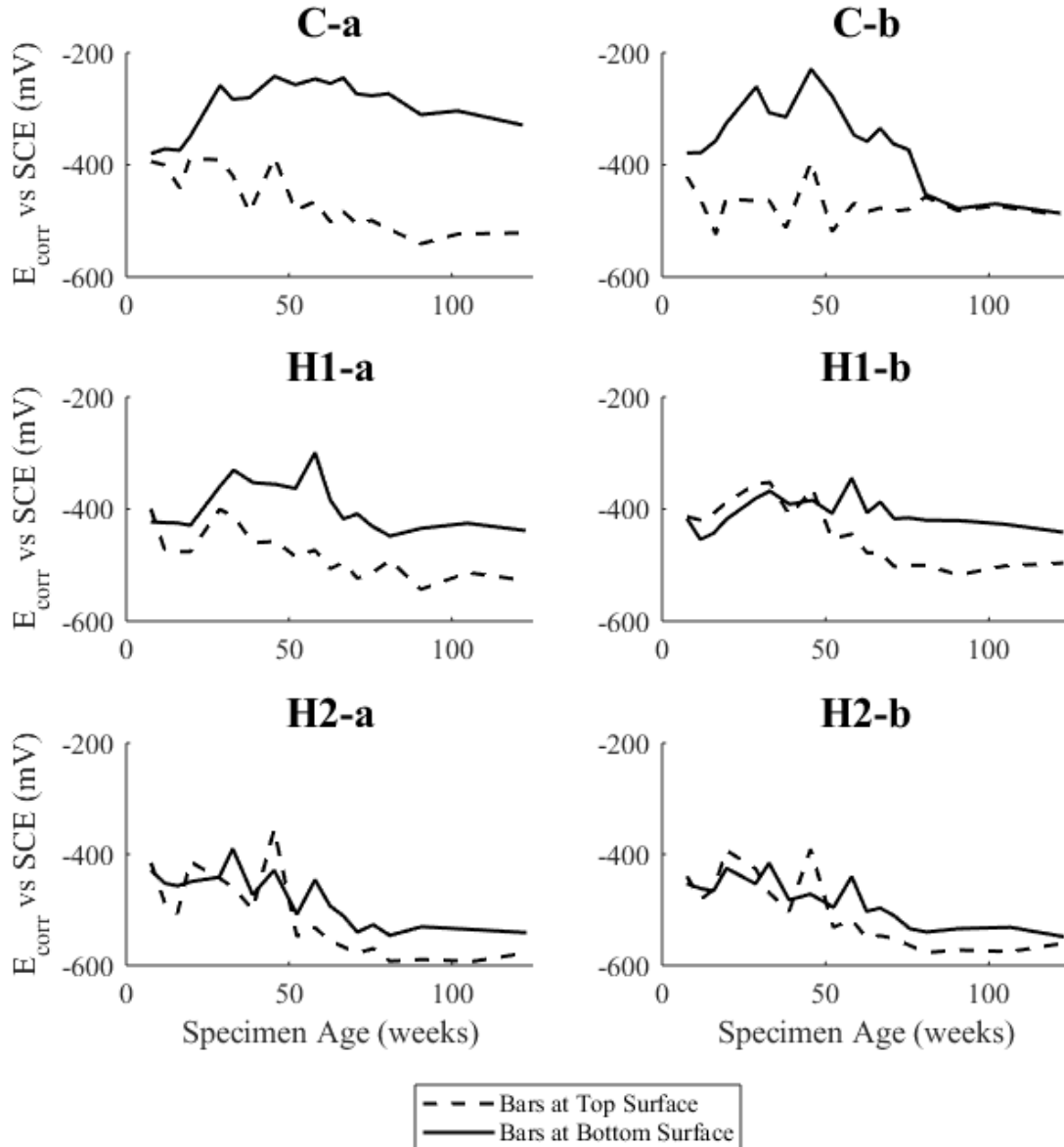
Figure 3 - 8: Corrosion potential for longitudinal bars of each column specimen.

A corrosion potential below -277mV vs SCE is proposed in ASTM C876-15 as having 90% probability of actively corroding (ASTM 2015). While all specimens exhibit corrosion potentials below this value early in the test, 'bottom' bars in the C specimens then hover around this value at around 25 weeks. Bars near the 'top' surface exhibit a lower (more negative) corrosion potential across all specimens, though the magnitude of the discrepancy between top and bottom bars

decreases from C to H1 to H2 specimens. This correlates the compressive strength, as the structure and surface cracking observations, which suggest that the C specimens had a stronger matrix, but with the development of shrinkage cracks, the 'top' bars proceeded to corrode due to increased local permeability. The lower compressive strength in the H1 and H2 specimens correlates with the more negative corrosion potential and thus higher probability of corrosion in the chloride-contaminated matrix.

Polarization resistance, R_P, was determined for each bar after alternating wet cycles, and the Tafel Slopes, β_a and β_c, were experimentally determined via Tafel scan. The Stearn-Geary Equation (Eq. 2 - 6) was then used to determine the corrosion rate and was normalized by rebar surface area to yield the corrosion current density, i_{corr} [μA/cm^2]. Plots showing R_P and i_{corr} throughout the corrosion exposure period are shown in Figure 3 - 9 and Figure 3 - 10, respectively. Corrosion rate plots are shown along with lines denoting the threshold values for active corrosion (0.1-0.2 μA/cm^2) according to the literature (Andrade et al. 1990).
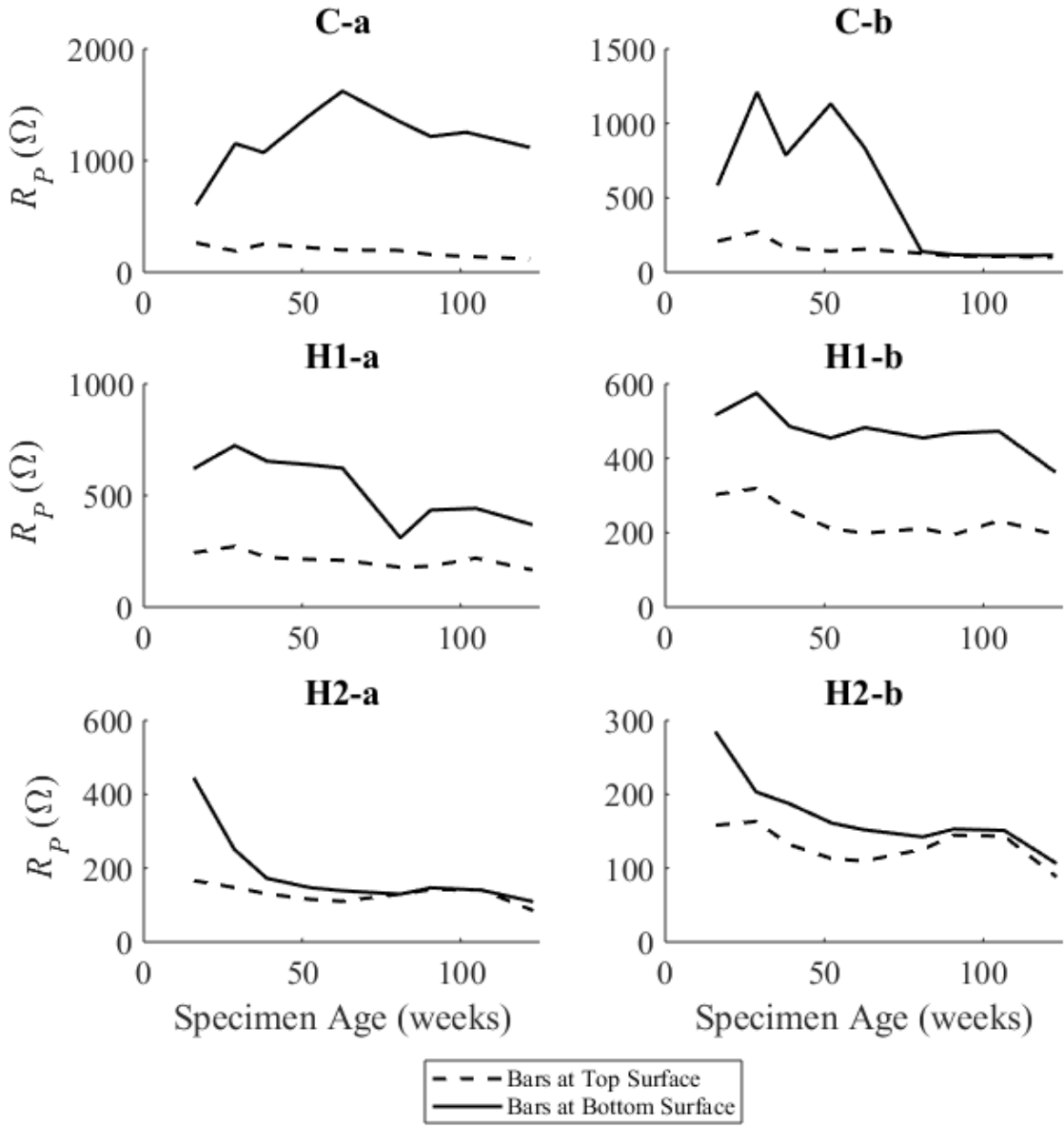
Figure 3 - 9: Polarization Resistance of column specimens over time.
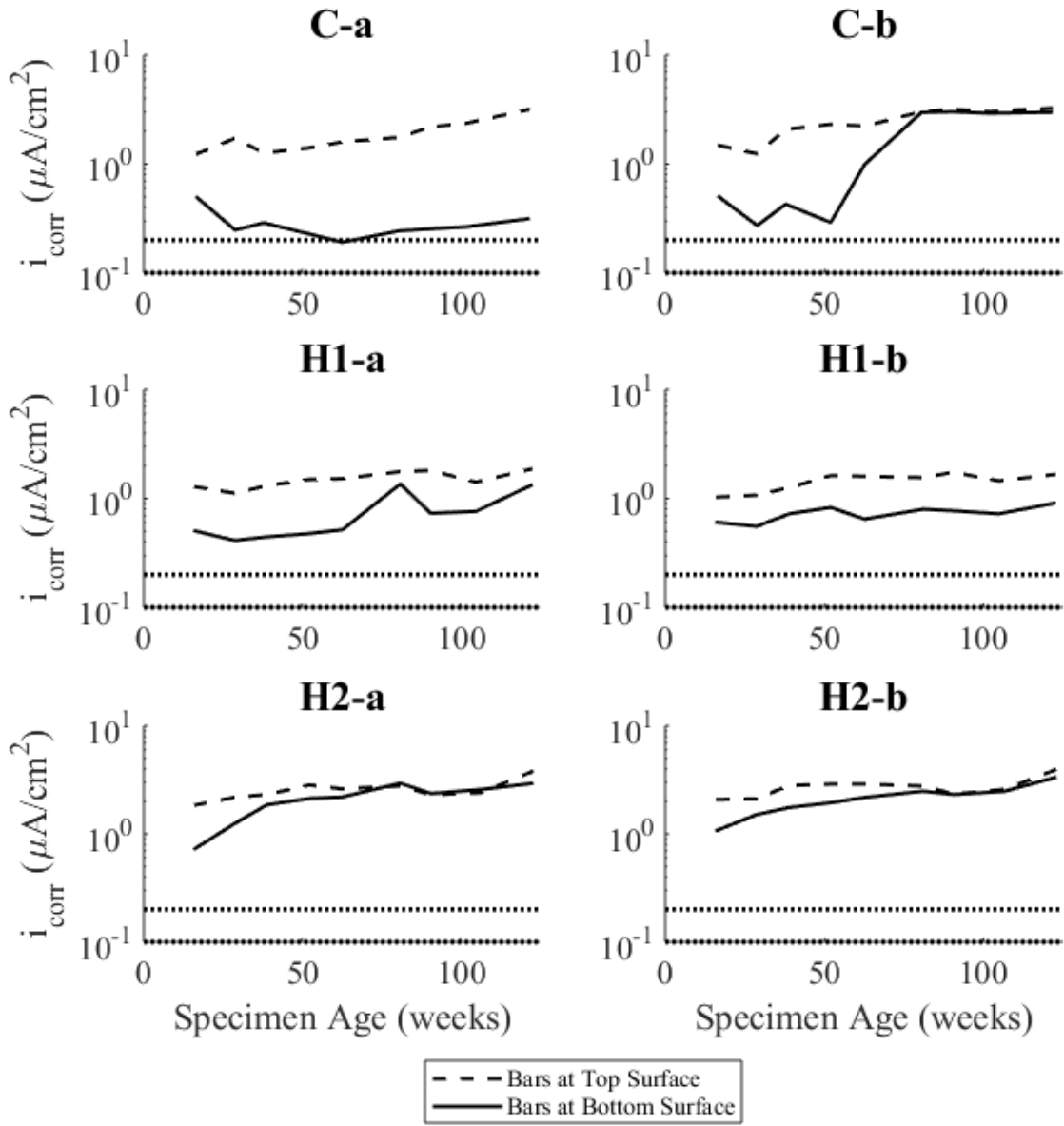
Figure 3 - 10: Corrosion rate of column specimens over time.

Plots of the corrosion rate agree with observations in corrosion potential measurements that all bars have a high probability of actively corroding, though 'bottom' bars in C-a remained close to threshold value throughout the propagation period. The corresponding bars in C-b start near this threshold but then increase to a rate similar to a match the 'top' rebars. It should be noted that surface cracking was not observed around these bars, indicating that reinforcement may have become electrically connected as the growth of corrosion products came into contact with transverse reinforcement. This hypothesis is further supported by mass loss measurements at the conclusion of the experiment. While this trend in i_{corr} was also observed in H2 specimens, the more gradual change in corrosion behavior and the presence of surface cracking along the 'bottom' bars suggests that these bars were actually corroding.

Corrosion rates of 'top' rebars are all in the same order of magnitude and are expected for natural corrosion (1-10 uA/cm^2) (Andrade et al. 1990). The corrosion rate does not exhibit any

stark increases with crack formation and growth, but the rate was observed to steadily rise over the course of the experiment, most clearly in the C specimens. While the expectation would be that corrosion rate would increase with crack growth, in cases where chloride is plentiful in the cover matrix, cracking would not bring about a major influx of chloride but would increase availability of oxygen at the bar surface. However, during corrosion rate measurements, the columns were submerged for 12 to 24 hours, which could mean that measured corrosion rates would be lower compared to rebars which had optimal access to air and moisture (Monteiro and Mehta 2014).

3.4.3 Mass Loss Predictions and Measurements

Cumulative mass loss was estimated by employing trapezoidal integration of the corrosion rate, I_{corr}, to approximate the charge transfer and subsequently calculating the mass loss using Eq. 3 - 1. Plots of progression of predicted mass loss are shown in Figure 3 - 11. An additional test point is displayed at 156 weeks (approx. 3 years), at the time of mass loss measurement. Following the final mechanical testing and rebar excavation, all rebar was chemically cleaned according to ASTM G1-03.

Table 3 - 4 lists the observed average mass loss for 'top' and 'bottom' bars from each column type (C, H1, and H2) along with their corresponding expected values from electrochemical measurements (Figure 3 - 11). Measured versus predicted mass loss for all rebars, presented normalized by rebar surface area, is shown in Figure 3 - 12.
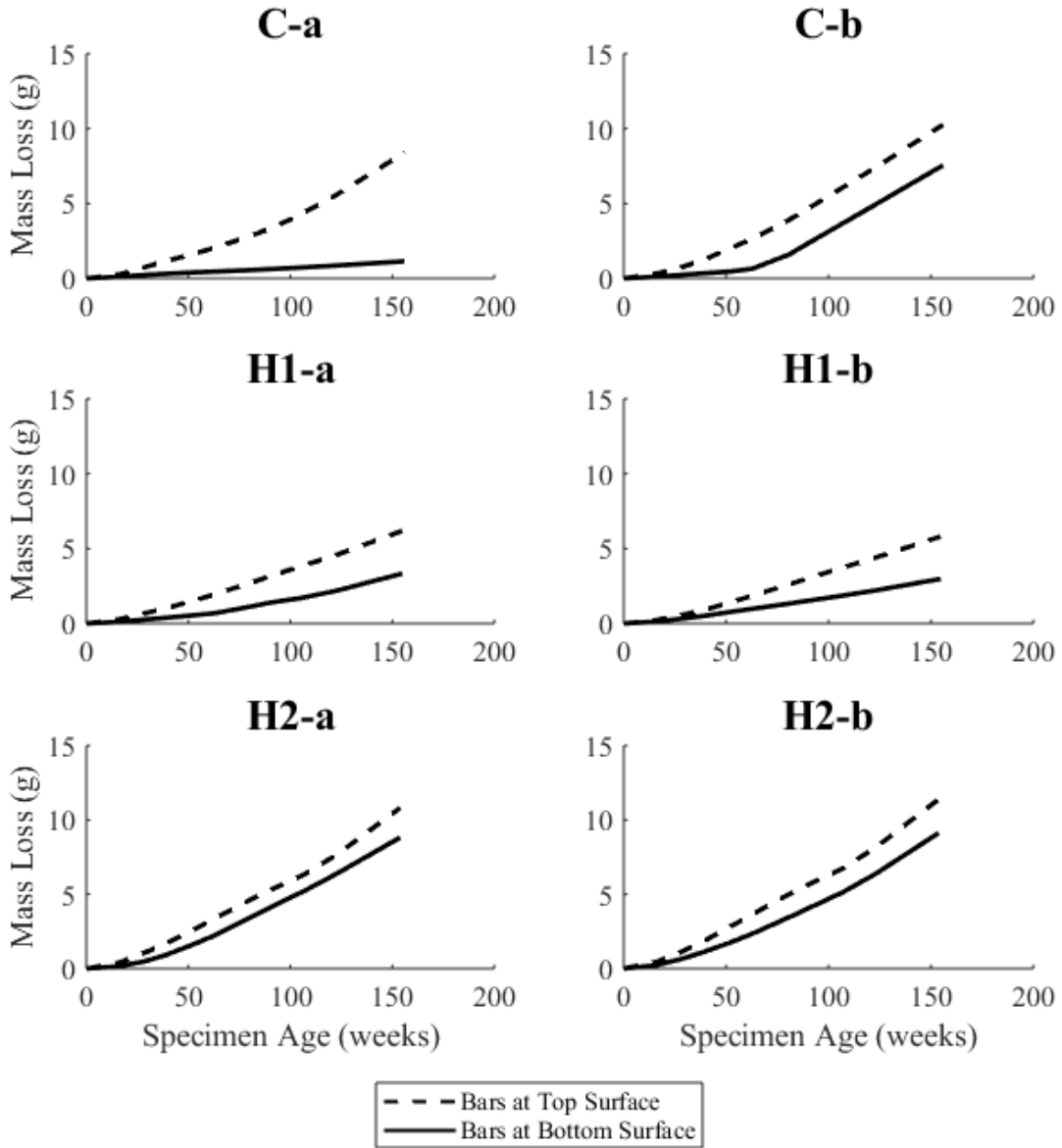
Figure 3 - 11: Expected mass loss based on corrosion rate measurements.

Table 3 - 4: Measured versus predicted rebar mass loss for different column types

	Measured (g)	Predicted (g)
C - 'top'	12.25	9.33
C - 'bottom'	1.70	4.35
H1 - 'top'	14.45	6.00
H1 - 'bottom'	2.90	3.15
H2 - 'top'	19.48	11.10
H2 - 'bottom'	9.75	8.97
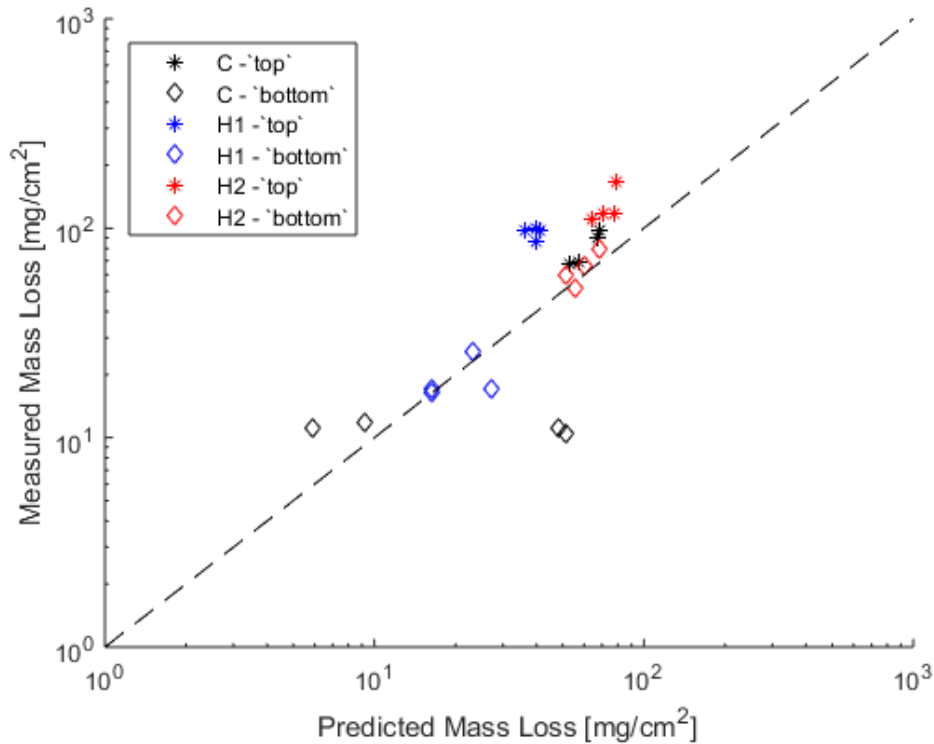
Figure 3 - 12: Predicted versus Measured mass loss for all rebars.

Predicted mass loss generally fell below the gravimetrically measured value, with one exception coming from one set of C 'bottom' bars that were observed to have a high corrosion rate (see Figure 3 - 9). It is more likely that their electrochemical measurements were altered by electrical connection to the 'top' reinforcement. Other outliers include 'top' reinforcement for H1 and H2 specimens, which had smaller crack widths than C specimens, but were found to have a larger mass loss at the conclusion of the experiment. This indicates that the corrosion rates for these specimens may have been higher when they were not submerged for electrochemical testing, as their limited supply of oxygen would be more rapidly consumed.

Corrosion damage patterns were also inspected following rebar excavation. Figure 3 - 13 shows corrosion patterns for typical 'top' and 'bottom' bars for specimen types C, H1 and H2. Each pair of images represents two sides of the same rebar. Scans of all reinforcing bars following mass loss measurements can be found in Appendix A-3.

Figure 3 - 13: Representative scans of corrosion damage to reinforcing steel following excavation. The first image in each pair shows the side of the rebar closest to side A, while the second image shows the side closest to side C.

More damage was found on 'top' bars than 'bottom' bars, with damage generally on one side of a given rebar, while the other side of the rebar remained largely unaffected. This damage pattern was found in all specimen types, in which damage occurred consistently on the side closest to side D during casting. This observation suggests that the region below reinforcing steel had a higher porosity than the region above. Due to the high flowability of all mixes it is possible that bleed water was trapped under rebars as it migrated to the surface, creating more porous zones on the under sides facing the bottom surface during casting. Corrosion products in chloride contaminated concrete have been suggested to be uniform (Gonzalez et al. 1990; Yuan et al. 2007) though this finding is consistent with other studies that determined that corrosion products will preferentially form in more porous zones or regions with defects even under a high chloride concentration (Hay and Ostertag 2019). This observation points to the importance of the interface during corrosion propagation, even in a chloride-contaminated environment.

'Bottom' bars for C and H1 specimens were largely undamaged, though some pitting was observed. In H2 specimens, the bottom bars showed similar damage patterns to 'top' bars, though the damage was less severe. Both H1 and H2 specimens exhibited regions of more localized corrosion with more uniform areas in between, while corrosion patterns were more uniform along the length of 'top' bars in C specimens. This is likely due to the uniform presence of cracking in C specimens, versus the discontinuous cracks in the H1 and H2 specimens. Corrosion products in H1 and H2 specimens were also found to be more densely packed onto the surface and were difficult to remove from the bar surface during chemical cleaning. Densification of corrosion products is expected in the presence of fiber reinforcement, also suggests that despite mass loss, H1 and H2 specimens retain their rebar-matrix bond better than C in the presence of corrosion damage.

It should be noted that the compressive strength of the C specimens was significantly higher than that of H1 and H2 specimens. A higher compressive strength would also indicate a higher resistivity and lower permeability and thus would lead to lower corrosion rate. If cracking in C specimens initiated due to shrinkage, then only rebar area near the crack would have access to oxygen and thus be exposed to corrosion damage. In H1 and H2 specimens, a lower compressive strength would correlate with the higher corrosion rate and corresponding mass loss.

3.4.4 Axial Stiffness Measurements

Axial stiffness measurements were taken at the beginning and end of the corrosion exposure period. Stiffness results were averaged for each column type and the results are shown in Table 3 - 5.

Table 3 - 5: Progression of average axial stiffness during corrosion exposure [MPa].

	4-week	24-week	140-week
C	155.3	148.6	150.8
H1	135.1	149.7	144.1
H2	141.8	146.3	148.6

Because spalling was not observed during the corrosion exposure period, no appreciable loss in stiffness was observed. Corrosion of reinforcement led to mass loss which in turn translates to loss in rebar diameter, but any small impact this may have had on column stiffness would likely

be counteracted by strength increase due to aging of the concrete. Finally, while cracking was observed, longitudinal cracking is unlikely to led to a meaningful loss in elastic axial stiffness. It should be noted that during excavation of reinforcing steel, the stainless steel transverse reinforcement was found to be nearly pristine. It follows that uncorroded hoops serve to bridge transverse cracks originating from longitudinal reinforcement. These findings suggest that in order for corrosion-induced spalling to occur, transverse hoops must be contributing to corrosion damage.

3.4.5 Monotonic Compression Behavior

Following the corrosion exposure period, one subset of columns (those labeled 'b' in electrochemical measurements) were subsequently tested in compression monotonically to failure. These tests were compared with uncorroded columns that were tested at one month. The results for each column type are shown in Figure 3 - 14.
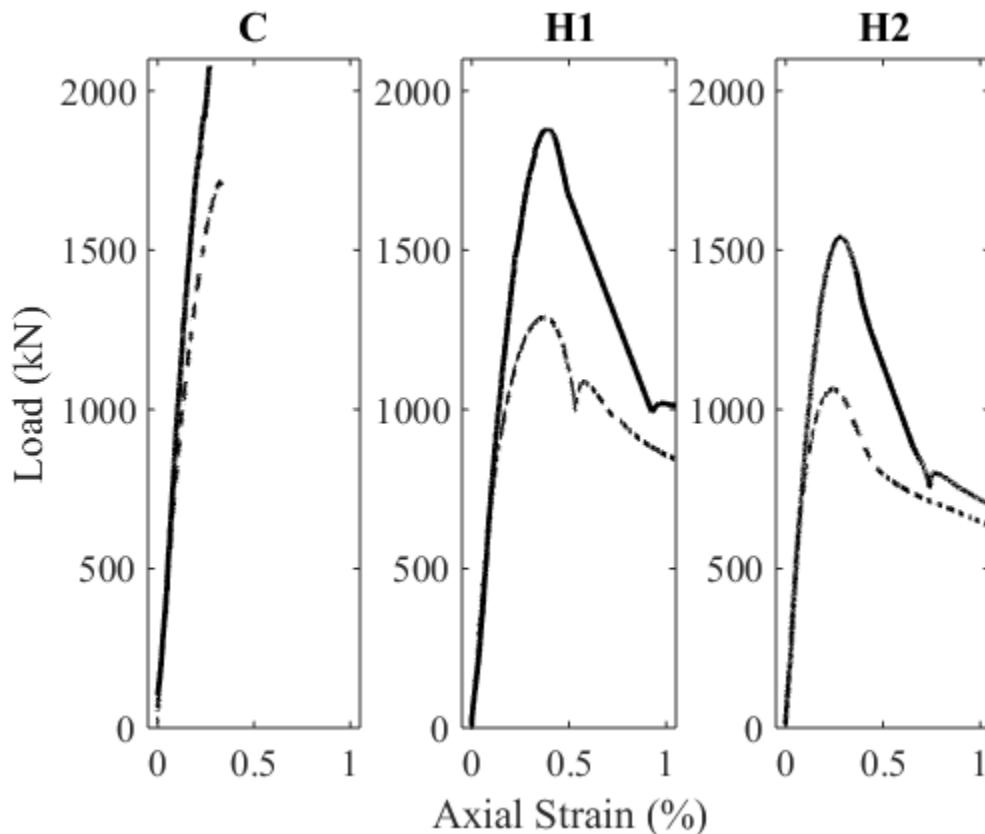
Figure 3 - 14: Load vs Strain behavior of columns, prior to corrosion exposure (dashed line) and at the end of the experiment (solid line).

As expected based on f'_c for each mix, C columns demonstrated the highest strength, while H2 displayed the lowest, both at the beginning and end of the experiment. The C columns had a sudden, brittle failure, which has been noted elsewhere for short, confined columns with carbon fiber wrapped ends (Turgay et al. 2010). This is contrasted by the SC-HyFRC specimens, which were able to show ductility even in the case of H2 specimens, which had reduced transverse reinforcement. Over the 140+ weeks between testing of the pristine column and the corroded column, strength continued to develop in the concrete, leading to an overall increase in strength

for all column types. The presence of large splitting cracks in the C columns may have contributed to the loss of ductility, though strength gain of the concrete may have also led the gross column strength to exceed the confined column strength.

3.4.5 Rebar Tensile Testing

The final test procedure was tensile testing of reinforcing steel following rebar excavation and mass loss measurements. Rebar from column specimens that did not undergo monotonic loading to failure (those labeled 'a' in electrochemical measurements), were tested in uniaxial tension. These bars were compared with pristine reinforcing steel from the same batch. A summary of the testing data can be found in Table 3 - 6. Loss of strength was measured by reduction in ultimate strength, f_u, and loss of ductility was measured by reduction in strain at the peak load. Strain at ultimate strength was chosen as a measure of ductility because in some tensile tests, necking and fracture of bars occurred outside of the region of interest of the extensometer, causing unloading in the region of interest and rendering it impossible to measure strain at fracture.

Table 3 - 6: Tensile test results for corroded rebars.

	Peak Stress (MPa)	% Reduction	Strain at Peak (mm/mm)	% Reduction
Pristine	669.9	--	0.1189	--
C - 'top'	638.8	4.7%	0.0783	34.1%
C - 'bottom'	658.4	1.7%	0.0847	28.8%
H1 - 'top'	618.8	7.6%	0.0646	45.6%
H1 - 'bottom'	656.2	2.1%	0.0870	26.9%
H2 - 'top'	598.3	10.7%	0.0554	53.4%
H2 - 'bottom'	643.5	3.9%	0.0818	31.2%

Corrosion of rebar led to a loss in material for all bars based on mass loss measurements (Figure 3 - 11). This took place as uniform section loss in some cases and localized pitting in others. Others (Almusallam 2001; Cairns et al. 2005) have found that rebar corrosion leads to a loss in nominal strength and ductility. 'Top' bars experienced the greatest reduction in both ultimate strength and strain at peak load, and reductions correlated closely with mass loss observed in corresponding specimen types. H2 specimens demonstrated the greatest mass loss and showed the greatest loss of nominal ultimate strength and ductility. While 'bottom' bars lost relatively little nominal strength, it should be noted that the decrease in ultimate strength was still pronounced.

3.5 Conclusion

Over a 125-week cyclic wet/dry exposure period, reinforced SCC and SC-HyFRC columns with admixed chlorides were monitored based on surface crack formation, electrochemical behavior and mechanical stiffness during corrosion propagation. Following this period one subset of columns from each group (C-b, H1-b, and H2-b) were tested in compression and compared with similar control columns tested at 28 days. All reinforcements were then excavated from column

specimens to determine mass loss over the total 156-week experiment. Rebars from columns that were not tested in compression (C-a, H1-a, and H2-a) were then tested in tension to determine their loss in nominal strength and ductility. The following conclusions can be drawn:

1. Admixed chlorides were effective at initiating an active corrosion state from the onset of the test, though large differences in compressive strength of the SCC and SC-HyFRC mixes limited the extent the results could be directly compared. Corrosion did not affect all bars equally in any of the columns with bars located at the 'top' surface during casting being more affected than bars at the 'bottom' surface. This difference was particularly notable in C specimens, whose high corrosion rates in 'top' reinforcement were likely enhanced to shrinkage cracking, while 'bottom' reinforcement remained largely unaffected.

2. Corrosion damage was concentrated on the side of reinforcement closest to the bottom surface during casting. This is likely due to bleed water from the highly flowable mix collecting under reinforcement during casting, leading to more porous matrix conditions on one side of reinforcement. This observation points to the importance of the rebar-matrix interface during corrosion propagation, as the opposite side of reinforcement was largely uncorroded even though it was also exposed to a high chloride content.

3. Surface crack formation in HyFRC was delayed, with denser corrosion products forming at the bar surface. The lower compressive strength likely contributed to increased corrosion rate and created a more porous rebar-matrix interface that accommodated more corrosion products.

4. Longitudinal cracking and subsequent crack widening and lengthening did not have a clear effect on measured corrosion rates in chloride-contaminated concrete, though rates were observed to increase gradually in C specimens as longitudinal cracks widened.

5. Discrepancies in mass loss measurements and predictions were found to be larger in 'top' bars in H1 and H2 columns. Gravimetric mass loss measurements at the conclusion of the experiment showed that corrosion rates electrochemical measurements led to underestimation of the rebar mass loss. This indicates that corrosion rates may have been higher either before or after electrochemical measurements (or both).

6. Stiffness measurements revealed no appreciable change in axial stiffness over the course of the experiment. Stainless steel transverse reinforcement did not corrode and served to bridge splitting cracks and prevent spalling.

7. Monotonic compressive loading at the end of the test showed that strength gain in the SCC and SC-HyFRC led to an overall increase in strength across all column types. Fiber reinforcement led to improved post-peak response of the columns regardless of transverse reinforcement ratio or level of corrosion-damage.

8. Reinforcement corrosion led to a loss in nominal ultimate tensile strength and ductility in all rebars tested in tension. Tensile strength loss was proportional to the percentage of mass

lost. Deeper pitting corrosion in SC-HyFRC columns led to a more pronounced loss in ductility.

4 Development of Hybrid Simulation to Investigate Plastic Hinge Region of a Single-Column Bridge

4.1 Introduction

Many reinforced concrete bridges are simultaneously exposed to the combined hazard of seismicity and corrosion damage. While the seismic performance of pristine RC bridges can be challenging to model on its own, the challenge associated with incorporating corrosion damage into these models has made this area sparsely studied. Hybrid simulation (HS) is well-suited to capture the non-linear response of bridges with pre-damaged components without the need to explicitly model these components. This chapter describes the development of an HS procedure to analyze the seismic performance of a single-column bridge in which the lower portion of the column is replaced with an experimental element. The experimental specimen is placed in a test setup that controls vertical, horizontal and rotational degrees of freedom using actuators and a spreader beam as the system is numerically exposed to three consecutive earthquake ground motions. A steel HSS section is used as the experimental element to calibrate the test setup, identify sources of error, and validate the HS procedure. A newly-developed OpenFRESCO experimental element was used to communicate scaled axial, lateral and rotational displacements to the reduced-scale experimental element that interfaces with a full-scale 3-dimensional OpenSEES bridge model.

4.2 Materials and Methods

4.2.1 Bridge Model

The bridge model utilized in this experiment is based on a single-column bridge structure over Highway 99 in Ripon, CA built in 2001. The model for the bridge was originally developed in OpenSEES by Kaviani (2011) as bridge 'A' and was created for research on the behavior of skewed bridge abutments in seismic events. For the purposes of this experiment, the skew of the bridge was set to zero degrees, as was the angle of application of ground motion (in longitudinal direction of bridge). In the research presented here, the abutments, deck, and upper portion of the column serve as the analytical substructure, while the lower portion of the column serves as the experimental substructure. An image of the bridge structure along with an elevation drawing is shown in Figure 4 - 1. A schematic drawing of the bridge model is shown in Figure 4 - 2.

(a)
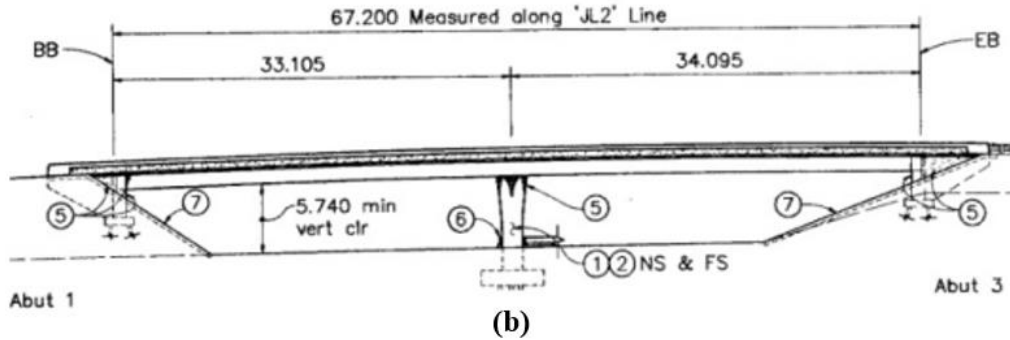
(b)

Figure 4 - 1: Google earth image of bridge structure (a) and elevation drawing (b) (Image sourced from Kaviani 2010).
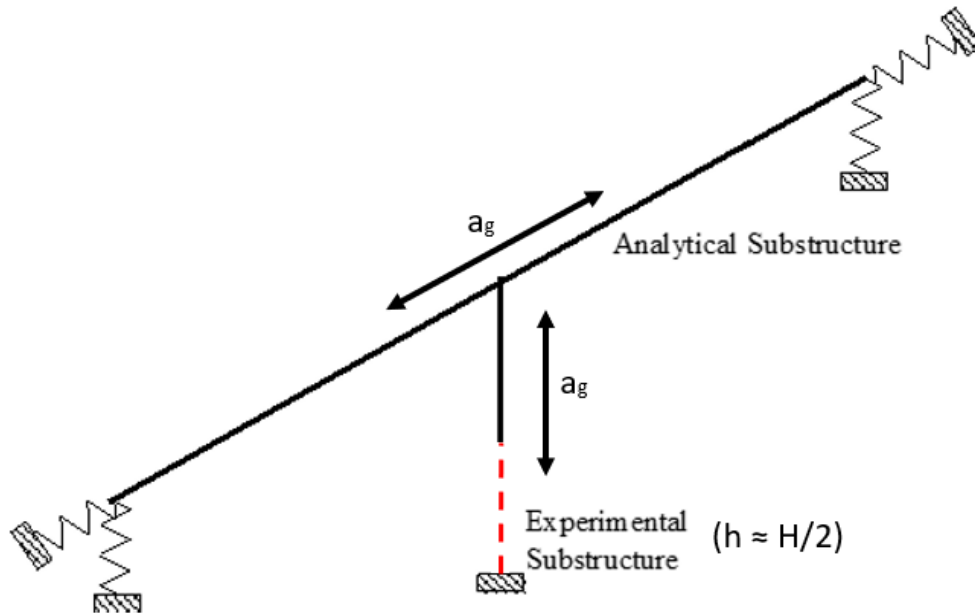
Figure 4 - 2: Schematic drawing of bridge model shown with abutment springs, deck and upper portion of column as the analytical substructure and the bottom of the column as the experimental substructure. Direction of the applied ground motion shown with black arrows.

The as-built column is circular in section and has a longitudinal reinforcement ratio of 2% and a height of 6m. The model was adjusted to match the reinforcement ratio (1.6%) and geometry (square) of columns presented in Chapter 3, which will also match the design of the RC and R/HyFRC experimental substructures to be presented in Chapter 5. A detailed section of the model

43

column is shown in Figure 4 - 3. In OpenSEES, the model utilizes Steel02 as the material model for steel, and Concrete02 as the material model for concrete, with the confined concrete core of the column accounted for through adjusted strength and ductility according to Mander et al. (1988). Plots showing the material models are shown in Appendix B-2 The bridge deck is a 3-cell continuous prestressed box girder, supported by seat-type abutments with elastomeric bearing pads and an integrated bent cap that connects to the single column at midspan (Kaviani 2010). The simplified bridge deck consists of two symmetric spans each 33.6 m long and a column height of 6.7 m. The deck is modeled with ten elastic elements on each span and the bent cap is rigid in the longitudinal bridge direction, modeled with an elastic element with increased stiffness spanning between the top of the column and the centroid of the deck, where it is joined with deck elements, as modeled by Kaviani (2010). The abutments follow a simplified model developed by Kaviani (2010). A list of select dimensions and relevant properties of bridge 'A' and the associated model can be found in Table 4 - 1. A full list of properties for bridge 'A' can be found in Appendix B-1.
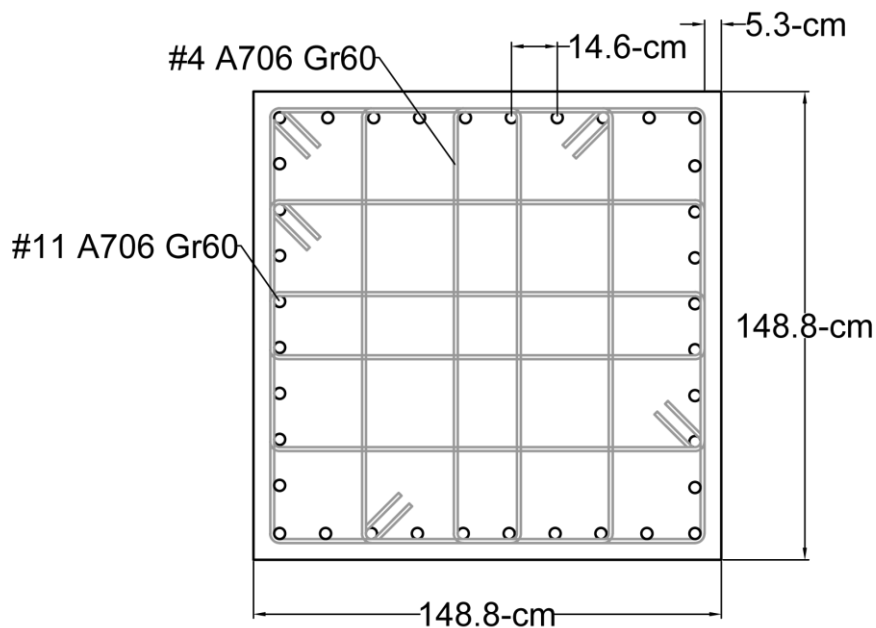

Figure 4 - 3: Modeled cross-section of the column of interest (Drawing courtesy of Ian Williams).

Table 4 - 1: List of select properties of bridge 'A' and model.

	As-Built	Model
Bridge Length	Total: 67.2 m Span 1: 33.1 m Span 2: 34.1 m	Total: 67.2 m Span 1: 33.6 m Span 2: 33.6 m
Column Height	6 m	6.7 m
Column Section Dimensions	1.68 m diameter (circular)	1.49 m x 1.49 m (square)
Reinforcing Steel	ASTM A706 $\rho_l = 2\%$ $\rho_t = 0.8\%$	Steel02 $\rho_l = 1.6\%$ $\rho_t = 1.2\%$
Concrete	$f'_c = 34.5$ MPa	Concrete02 $f'_c = 34.5$ MPa $f'_{cc} = 44.8$ MPa

It should be noted that degrees of freedom that were not controlled during HS were held fixed in the model. This includes deformation out-of-plane of the bridge (transverse direction), as well as torsion of the bridge column and torsion of the bridge deck.

4.2.2 Experimental Substructure

A steel hollow structural section (HSS) with dimensions 127x127x9.5mm (5x5x⅜ in) ASTM grade A500 B/C with a length of 609.4 mm was selected as the experimental substructure to calibrate the HS system. A drawing of the experimental substructure used in the calibration experiments is shown in Figure 4 - 4 with section properties listed in Table 4 - 2. The specimen was introduced to calibrate the system for a reduced scale RC specimen with a scale factor of 1:8.37 (to be presented in Ch 5). The same scale factor is applied to the steel specimen presented in this chapter. This scale factor is applied to displacement commands sent to the actuators and to force measurements collected by the DAQ.
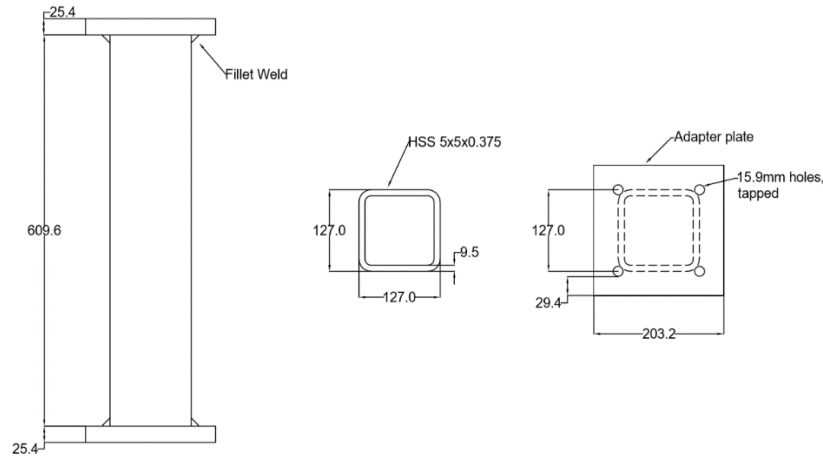
Figure 4 - 4: Plan and elevation details of the experimental substructure.

**Table 4 - 2**: Section properties of experimental specimen.

Section Type	AISC HSS 5x5x⅜ (127x127x9.5mm)
Steel Type	ASTM A500 B/C
fy	> 317 MPa
fu	> 427 MPa
E	200 GPa
Length	609.4 mm

In OpenSEES/OpenFRESCO, the experimental substructure is defined by a beamColumn experimental element (Schellenberg et al. 2009). Initial stiffness properties for the experimental element are determined through the stiffness determination procedure described in Section 4.3.2.

4.2.3 Experimental Setup

The physical testing frame utilizes three servohydraulic actuators, as shown in Figure 4 - 5, with one 260kN actuator applying lateral load and two 220kN actuators applying vertical load and rotation via a spreader beam. The actuators are mounted to a reaction frame and receive computed displacement commands from an MTS FlexTest controller (The FlexTest consists of both a PID Controller component and a Data Acquisition (DAQ) component). The OpenSEES model interfaces with the controller through OpenFRESCO to send the computed displacements to the actuators. Forces are measured by load cells attached to the actuators and this information is communicated back to the MTS FlexTest DAQ, which relays forces back to OpenSEES via OpenFRESCO. A schematic of this communication line is shown in Figure 4 - 6. The time-history analysis performed during HS consists of solving the equations of motion for the structure, with a given acceleration input at each time step. OpenSEES then solves the equations for the structure to determine displacements, communicates these displacements to OpenFRESCO, which then sends them as commands to the MTS FlexTest controller, which in turn commands a displacement

46

in the actuators. The applied forces are then measured by load cells on the actuators and sent back to the DAQ, which passes them on to OpenFRESCO where they undergo a transformation and are communicated back to the model in OpenSEES as response forces to compute the restoring force vector.
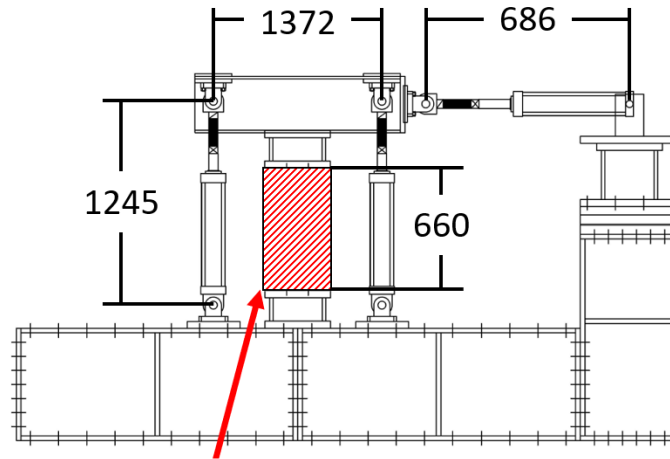
Figure 4 - 5: Experimental test frame (dimensions shown in mm) (Drawing courtesy of Ian Williams).
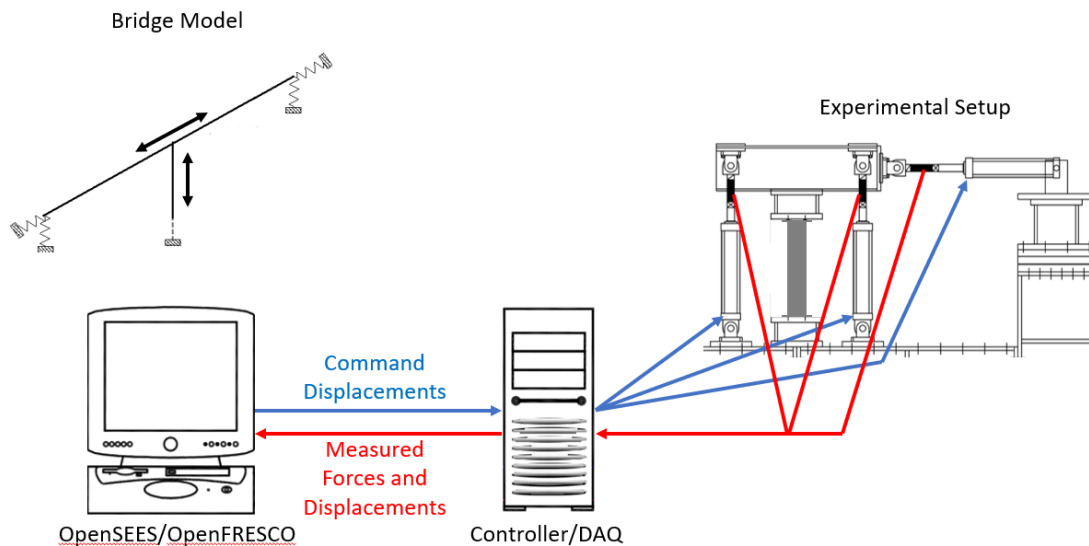
Figure 4 - 6: Schematic diagram showing communication path for commands and measurements during hybrid simulation.

4.2.4 Development of New OpenFRESCO Experimental Setup Command

A new experimental setup command was created in OpenFRESCO to communicate displacements to the controller and to receive force measurements from the DAQ. This setup was based on the ThreeActuators experimental setup shown in Figure 4 - 5, but was updated to allow the setup to interface with a 3D OpenSEES model. The new command also allows for a rigid offset to account for any distance between the line of action of the horizontal actuator and the node of interest. A model of the updated Experimental Setup command is shown in Figure 4 - 7.

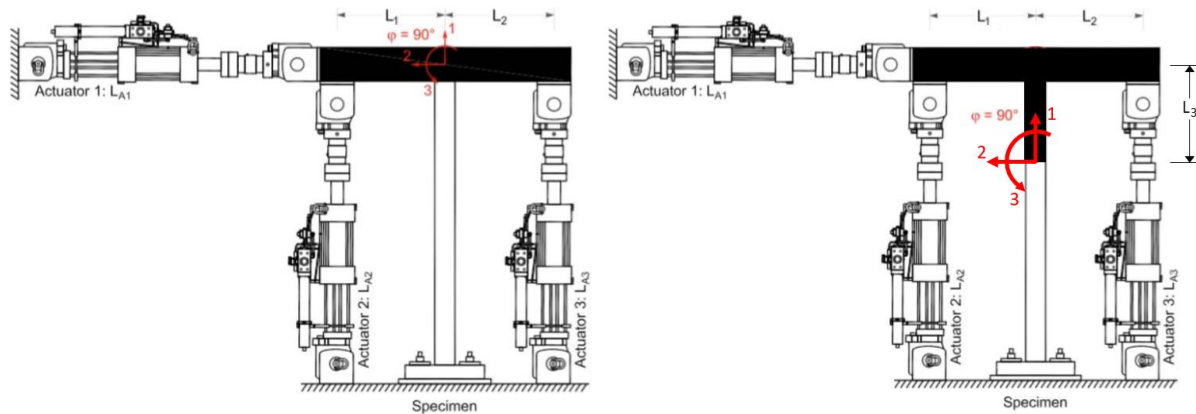**Figure 4 - 7**: Original ThreeActuators Setup (Left) and updated ThreeActuators Setup (Right) (After Schellenberg et al. 2009).

4.2.5 Ground Motion Selection

The HS procedure utilizes three ground motions, namely 1999 Chi Chi, Taiwan (referred to as GM1), 1979 El Centro, USA (referred to as GM2), and 1994 Northridge, USA (referred to as GM3). The 5% damped response spectra can be seen in the plot in Figure 4 - 8, with a vertical line denoting the fundamental period of the simulated bridge. The horizontal and vertical plots containing acceleration versus time for the series of ground motions is plotted in Figure 4 - 9. Ground motions were selected from the Pacific Earthquake Engineering Research (PEER) center Database, and were selected as relative small, medium, and large ground motions. These ground motions have both horizontal and vertical components and the three are applied sequentially during HS such that the damage observed is cumulative. It is important to note that ground motions were not selected based on any site hazard analysis, but rather to demonstrate behavior of the bridge of interest under relative small, medium, and large scale excitations. A time step of 5 ms is used in the time history analysis, while HS is conducted approximately ten times slower than real-time.
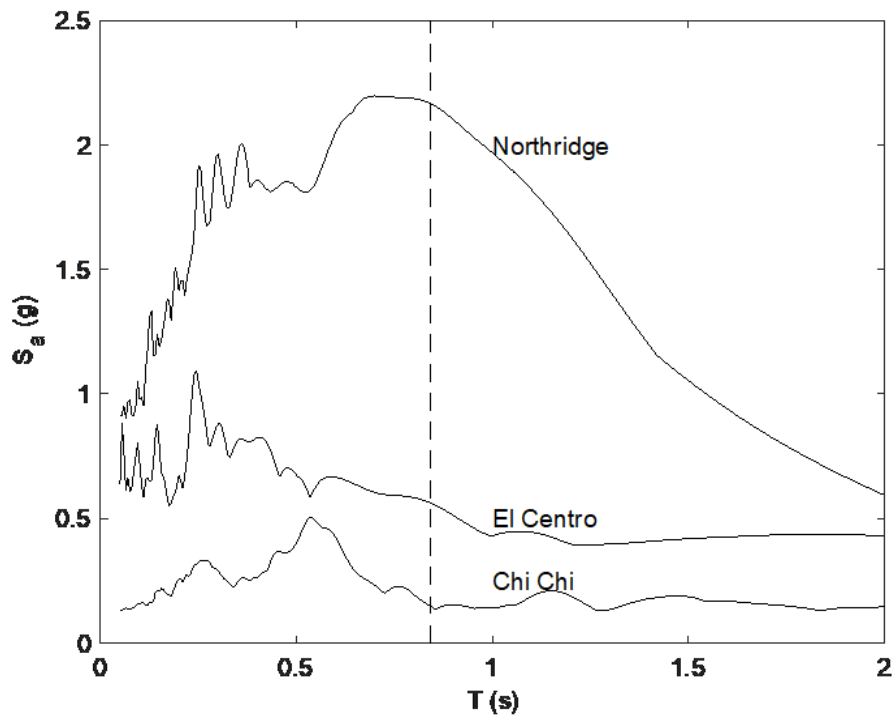
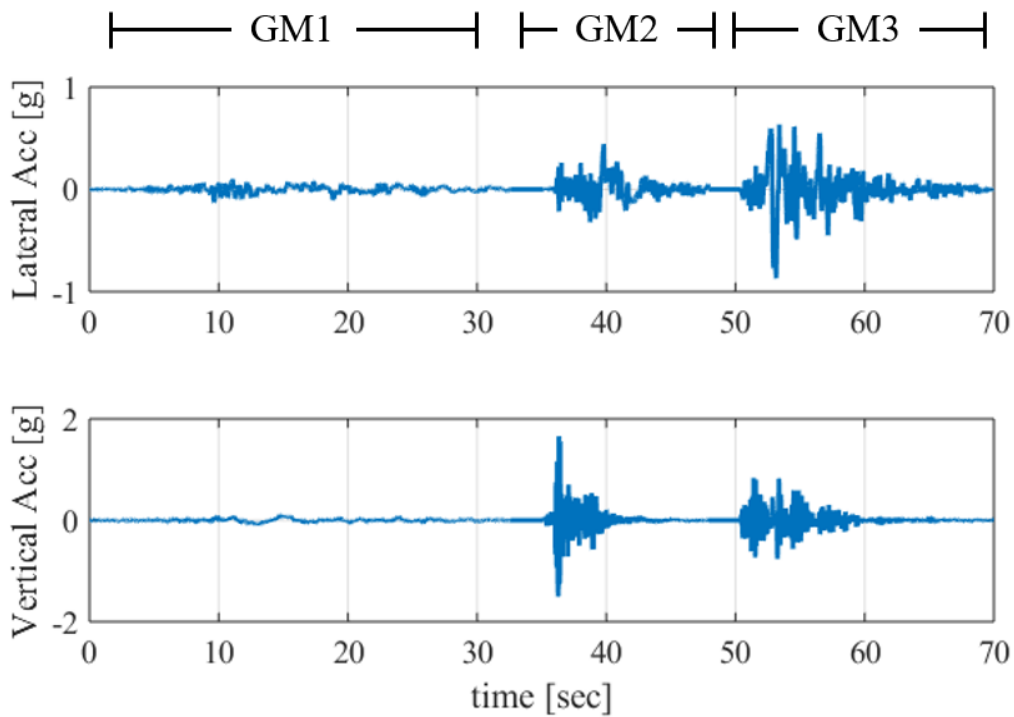**Figure 4 - 8**: Response spectra of ground motions used in HS (5% damping).

Figure 4 - 9: Acceleration time history for the series of three ground motion used in HS.

49

4.3 Experimental Procedures

4.3.1 Gravity Load Application

Displacement control of axially stiff members has been reported as problematic by others due to resonance with the oil column stiffness in actuator (Chae et al. 2018). Initial attempts to control the small axial displacement in the column due to gravity loading were unsuccessful. This led to the creation of a bypass in which the gravity load was applied to the experimental element manually. In the model, this initial load in the experimental specimen was accounted for through the following procedure:

1. The node connecting the experimental substructure to the analytical substructure was fixed in the vertical direction.
2. The bottom node of the experimental element was released in the vertical direction and the expected gravity load was applied upward to counteract the downward gravity load and prevent the development of an unbalanced force.
3. The bottom node of the experimental element was then once again fixed in the vertical direction and the node connecting the experimental and analytical substructures was released in the vertical direction.
4. In the first time-step of the ground motion, the experimental specimen, experimental element and analytical superstructure were all allowed to come into equilibrium. The displacement commands sent to the experimental specimen were given relative to the starting displacement rather than absolute.

4.3.2 Stiffness Determination

An accurate simulation requires a good initial guess of the tangent stiffness of the system (Mosalam and Günay 2013). In order to limit error propagation during HS, the flexibility of the test setup must be accounted for in the initial stiffness values of the experimental element. A test procedure was developed to impose small cyclic displacements on the system to reveal the stiffness coefficients of the experimental specimen in the test frame. In this procedure, the DOF of interest of the specimen was displaced while all other DOFs were held constant. This allowed for the determination of the stiffness of the experimental substructure accounting for any additional flexibility provided by the test frame. The procedure was used to determine axial stiffness, lateral stiffness, and rotational stiffness. The off-diagonal terms in the stiffness matrix were also determined by averaging the measured moment during the lateral stiffness determination and the measured lateral force during the rotational stiffness determination.

4.4 Results and Discussion

4.4.1 Stiffness Determination

Prior to running the HS experiment, the stiffness of the experimental specimen in the testing frame was determined and compared with expected values for the section. The stiffness was determined by commanding a small displacement in the degree of freedom of interest while holding other degrees of freedom fixed. The results of the stiffness determination are shown in Figure 4 - 10 with the slopes of the curves shown in Table 4 - 3 as the 2D stiffness matrix for the element. It should be noted that in the model, the full 3D stiffness matrix was approximated using these values, though all other DOFs were held fixed and are thus not shown here.
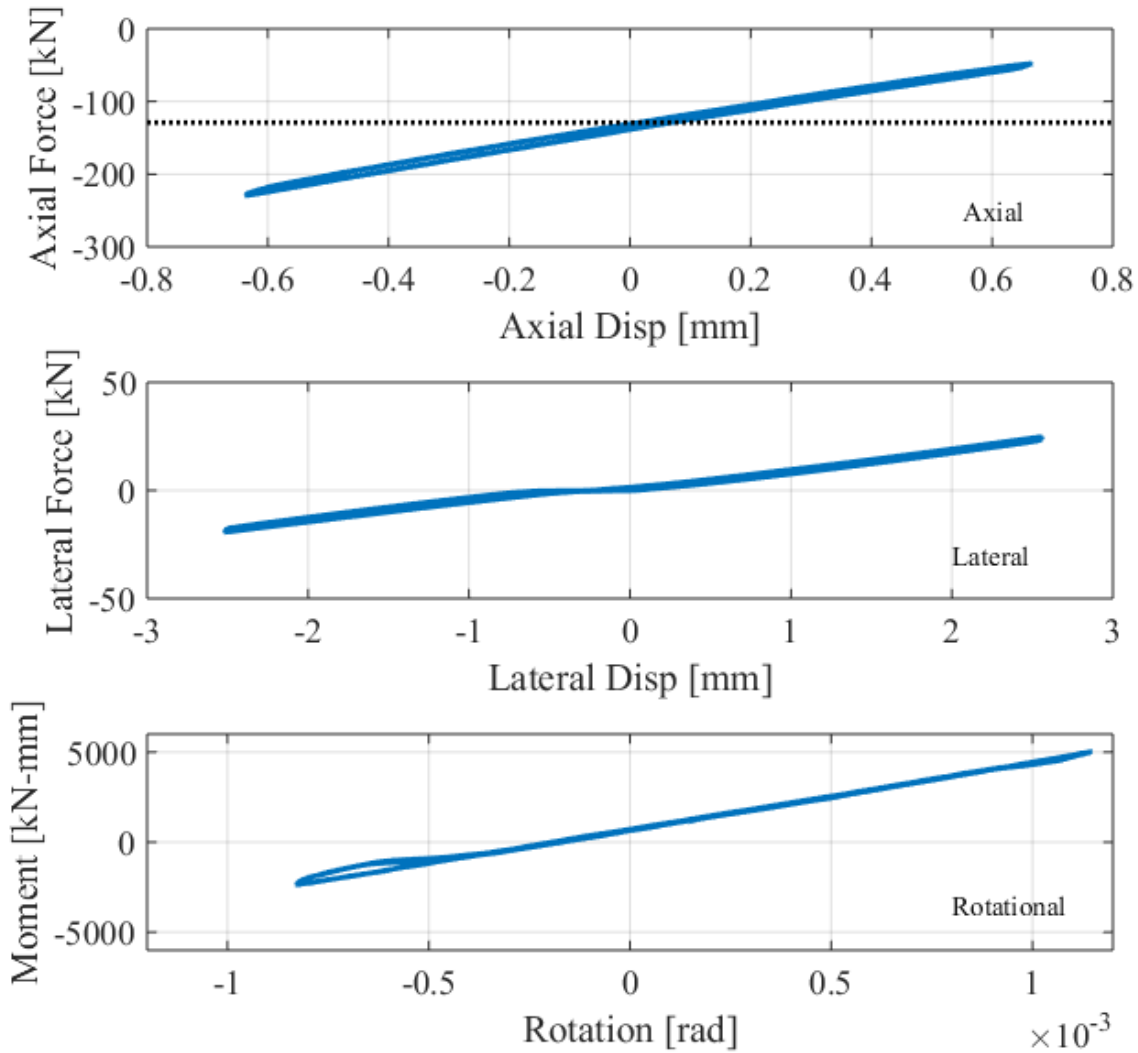
Figure 4 - 10: Plots of cyclic loading for stiffness determination for experimental element. The stiffness was taken to be the average slope for each plot.

Table 4 - 3: Stiffness matrix coefficients from stiffness determination procedure.

	139.9 kN/mm	0	0
$K_{measured} =$	0	8.42 kN/mm	-2847 kN
	0	-2847 kN	3.245e6 kN-mm/rad

Backlash (gaps in the pin connection between the actuator and the test setup, such that when the actuator force goes from positive to negative, there is a zero slope plateau over a distinct displacement) is evident in the lateral force displacement relationship in Figure 4 - 10. In order

to reduce the backlash (and thus reduce errors), a new connection system must be created; this will be discussed further in Chapter 5.

Given the tabulated properties of the steel section, it was expected that the column would have the ideal stiffness values shown in Table 4 - 4. Due to the loading frame, there was an observable loss in stiffness from prediction to actual. Included in the table are the respective proportions of actual stiffness compared to ideal stiffness.

Table 4 - 4: Ideal stiffness matrix coefficients and ratio of measured stiffness to ideal stiffness (%).

	EA/L = 1307.7 kN/mm (10.7%)	0	0
$K_{predicted} =$	0	$12EI/L^3$ = 95.7 kN/mm (8.8%)	$-6EI/L^2$ = -29157.5 kN (9.8%)
	0	$-6EI/L^2$ = -29157.5 kN (9.8%)	4EI/L = 11.850e6 kN-mm (27.2%)

The measured stiffness of the experimental specimen in the test frame is approximately one tenth of the expected values for all terms except K_{33}, which was above one fourth. Two major sources of error were observed in the test frame: The first was the observed backlash in the horizontal actuator, which had contributions from both the rod end and the clevis attachment. The backlash can be observed in the 'lateral' plot Figure 4 - 10, where the horizontal stiffness plateaus when it crosses zero force. The second source of error is likely from flexibility in the loading frame at the spreader beam (for the vertical and rotational DOFs) and in the pedestal holding the lateral actuator (for the horizontal DOF). While the flexibility of the loading frame cannot feasibly be improved in the scope of this experiment, the backlash can be reduced, with improvements discussed in Chapter 5.

4.4.2 Hybrid Simulation for Ground Motion Scaled by 0.375

Prior to HS, an analytical simulation was run in which the experimental element was replaced with an elasticBeamColumn element with the stiffness properties matching the initial stiffness of the experimental substructure (determined in section 4.4.1). This analytical simulation is compared with the HS utilizing the experimental specimen. Figure 4 - 11 shows the displacements (at model scale) recorded at the control point node at the interface between the analytical substructure and the experimental substructure. The reaction forces at the control point were recorded and are displayed versus time in Figure 4 - 12. The results are compared with the corresponding node in the analytical simulation. Both simulations utilized a series of three consecutive ground motions (described in section 4.2.5), with an applied scale factor of 0.375 and the x-axis shows simulation time.
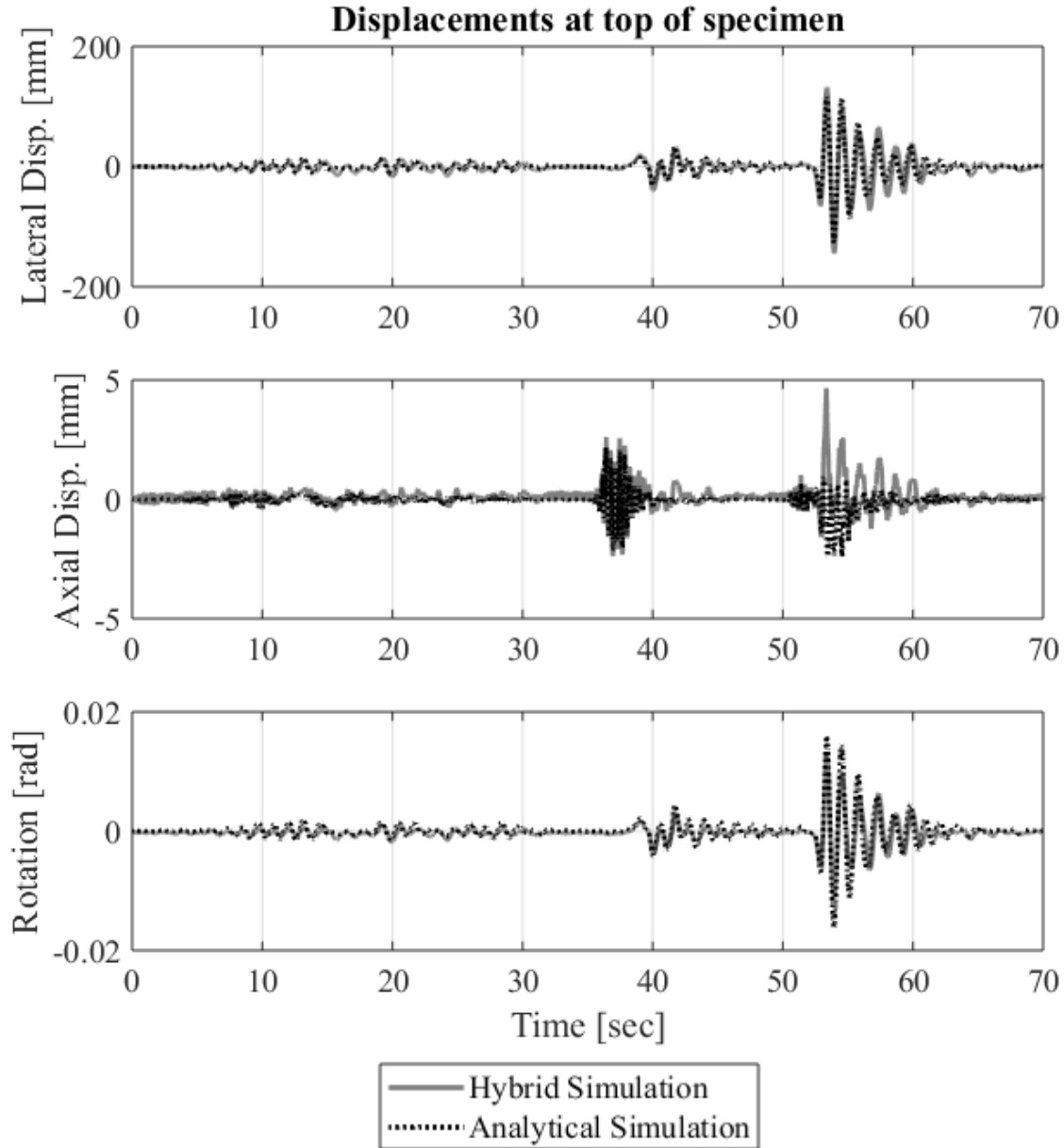
Figure 4 - 11: Displacement versus time at the top of the experimental specimen for ground motion series scaled by 0.375.

Lateral displacements in the HS show good agreement with the analytical simulation in the reduced scale series of ground motions where little to no yielding of the column is expected. In GM3, the HS response exceeded the analytical response. As lateral deformations increased, in the second and third ground motions, the lateral deformations appeared to influence the vertical displacements. Lateral deformations in the HS are slightly larger than the analytical simulation, while the opposite is true for the rotational degree of freedom.
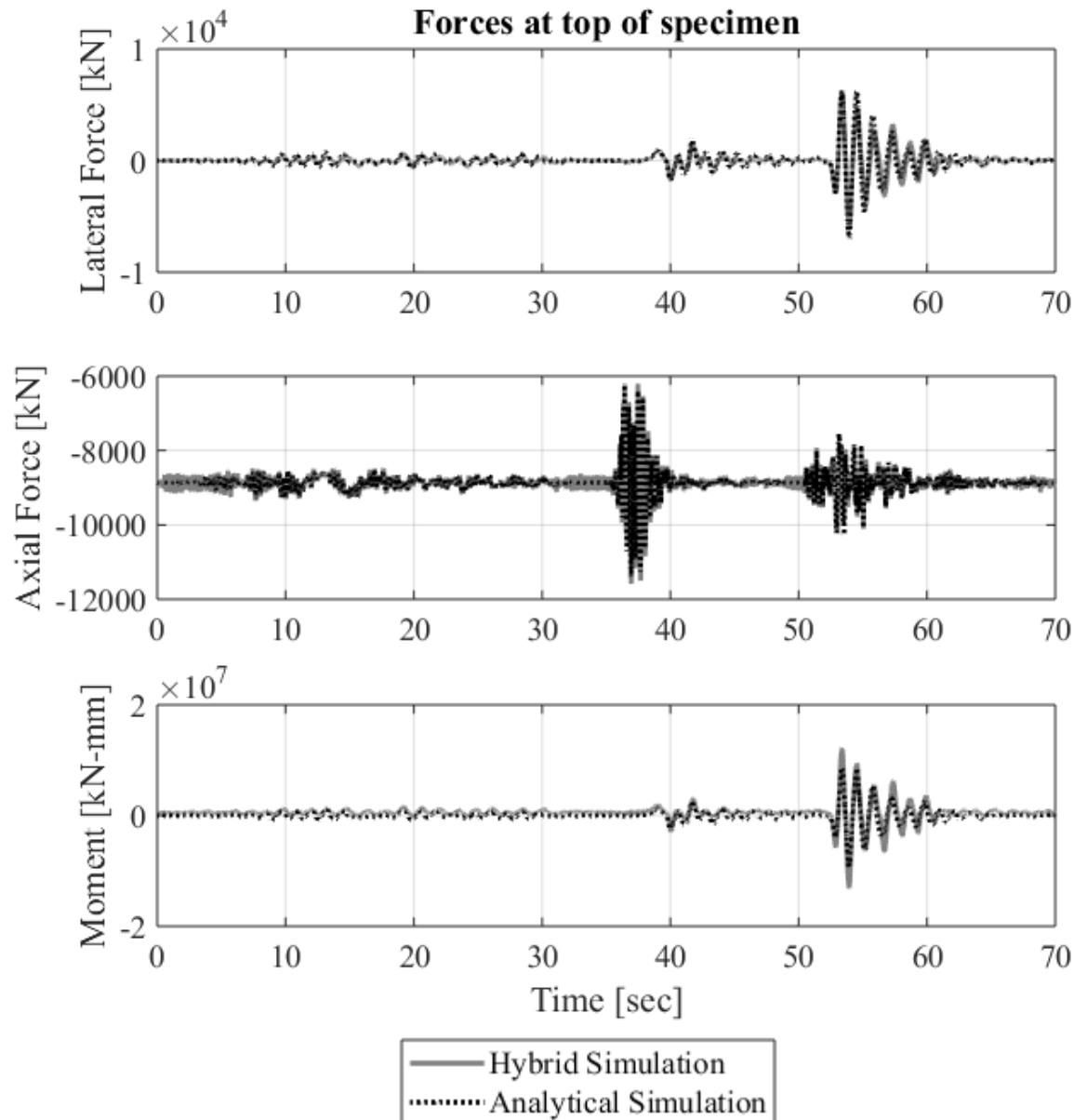
Figure 4 - 12: Forces versus time at the control point for ground motion series scaled by 0.375.

The force response does not suffer from the same issues as the displacement response during the larger lateral displacements of GM2 and GM3. The HS response showed a larger lateral force and moment than in the analytical simulation. Additionally in the vertical response, it can be seen that oscillations occur, and are especially visible in between ground motions in Figure 4 - 13. The frequency of these oscillations was determined to be approximately 7Hz, and was attributed to excitation of higher modes in the axially stiff test specimen. Similar oscillations were observed by Chae et al. (2018), though the oscillations in their HS led to an unstable response, while the oscillations in this case remained stable. These oscillations were reduced through the introduction of additional damping added to the model, which followed a Rayleigh model and applied 20% damping at a 7Hz oscillation. This model was selected to minimize the impact on lower frequency modes. Additionally, the Generalized-α integration scheme was used to maximize the numerical

damping applied to the model. Figure 4 - 13 shows an FFT to reveal the frequency of tracking errors in individual actuators before and after adding additional damping to the model. A spike at approximately 7Hz is seen in Figure 4 - 13(a) and is reduced in Figure 4 - 13(b).
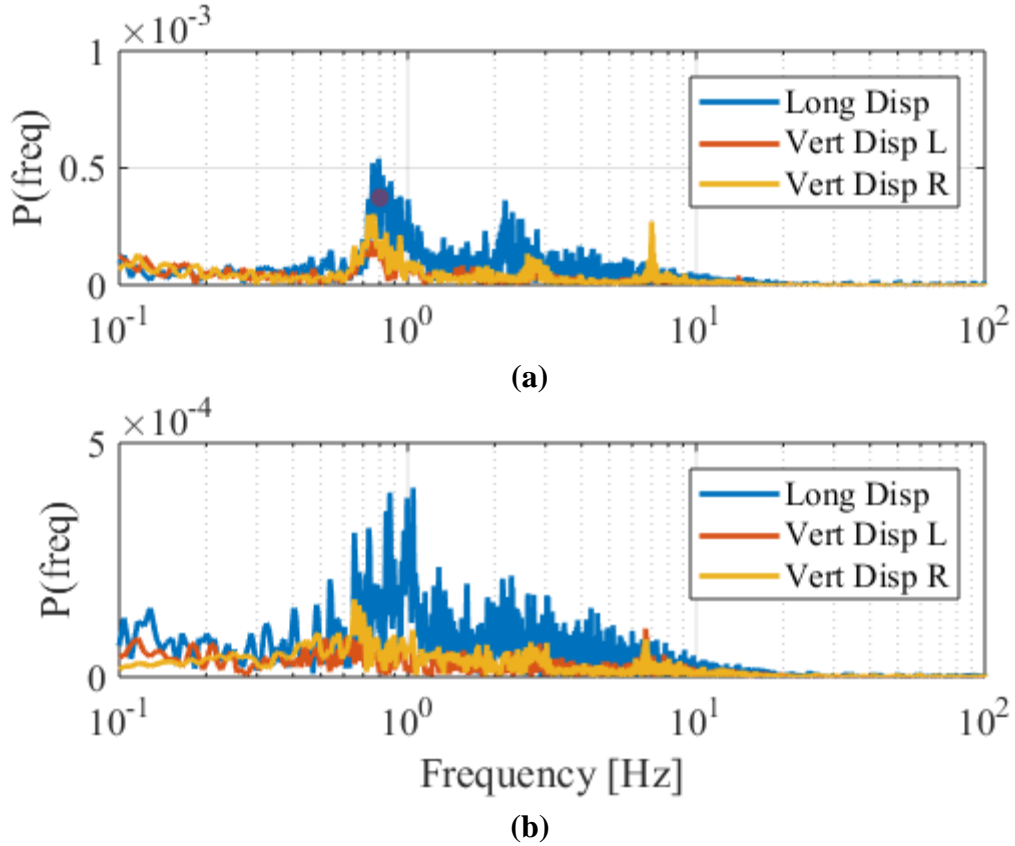

(a)

(b)

Figure 4 - 13: FFT of actuator tracking errors for force response data before (a) and after (b) the addition of 20% Rayleigh damping at 7Hz to reduce the excitation of higher modes.

The force versus displacement response for the lateral DOF is plotted in Figure 4 - 14 to compare the stiffness of the simulated experimental element with HS, and to observe the overall response. Backlash in the lateral actuator can be seen in the plateau at the origin in Figure 4 - 14. The stiffness prediction is a good match for the system, though the elastic element used in the analytical simulation cannot capture backlash or the small amount of hysteresis observed during HS.
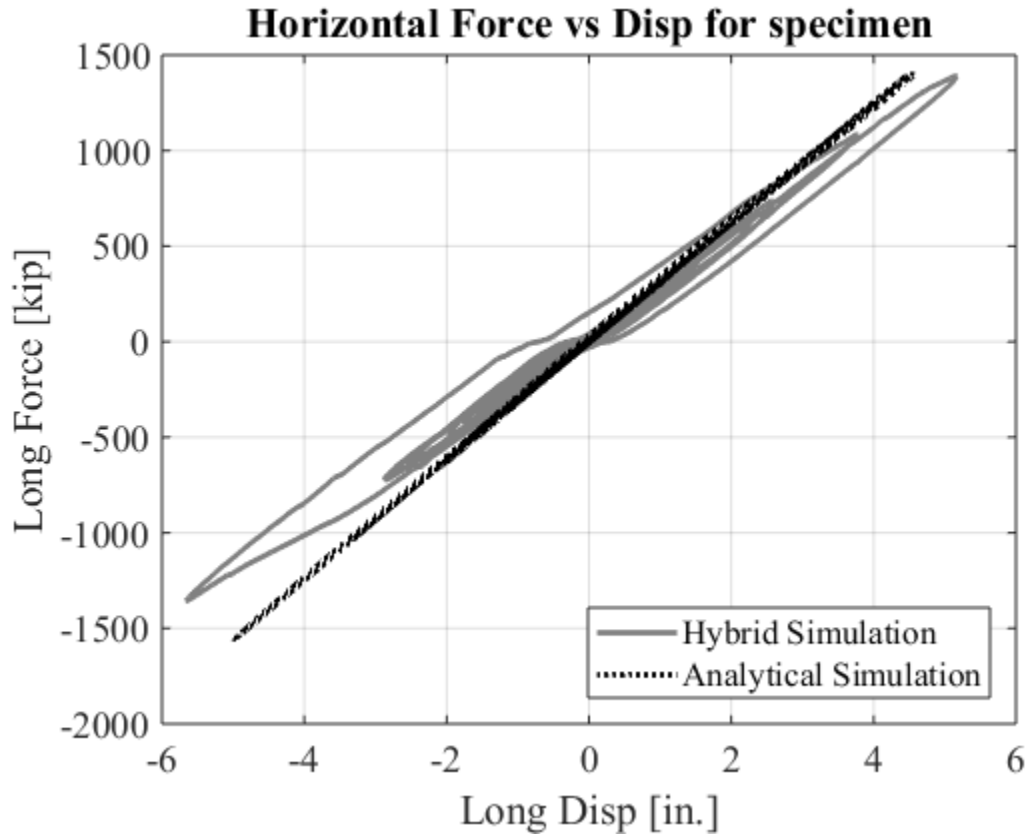
Figure 4 - 14: Force versus displacement relationships for HS and analytical simulation with ground motion scaled by 0.375.

4.4.3 Hybrid Simulation for Ground Motion Scaled by 0.5

Following the first reduced-scale ground motion, the factor was incremented to 0.5. In this analysis, the upper portion of the column was switched from an elastic beam column element in OpenSEES to a force-based nonlinear beam column element. The displacement of the control point during HS and analytical simulation for a ground motion with a reduced scale of 0.5 are shown in Figure 4 - 15.
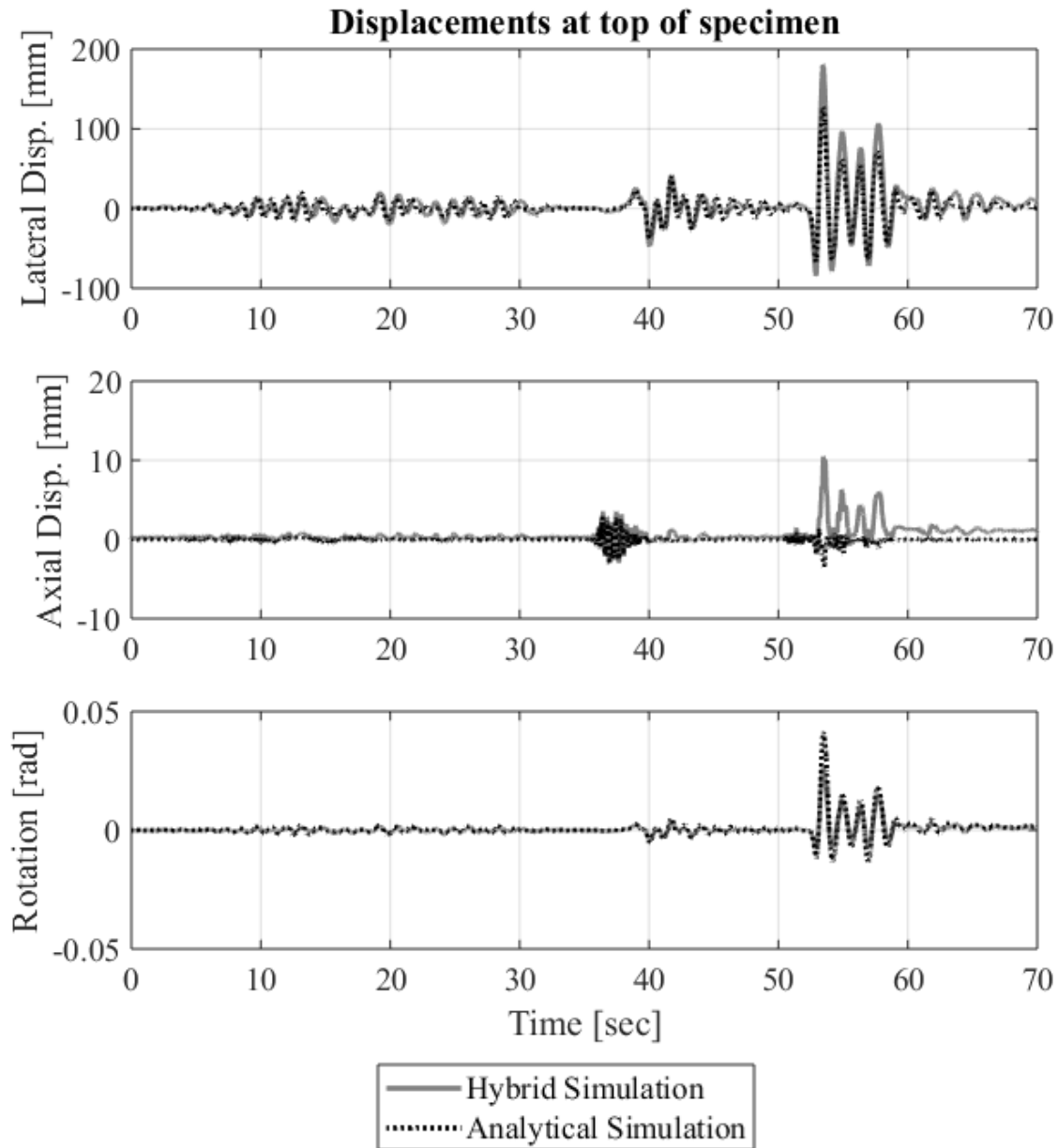
Figure 4 - 15: Displacement versus time at the top of the experimental specimen for ground motion series scaled by 0.5.

During the first large pulse of GM3, the weld at the base of the experimental specimen fractured. The discrepancy between displacements in HS and analytical simulations grew and permanent deformations were observed in both the lateral and axial displacement histories. The analytical simulation was again found to exceed HS in the rotational degree of freedom.

The force history at the control point (shown in Figure 4 - 16) also showed a greater deviation from the response of the analytical simulation with an elastic element compared to the smaller ground motion. This can be attributed to yielding, the eventual fracture of the weld, and an increased interaction between the different degrees of freedom at larger displacements.
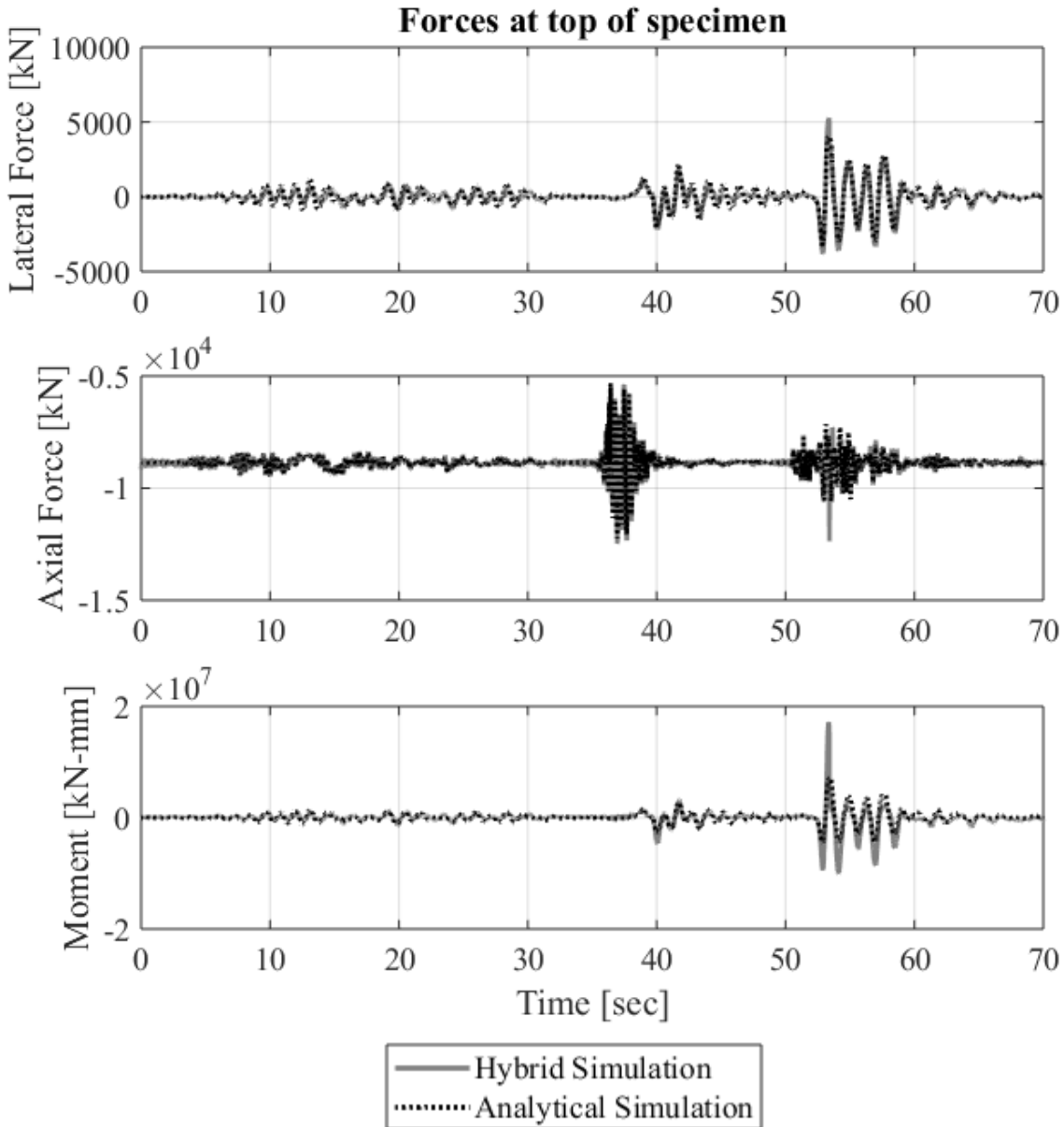
57

Figure 4 - 16: Force vs time at the top of the experimental specimen for ground motion series scaled by 0.5.

While there is more agreement in the force vs time data here compared to the displacement data, large displacement at GM3 led to large deviations in the rotational degree of freedom. At the point of fracture (approximately 53 seconds), a spike can also be seen in the vertical displacement.

Force versus displacement response of at the top of the experimental element is shown in Figure 4 - 17. Inelastic behavior is observed in the elastic element in the large pulse of GM3 even in the analytical simulation with an elastic simulated column element. This behavior can be attributed to the large displacement at the top of the column creating additional deformation due to the P-Δ effect. In the HS, the sudden drop in strength at the large displacement shows the failure of the weld at the base of the experimental structure.
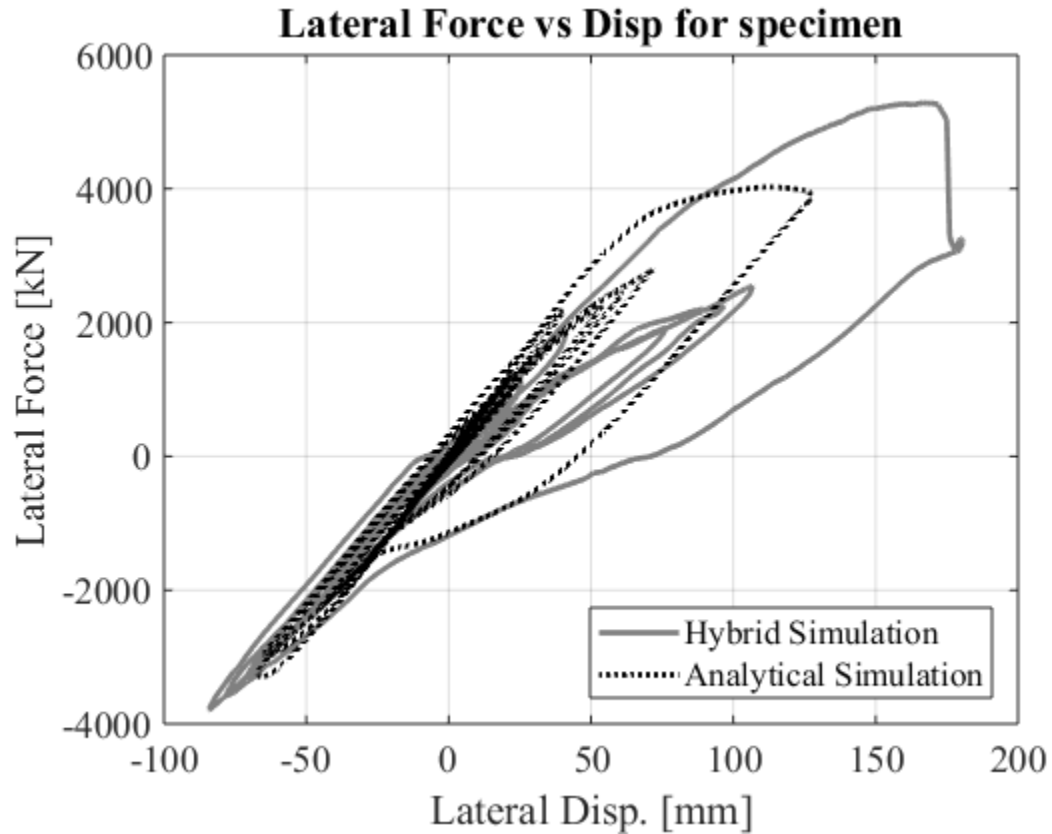
Figure 4 - 17: Force versus displacement relationships for the top of the experimental element.

During testing, a loud sound was heard coming from the test specimen at this instance and it was observed after testing that the weld at the base of the experimental substructure fractured. Images of the weld crack are shown in Figure 4 - 18. The weld fracture traverses the bolt hole near at the corners of the experimental specimen. These bolt holes are stress concentrations and likely contributed to the initiation of the cracks under the repeated HS runs.

Figure 4 - 18: Images of the experimental specimen following HS with ground motion series scaled by 0.5. Cracking occurred at the weld at the bottom right of the column in (a). Close up details of fracture shown in (b) and (c).

4.5 Conclusion

Hybrid simulation was performed on a single-column bridge where the lower portion of the column was replaced with an experimental element. A steel HSS section served as the experimental specimen with a reduced scale of 1:8.37 and the system was excited by three consecutive ground motions. The OpenFRESCO ThreeActuators experimental setup command was modified to interface with a 3D bridge model and to allow for a rigid offset from the line of action of the horizontal actuator. Following HS, the following conclusions can be drawn:

1. Gravity load application was successfully separated from the HS procedure and was applied to the experimental substructure via manual preload and applying loading in the model such that the control point during HS was held as a fixed reference frame.

2. Excitation of higher axial modes due to axial stiffness of the column were compensated by the addition of 20% Rayleigh damping at 7Hz. This damping model was found to have the lowest impact on lower frequency modes. The Generalized-α integration scheme was selected to maximize numerical damping during HS.

3. A stiffness determination procedure was performed prior to HS so that the initial stiffness guess could match that of the experimental specimen. This measured stiffness was also used to compare the response of HS with an analytical simulation in which the experimental specimen was replaced with an elastic element with matching stiffness properties.

4. HS results showed good agreement for smaller ground motions, though under large lateral displacements in GM3, interactions between the DOFs influenced the results, especially in the vertical direction.

5. During testing, there were several sources of errors identified in the test setup, with some measures taken to reduce errors during testing, such as the introduction of additional damping at higher modes, and some were left to be implemented in Chapter 5, such as backlash in the horizontal actuator.

6. The experimental substructure fractured at the weld following the HS run with the groundmotion series scaled by 0.5. Fatigue loading from repeated HS simulations and stress concentrations due to bolt holes at the weld corners were likely responsible for the early fracture.

5 Hybrid Simulation of Corrosion-Damaged Bridges

5.1 Introduction

Due to the aging stock of infrastructure in the United States and its widespread susceptibility to corrosion damage, it is of interest to understand the seismic performance of corrosion-damaged reinforced concrete bridge structures, particularly in the case where corrosion damage is localized in the plastic hinge region. In order to overcome challenges associated with pure analytical modeling and system level testing, hybrid simulation is utilized as a method to capture the intricacies of simulating earthquake performance of corrosion-damaged bridge structures. In this chapter, the HS test setup developed in Chapter 4 is implemented with an experimental substructure consisting of corroded and noncorroded RC and R/HyFRC columns with cross section and reinforcing ratios similar to those presented in Chapter 3. Corrosion damage is accelerated by applied current in a reduced scale section of a bridge column that is used as an experimental substructure in the hybrid simulation of a single-column CA highway bridge.

5.2 Materials and Specimens

5.2.1 Bridge Model

The research presented in this chapter utilizes the same bridge model presented in Chapter 4, with the only adjustment being the use of a displacement-based beam column element for the upper portion of the column. This type of element was found to yield more stable results than a force-based beam column element under the larger ground motions (GM2 and GM3). For information about the model and prototype bridge, please refer to section 4.2.1.

5.2.2 Experimental Specimen

Four column specimens were created for the experiment, one set of two reinforced HyFRC columns (referred to herein as HyFRC) and one set of two conventional RC columns (referred to herein as C). In each set of two, one column underwent accelerated corrosion (denoted with -c), while one column served as an uncorroded control (denoted with -u). Both the HyFRC and conventional concrete control mix designs were adapted from mix designs presented by Blunt and Ostertag (2009), but with only one scale of steel macro fiber (30mm) and one scale of PVA microfiber (8mm). Mix designs for both materials are shown in shown in Figure 5 - 1. Chloride was added to the batched water upon mixing at a concentration of 2% by weight binder to initiate corrosion and to improve effectiveness of accelerated corrosion via applied current.

Table 5 - 1: Mix proportions for HyFRC and C materials [per 1 m^3].

	HyFRC	C
Cement [kg]	423	423
Coarse aggregate [kg]	775	810
Fine aggregate [kg]	853	858
Batched water [kg]	237	237
PVA fibers [vol. %]	0.2	-
30mm Steel fiber [vol. %]	1.3	-
Water-binder ratio	0.54	0.54
Cl$^-$ [wt.% of binder]	2.0	2.0
f'_c [MPa]	43	45

The experimental substructure is a square column with side length of 178 mm and a specimen length of 356 mm and has a longitudinal and transverse reinforcement ratio of 1.6% and 1.2%, respectively. The experimental column has a linear scale factor of 8.37 compared to the square prototype column. The cross section of the prototype bridge column and the experimental column are shown along with the elevation detail in Figure 5 - 1. All specimens used ASTM type A706 grade 60 steel for longitudinal reinforcement and 3/16" mild steel wire for transverse reinforcement. Lenton EL12S4 couplers were used to attach the specimen to the test setup. Ultra-high performance fiber reinforced concrete (UHPFRC) was utilized to create rigid end caps to provide a stiff boundary condition at the connection between the experimental substructure and the testing frame. The mix design for the end caps can be found in Appendix C-1.
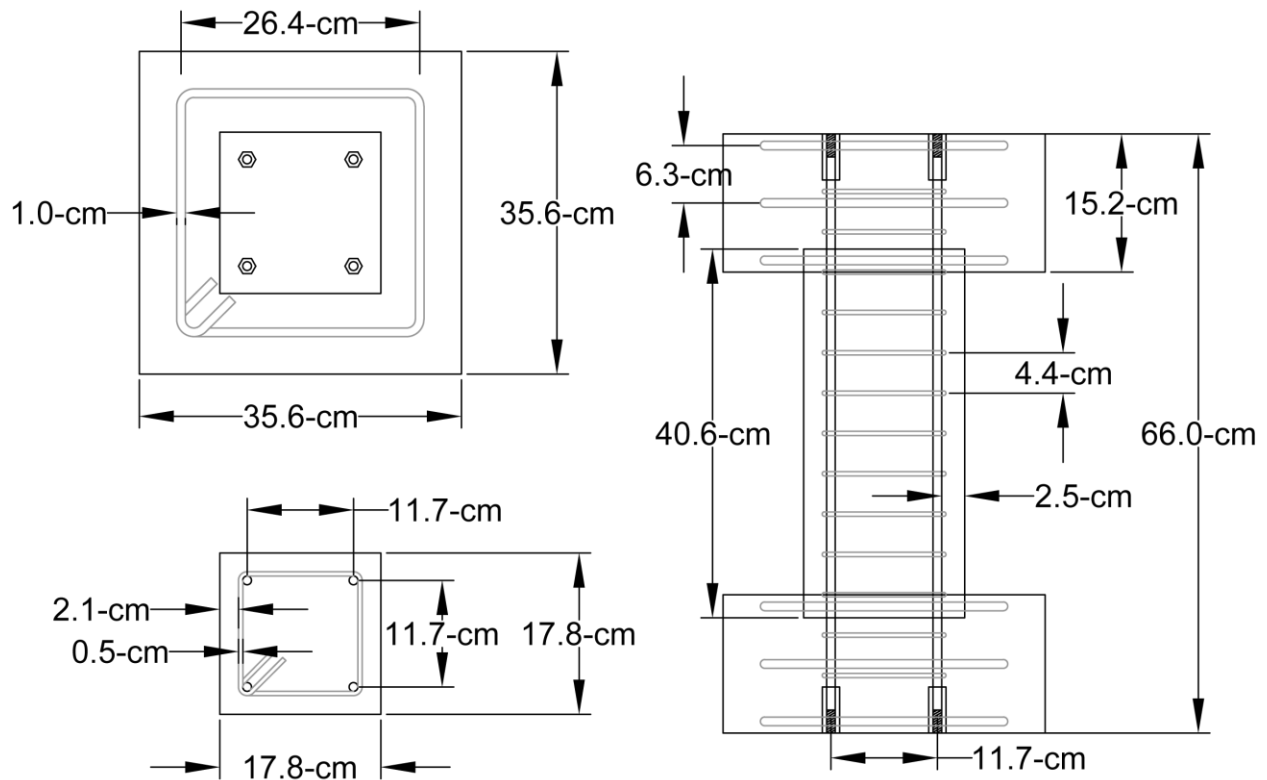
Figure 5 - 1: Cross section of model column (left), experimental column (center) and elevation detail drawing of the experimental column (right) (Drawing courtesy of Ian Williams).

5.3 Methods

5.3.1 Experimental Element Casting Sequence

Column elements (without end caps) were cast and subsequently moist cured for seven days prior to stripping formwork. Column elements were then left in ambient laboratory conditions for at least three days, at which point columns that were to undergo accelerated corrosion were placed in the dam setup described in Chapter 3, which submerged columns in 3.5% NaCl solution to allow for accelerated corrosion via applied current. Control columns were left in ambient laboratory conditions during this time. Following accelerated corrosion, all column elements were placed into new formwork for casting of UHPFRC end caps. The casting sequence of a typical column element is shown in Figure 5 - 2.
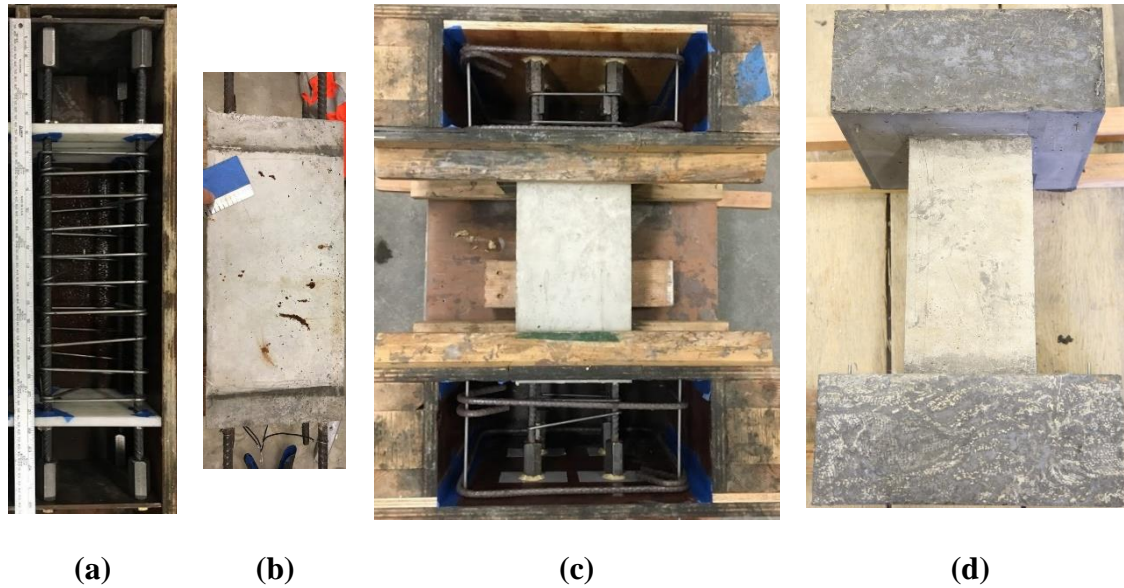
| (a) | (b) | (c) | (d) |

Figure 5 - 2: Construction progression for typical experimental specimen: (a) Column reinforcement prior to casting, (b) column element after casting, (c) column element in endcap formwork, (d) final experimental specimen.

5.3.2 Accelerated Corrosion

Chloride was added to the mix design at 2 percent by weight of binder in order to initiate corrosion of embedded reinforcement. Additionally, a Gamry G750 potentiostat was used to induce corrosion damage with a constant applied current with an intensity ranging from 0.1-0.2 mA/cm^2 over a 550-hour period. This corrosion intensity is the upper limit of corrosion rates that can be found in the most aggressive environments according to Andrade et al. (1990) and was proposed as an upper limit by El Maddaawy and Soudki (2003) when implementing accelerated corrosion via applied current. While accelerated corrosion by impressed current has been shown to alter corrosion patterns, these accelerated methods allow for specimens to be exposed to several years' worth of corrosion damage in a matter of weeks, making experimental testing feasible. The maximum applied corrosion rate is approximately 50 times the rate observed in specimens described in Chapter 3, in which corrosion rates were measured for reinforcing steel in chloride-contaminated concrete. Figure 5 - 3 shows a schematic diagram of the accelerated corrosion setup.
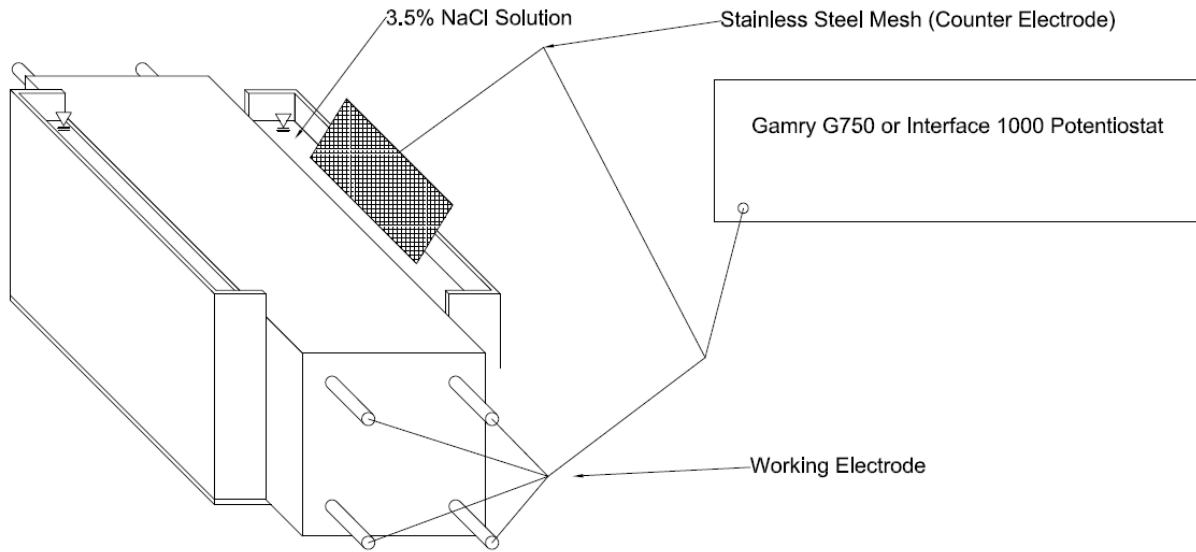
Figure 5 - 3: Schematic diagram of accelerated corrosion setup.

5.3.3 Hybrid Simulation Test Setup

The experiments presented herein use the same test setup described in Chapter 4, though improvements were made to the test setup to reduce backlash in the horizontal actuator. The improvements include the use of a custom rod end that is capable of clamping on to the rotational pin. On the clevis side, shims and set screws were used to close any gap between the pin and the clevis. A drawing of the test setup and improvements to the horizontal actuator are shown in Figure 5 - 4. The hybrid simulation procedure follows the same communication channel diagrammed in Figure 4 - 6.
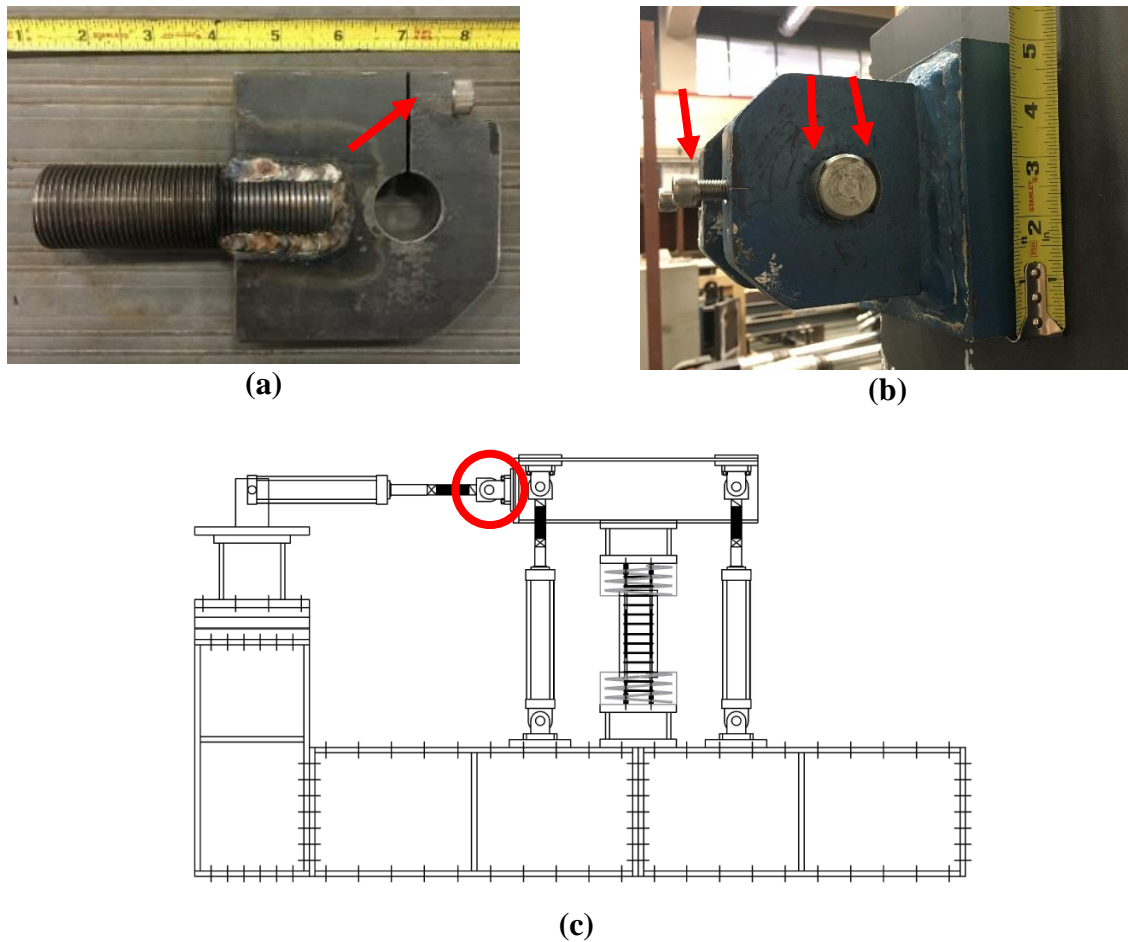
Figure 5 - 4: Detail image of updated rod end (a) and updated clevis (b) to reduce backlash in lateral degree of freedom for the test frame (c).

5.4 Results and Discussion

5.4.1 Accelerated Corrosion

Prior to the casting of the UHPFRC endcaps, one column from each set was submersed in 3.5% NaCl solution and connected to a potentiostat (in this case used as a galvanostat) for accelerated corrosion. An applied current was used to accelerate corrosion damage with an intensity of 0.1 mA/cm^2 for 90 hours, followed by 460 hours at 0.2 mA/cm^2 to create a theoretical mass loss of 103 mg/cm^2 according to Faraday's Law. This value of mass loss was targeted to match the average value observed amongst 'top' rebars in the experiment presented in Chapter 3 (average mass loss was 101 mg/cm^2). It should be noted, however, that due to electrical connection to the mild steel hoops, the mass loss is not restricted to the longitudinal reinforcement. Plots of the applied current and the measured potential over time are shown in Figure 5 - 5.
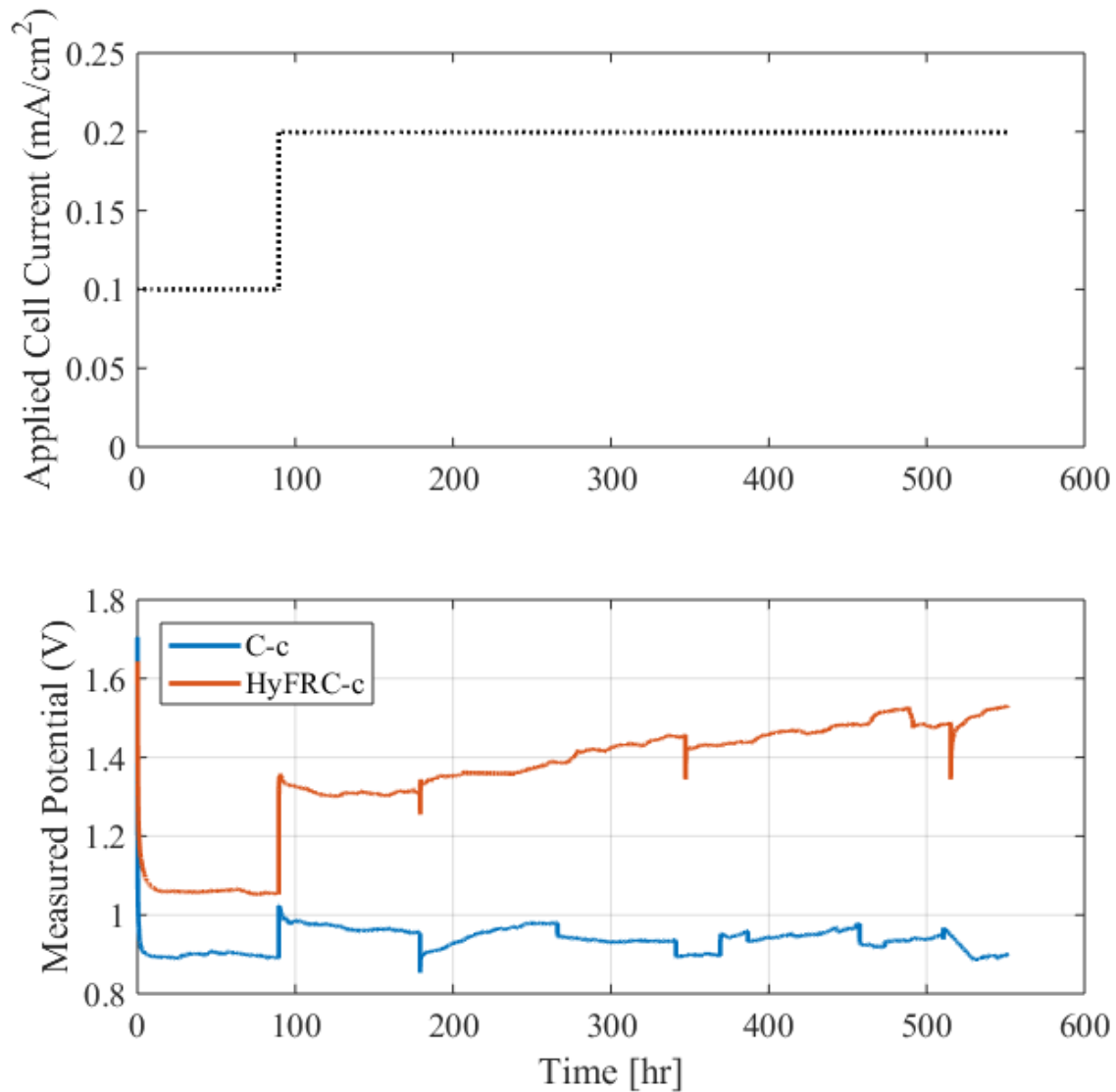
Figure 5 - 5: Applied current vs time (a) and the measured potential vs time (b) for HyFRC-c and C-c columns.

The applied potential required to induce the desired current was consistently higher for the HyFRC specimen than the C specimen, and following the initial drop in potential, the potential increased throughout accelerated corrosion exposure. Sharp changes in the measured potential occur when the test was paused for extended periods to refill the dam if the water level dropped too low. The increase in potential observed in HyFRC-c can be attributed to an increasing resistance as corrosion damage propagates and corrosion products encounter a crack resistant matrix. On the other hand, in C-c after initial cracking occurs, corrosion products were observed to migrate out to the surface. Continued corrosion damage in C-c led to widening cracks, which explains the slight decrease in measured potential during the exposure. Images of sample surface cracking for each column type at the end of the corrosion test are shown in Figure 5 - 6.
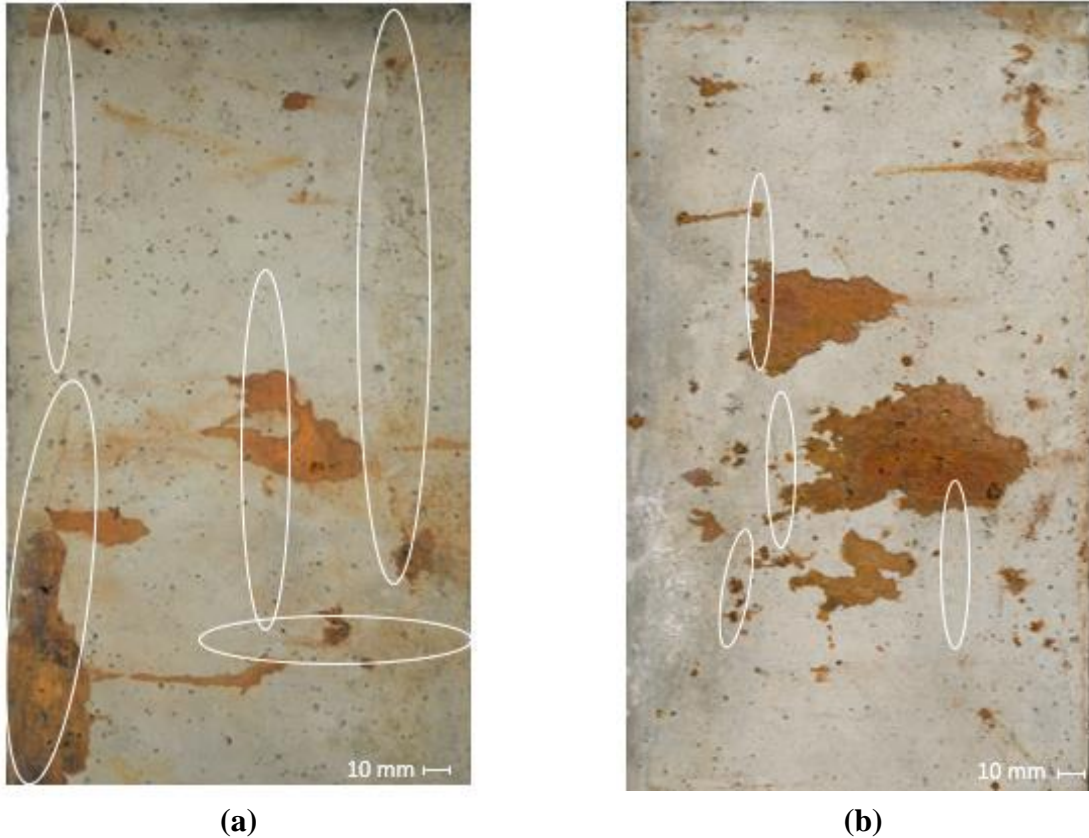
(a) **(b)**

Figure 5 - 6: Surface cracking and corrosion egress following accelerated corrosion for C-c (a) and HyFRC-c (b) at the end of the accelerated corrosion test.

Accelerated corrosion led to the development of splitting cracks in C-c, and created shorter, discontinuous cracks HyFRC-c. In both cases, corrosion products were found egressing from crack surfaces. The maximum crack width in the C-c specimen was 0.4 mm, while the maximum in HyFRC-c was 0.2 mm. Both crack widths were approximately half of the maximum value observed under long-term corrosion in chloride contaminated concrete for a similar amount of theoretical mass loss and similar material types (presented in Chapter 3). The theoretical mass loss for each reinforcing bar was predicted by Faraday's law of electrolysis (Eq. 3 - 1) and was found to be 103 mg/cm^2, which is similar to the mass lost by the average 'top' rebar presented in Chapter 3 (Average was 101.3 mg/cm^2). Once corrosion products have migrated to the surface, they no longer contribute to internal expansion of the cover concrete and thus reduce the contribution of corrosion to crack growth and damage to the cover. In Chapter 3, negligible amounts of corrosion products reached the surface of the concrete, in contrast to what was observed here.

5.4.2 Determination of Column Stiffness

Prior to HS, stiffness coefficients were determined for each specimen. The imposed displacements used in HS in Chapter 4 were reduced for the RC and R/HyFRC columns to ensure elastic behavior. The results for the stiffness determination for each specimen are compared in Table 5 - 2 (Individual plots are shown in Appendix C-2).

Table 5 - 2: Stiffness coefficients for columns prior to HS.

	C-u	C-c	HyFRC-u	HyFRC-c
Axial stiffness (K_{11}) [kN/mm]	154.9	157.3	151.6	151.4
Lateral stiffness (K_{22}) [kN/mm]	9.86	9.39	9.93	10.66
Rotational stiffness (K_{33}) [kN-mm/rad]	4.21e6	4.27e6	3.87e6	3.99e6

5.4.3 Hybrid Simulation of C Columns

Each experimental specimen was exposed to the same series of three ground motions shown in Section 4.2.5. Figure 5 - 7 shows the plot of lateral force versus displacement of the control point for the C-u specimen and compares this plot with (1) a nonlinear analytical simulation, in which the full column is modeled as a displacement-based beam column with section properties of the prototype column and (2) an elastic analytical simulation, in which the experimental specimen is modeled as an elastic element with stiffness properties matching the C-u experimental specimen in the test frame. Due to the flexibility of the loading frame that was observed in Chapter 4, the results of HS are expected to match closely with elastic analytical simulation, which has an identical initial stiffness to the experimental specimen. The nonlinear analytical simulation is plotted to demonstrate the expected stiffness of the system based on modeled properties. The flexibility of the test setup greatly influences the results of HS.
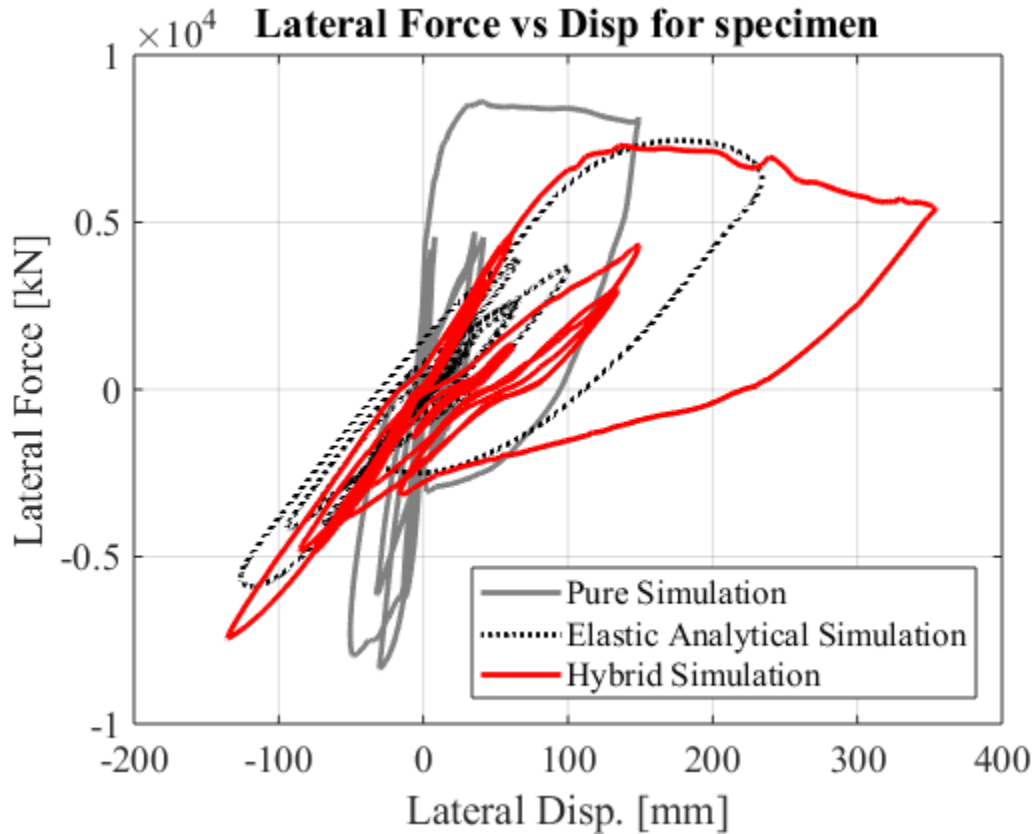
Figure 5 - 7: Force versus displacement for HS, pure simulation with prototype model properties, and analytical simulation with a simulated elastic experimental substructure.

The stiffness of the prototype column in the pure simulation is much higher than what was achieved by the experimental specimen in the test frame during HS, leading to increased strength and decreased peak displacement when compared to HS. The analytical simulation with an elastic experimental substructure, on the other hand, matches the forces even in the major pulse quite well, though the peak displacement is considerably less than HS. The backlash has also been reduced compared to Figure 4 - 14, and though it does not plateau, there is still a change in slope around the origin, indicating that the backlash has not been completely eliminated. Figure 5 - 8, Figure 5 - 9, and Figure 5 - 10 show displacement history, force history, and force versus displacement plots, respectively, at the control point for HS of the C-c and C-u columns.
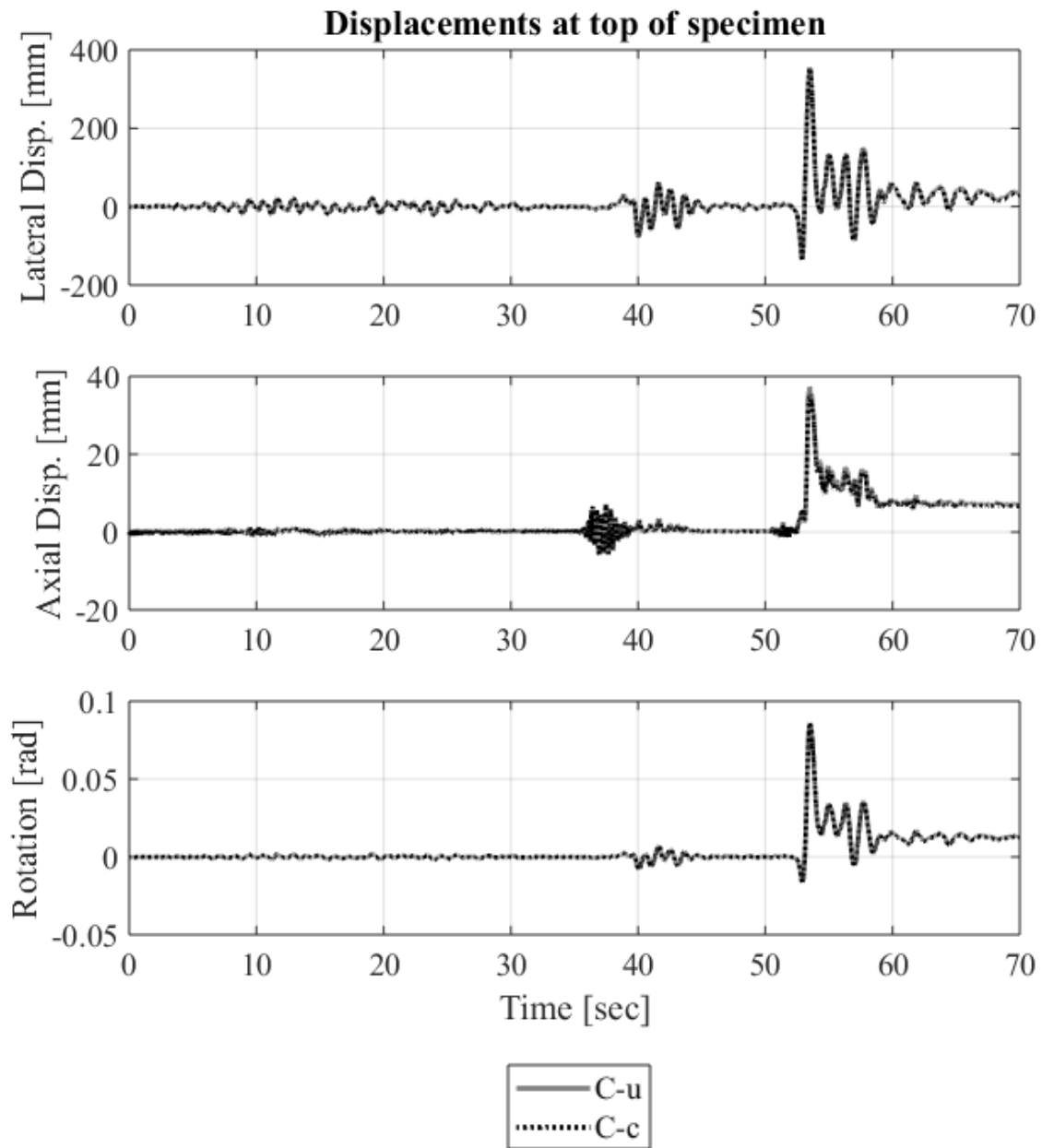
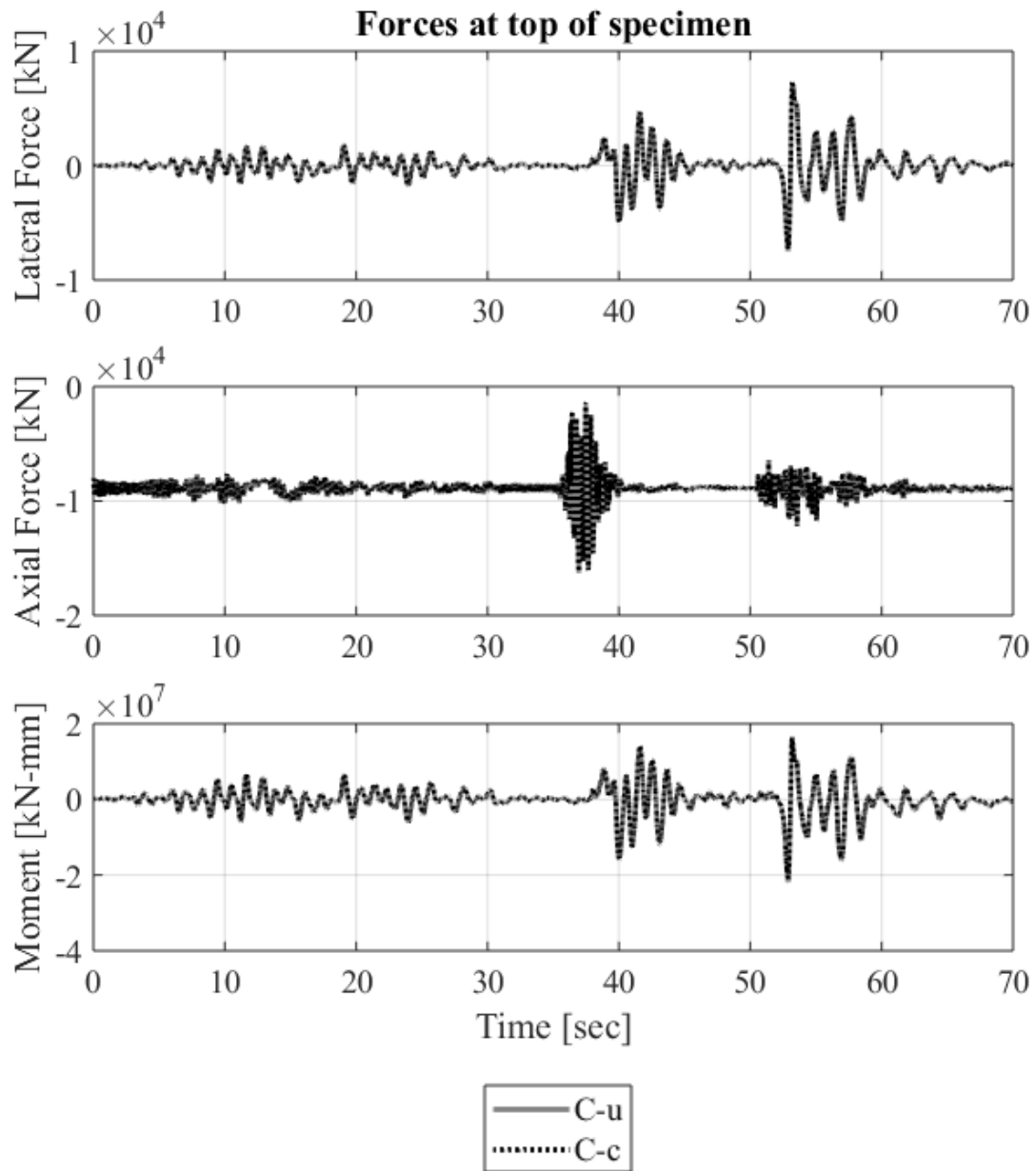**Figure 5 - 8**: HS displacement history at control point for C specimens.

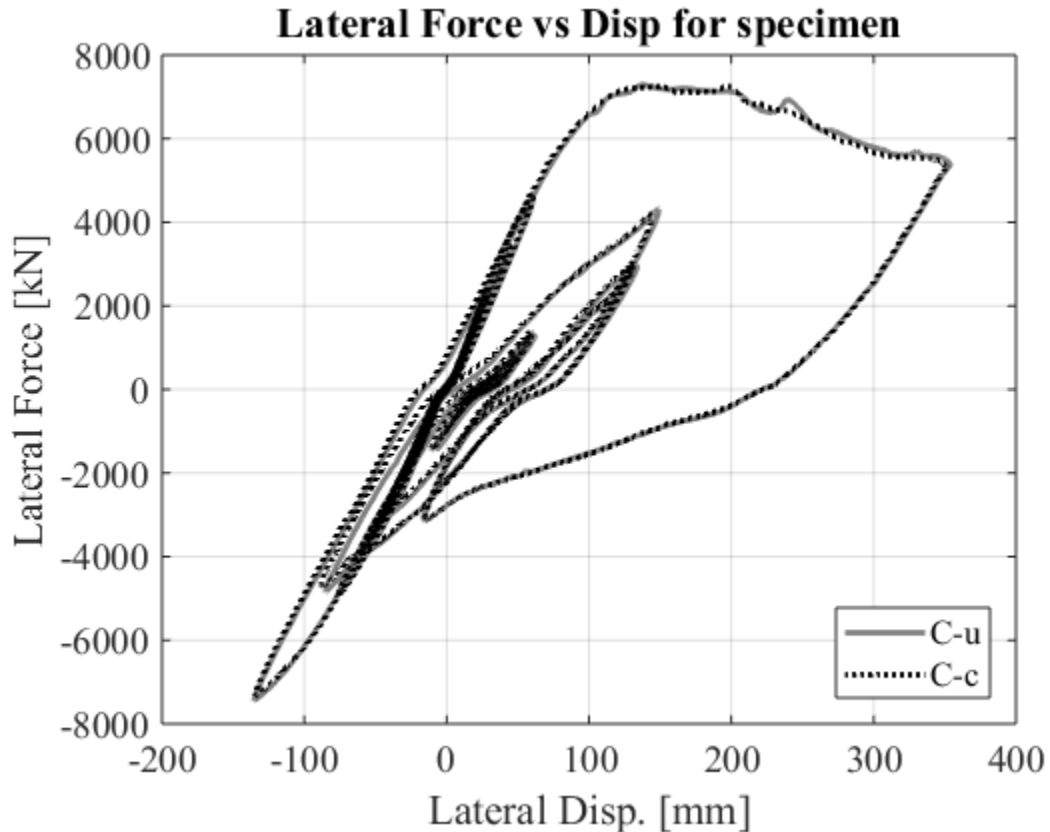**Figure 5 - 9**: HS force history at control point for C specimens.

Figure 5 - 10: Force versus displacement at control point for C specimens.

The results of HS show that the corrosion damage induced in this experiment did not have a distinguishable effect on the seismic performance of the columns. While it is possible that the level of corrosion damage was insufficient to create a large difference in performance, it is more likely that the method of attachment of the experimental specimen to the test frame was insufficient and dominated behavior while the column remained elastic. Some slight differences are observed in the inelastic behavior of the major pulse, but the ultimate displacement and softening curve seem to demonstrate that behavior of specimen is not dominated by the specimen itself, but rather governed by the flexibility of the test setup. The columns did observe permanent deformations following the large displacements of GM3 as seen in Figure 5 - 8. Both columns experienced spalling in the plastic hinge region of the column. The cover material was delaminated and was removed by hand following HS. Images of the damaged columns are shown in Figure 5 - 11.
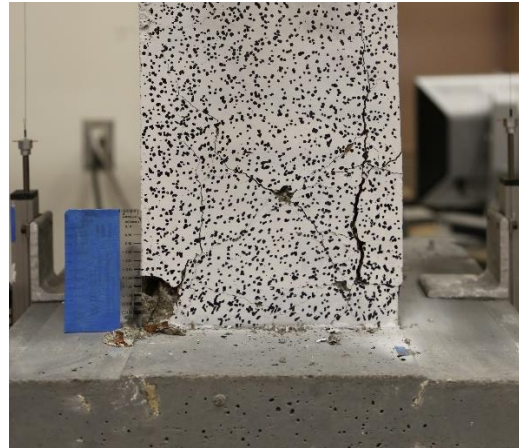
Figure 5 - 11: Damage to C columns following HS: C-u (a), C-c (b), C-c with cover removed (c).

Corrosion products in C column confirm that the hoops contributed to corrosion damage and that corrosion damage was not isolated to longitudinal reinforcement. This likely contributed to the tendency to spall in the C-c specimen. Corrosion products can be seen in the regions between transverse reinforcement, indicating that cracking formed and partially delaminated the cover prior to damage from HS. This corrosion damage was not sufficient to cause spalling on its own, as the egress of corrosion products from surface cracks reduced the pressure that products placed on the cover.

5.4.4 Hybrid Simulation of HyFRC Columns

Figure 5 - 12, Figure 5 - 13, and Figure 5 - 14 show displacement history, force history, and force versus displacement plots, respectively, for the HyFRC columns. During the HS run for the HyFRC-u specimen, the interlock was engaged, effectively stopping the simulation during the

large pulse of GM3. Since the stiffness of the two HyFRC columns were very similar and the behavior during GM1 and GM2 was very similar it was not deemed necessary to test a new specimen.
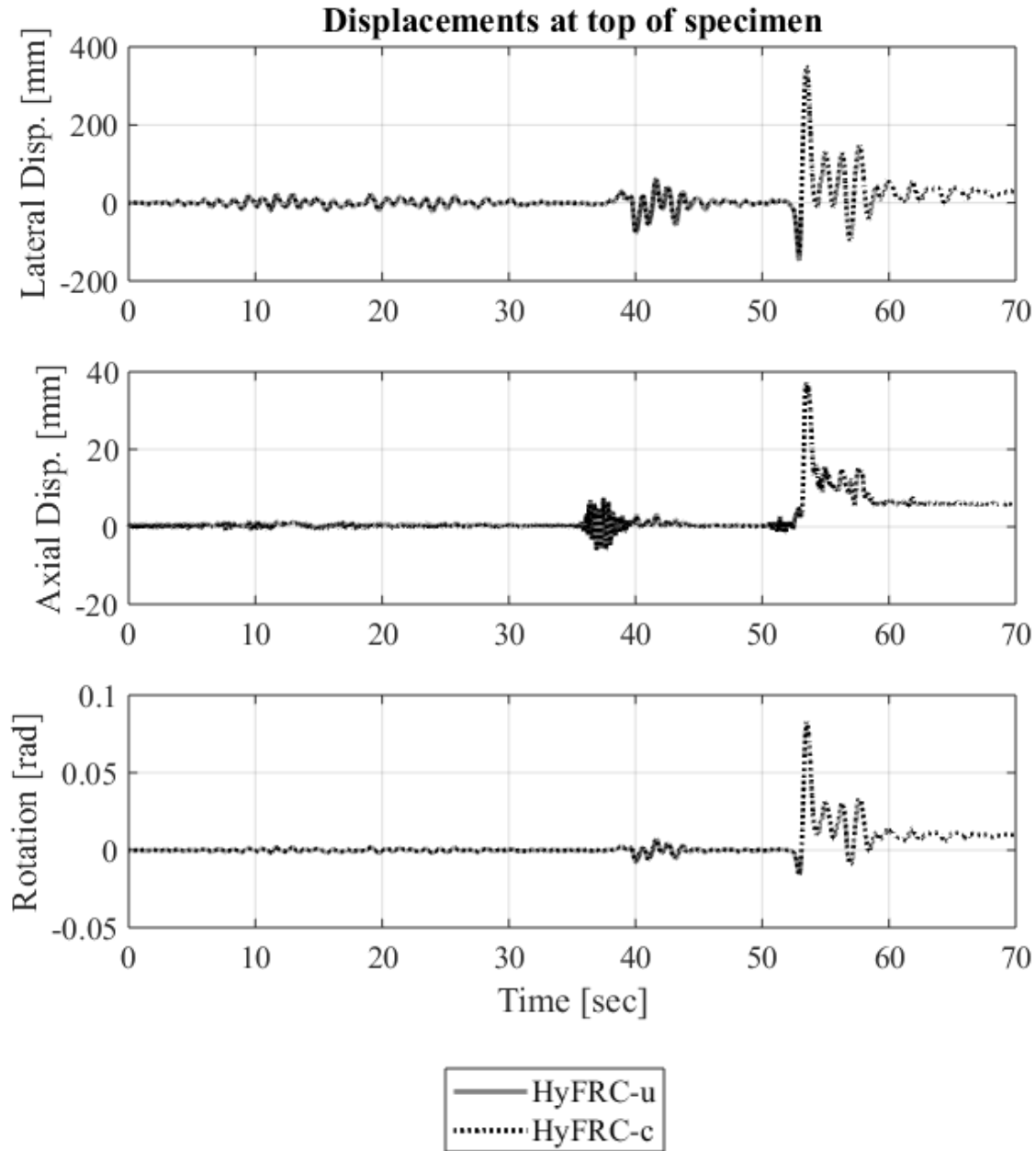

Figure 5 - 12: HS displacement history at control point for HyFRC specimens.
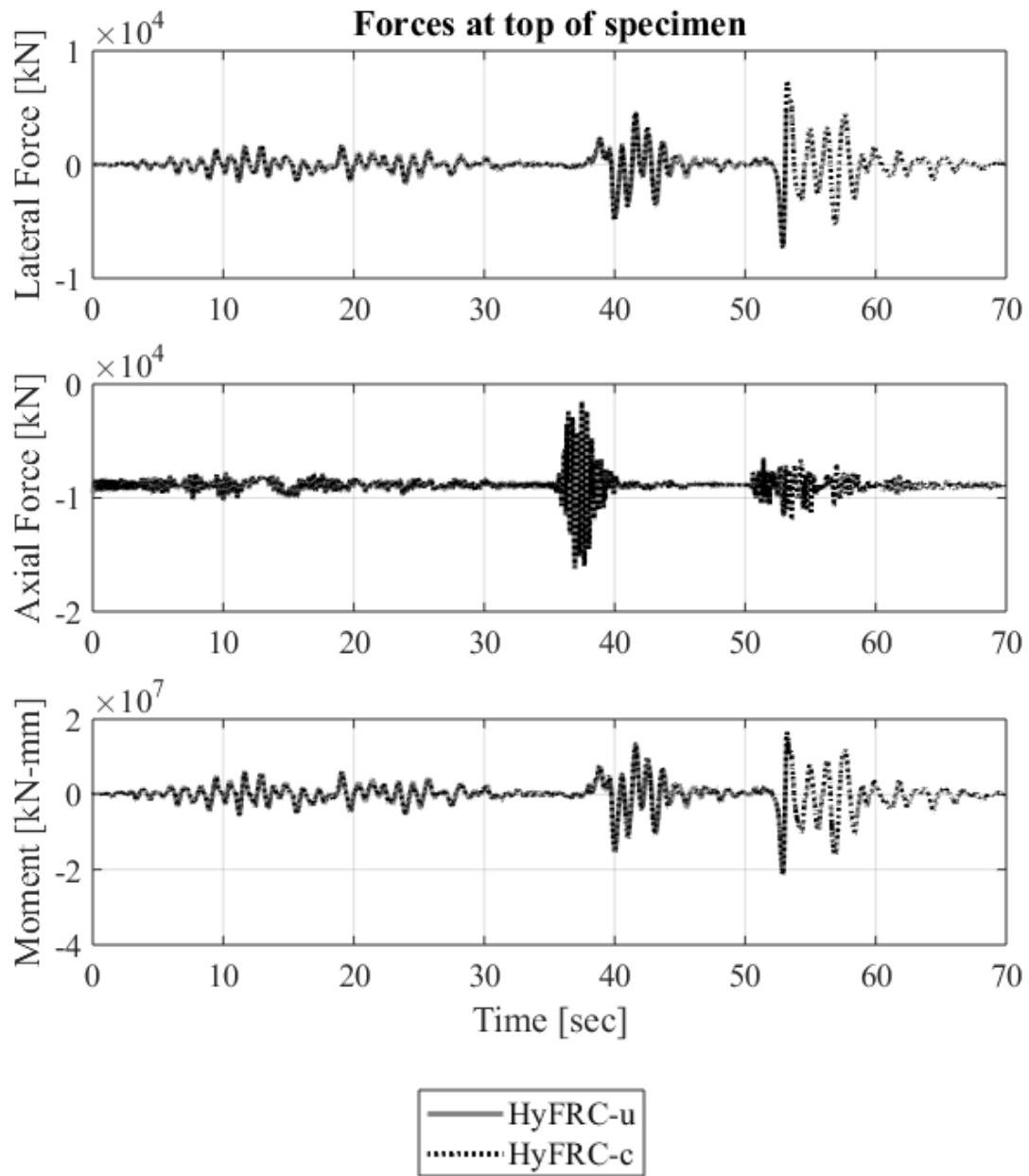
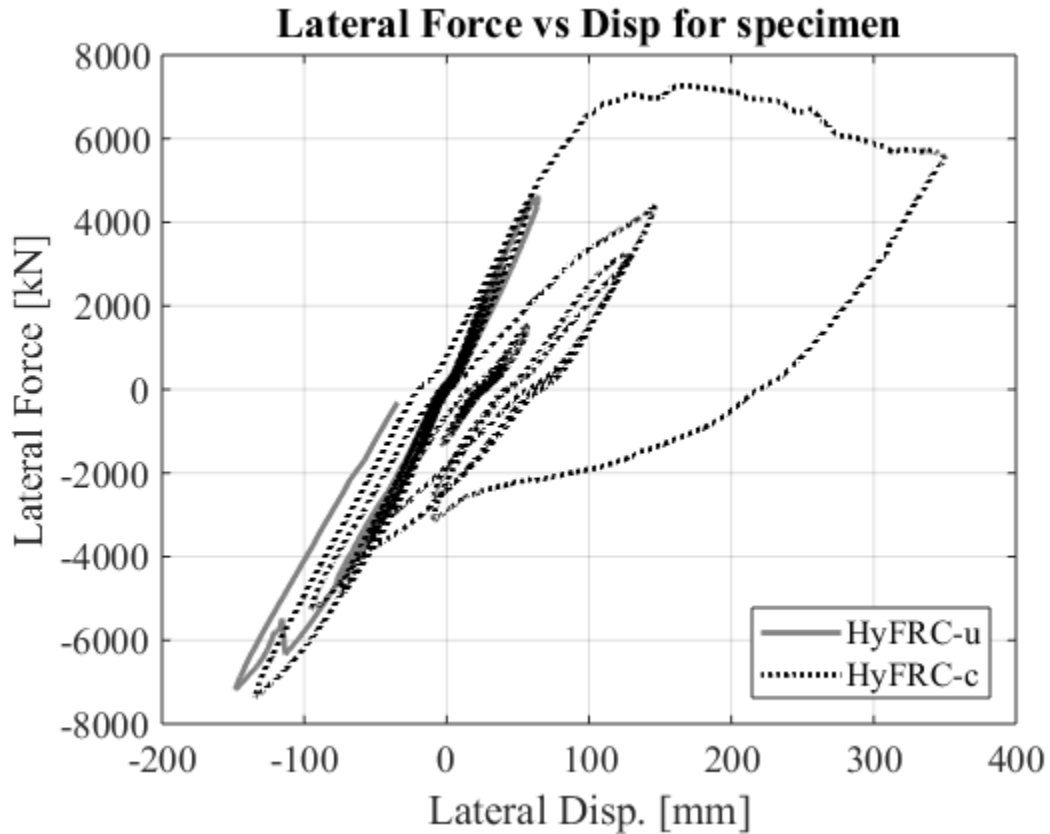**Figure 5 - 13**: HS force history at control point for HyFRC specimens.

Figure 5 - 14: Force versus displacement at control point for C specimens.

Cracking was observed in the HyFRC columns following HS with some amount of crushing occurring in HyFRC-c. The cover could not be easily removed following HS and thus the reinforcement was not exposed. Damage was also observed in the UHPFRC end cap, due to the increased tensile flexural strength of the HyFRC column. Figure 5 - 15 shows cracking in column and damage to the end cap following HS.
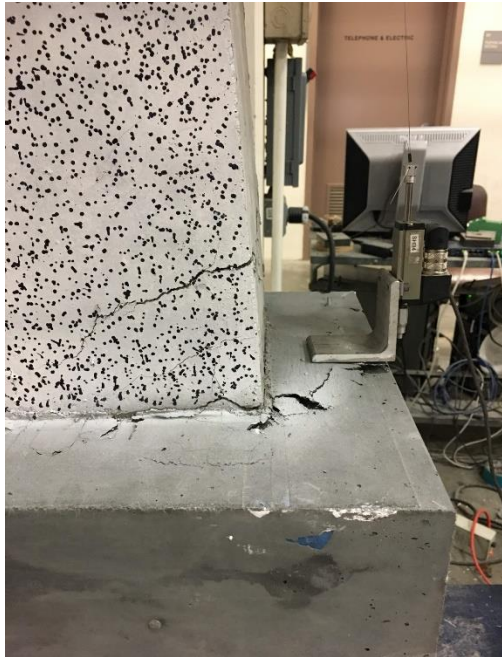
(a) **(b)**

Figure 5 - 15: Damage to HyFRC columns following HS: HyFRC-u (a) and HyFRC-c (b).

The HyFRC specimens did not show any distinct change in performance in this HS application, and rather matched the results of the C columns, while the damage patterns were very different amongst the columns. Figure 5 - 16 shows force versus displacement plots for C-u, C-c and HyFRC-c together to show the degree of overlap in the different hybrid simulations.
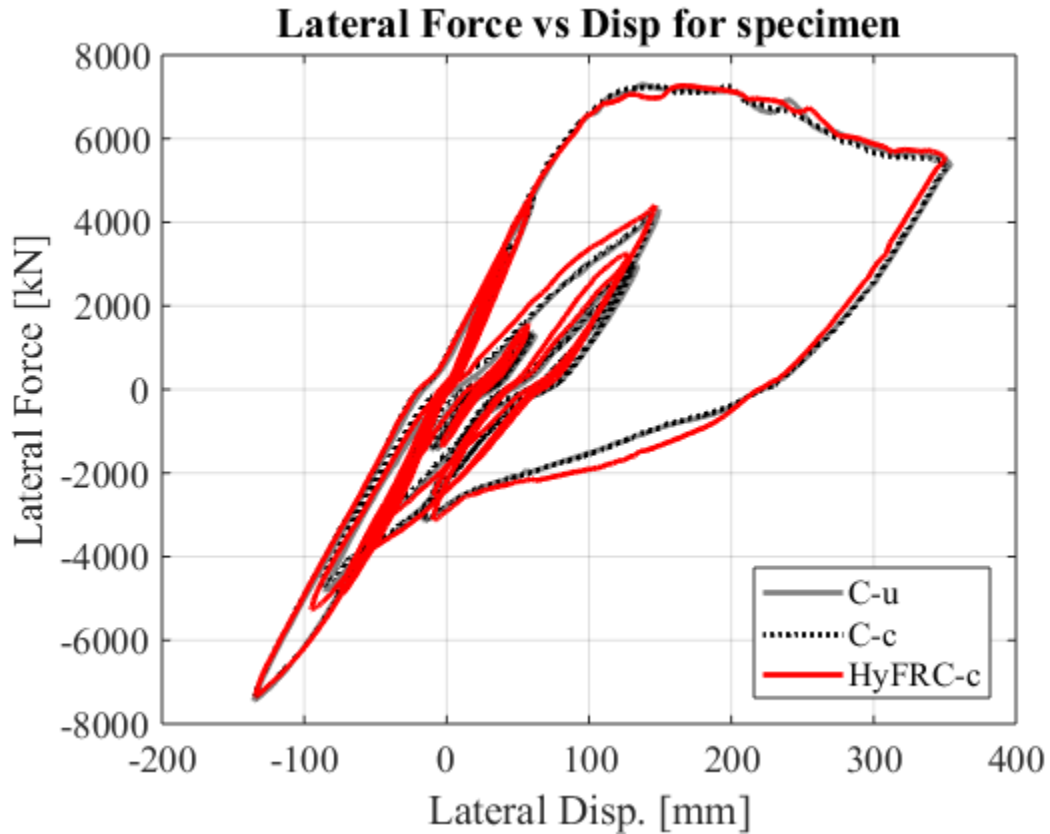
Figure 5 - 16: HS force versus displacement at control point for C-u, C-c and HyFRC-c specimens.

5.4.5 Stiffness reduction following HS

Following HS, a second stiffness determination was conducted to measure any loss in stiffness following exposure to seismic damage. The results are shown in Table 5 - 3, along with the percent reduction for each stiffness value, comparing each value with the respective stiffness value prior to HS.

Table 5 - 3: Residual stiffness values following HS.

	C-u	C-c	HyFRC-u*	HyFRC-c
Axial stiffness (K_{11}) [kN/mm]	125.1	124.7	133.5	130.6
% Reduction	19.2	20.7	11.9	13.8
Lateral stiffness (K_{22}) [kN/mm]	5.60	5.27	8.60	8.58
% Reduction	43.2	43.8	13.4	19.5
Rotational stiffness (K_{33}) [kN-mm/rad]	2.25e6	2.11e6	3.14e6	2.46e6
% Reduction	46.5	50.7	18.8	38.4

*HyFRC-u did not complete the full ground motion series

All specimens (corroded or uncorroded) were observed to lose stiffness in all DOFs after being exposed to seismic loading, with corroded control specimens revealing almost the same stiffness reduction as the uncorroded control samples. Corroded HyFRC columns were more effective at retaining stiffness for all DOFs compared to the corroded control specimens. Since the cover in HyFRC specimens did not spall off, it was still able to contribute to the stiffness of the column following HS.

5.5 Conclusion

Hybrid Simulation was utilized to investigate the effect of corrosion damage in the plastic hinge on seismic behavior of reinforced concrete bridge columns. Reduced scale R/HyFRC and conventional RC columns served as the experimental substructure and were exposed to corrosion damage via applied current. The following conclusions can be drawn.

1. Accelerated corrosion led to the egress of corrosion products from cracks, leading to smaller crack widths for a given theoretical mass loss when compared to long-term chloride-induced corrosion. HyFRC was effective at reducing crack widths and led to a higher measured potential to reach the desired cell current.

2. Backlash in the horizontal actuator was reduced through the use of a modified rod end that clamps down onto the pin and a clevis that utilizes shims to close any gap and set screws to ensure a tight fit for the pin.

3. HyFRC columns were more effective at preventing spalling as well as retaining their stiffness following severe seismic damage, even with pre-existing corrosion damage.

4. The degree of corrosion and corresponding amount of damage was not sufficient to observe any appreciable change in performance of the columns. This is likely due to the flexibility of the test setup and the method used to attach the experimental specimen to the test frame.

The latter could be improved through the use prestressing rods to fasten the experimental specimen to the test frame more securely. This modification would also remove the need to connect longitudinal reinforcement to the test setup via couplers, so headed reinforcement could anchor the rebar in the UHPFRC end cap. A schematic drawing of the proposed updated specimen is shown in Figure 5 - 17.
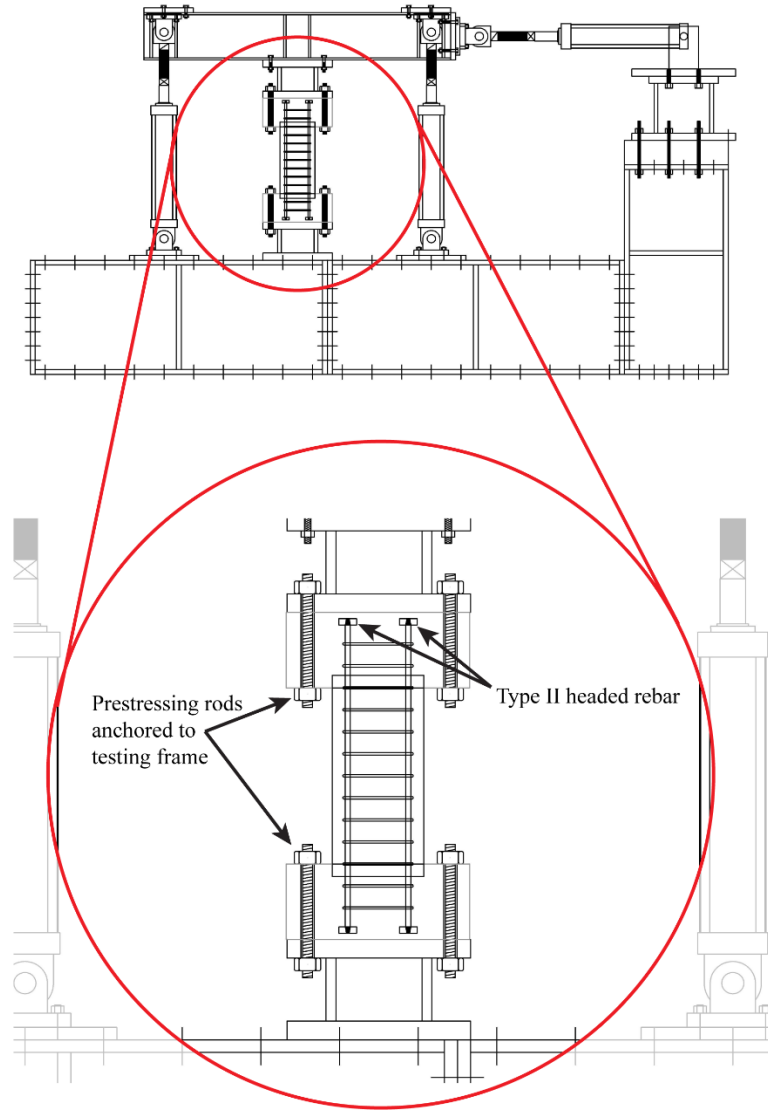

Figure 5 - 17: Updated test specimen would allow for a more rigid connection between the test frame and the experimental specimen (Drawing courtesy of Ian Williams).

6 Conclusion

The influence of corrosion damage on mechanical properties in reinforced concrete and HyFRC columns was investigated experimentally to better understand the seismic performance of damaged structures and the influence of fiber reinforcement on durability during corrosion propagation and ductility during extreme loading. A long-term corrosion propagation experiment was performed to investigate the compressive behavior of reinforced SCC and SC-HyFRC column elements and the tensile behavior of corroded rebar. A hybrid simulation procedure was developed to test the seismic performance of a single-column bridge in which the column-base was a physical experimental specimen that interfaced with a computer model of the remainder of the structure during earthquake ground motion. This HS procedure was implemented with corrosion damaged reinforced concrete and HyFRC column elements with and without corrosion damage. Corrosion damage in these elements was accelerated via applied current.

Admixed chlorides were used to bypass the corrosion initiation phase so that experimental work could focus on the propagation of corrosion damage. However, the lower compressive strength of the SC-HyFRC suggests a higher porosity at the matrix/rebar interface which has been shown to dictate the corrosion propagation phase (Hay and Ostertag 2019). This was also supported by corrosion patterns seen on reinforcement as the lower side of the bar during casting was more prone to corrosion damage due to higher porosity from bleed water. Despite higher mass loss of the rebars and hence more corrosion product formation in SC-HyFRC the corrosion products were more densely packed at the rebar surface due to the crack growth resistance of the SC-HyFRC matrix. Hence, the variation in compressive strength limited the comparisons that could be made between SC-HyFRC and SCC regarding corrosion behavior. Whereas it has been clearly proven that HyFRC and SC-HyFRC is able to extend the corrosion initiation phase, long-term corrosion propagation studies in reinforced HyFRC materials requires further investigation before definitive conclusions can be drawn about the effectiveness of HyFRC to slow down the corrosion propagation phase.

Fiber reinforcement reduced the extent of cracking under long-term chloride-contamination, with corrosion products found to be more densely packed at the bar surface. Additionally, crack widths were found to be smaller and more likely to remain discontinuous, rather than connect to form large splitting cracks. These results were also observed under accelerated corrosion due to applied current in reinforced concrete and HyFRC columns, in which the non-fiber-reinforced column observed wider crack widths and more corrosion product egress than its HyFRC counterpart. Additionally, the measured potential to corrode the HyFRC column at a given current was higher than in the control. Under both long-term chloride contamination and applied current, spalling was not observed. In the columns discussed in Chapter 3, stainless steel transverse reinforcing bars were found to bridge cracks during corrosion propagation and likely prevented spalling from occurring. Accelerated corrosion experiments supported this theory, as corrosion products were found to deposit in cracks between hoops. Due to the large amount of egress of corrosion products, this method was also unable to produce spalling prior to mechanical loading. The impact of crack control and spalling on corrosion propagation behavior should be further investigated to better understand the electrochemical impacts of cracking and spalling resistance of fiber reinforcement.

Corrosion damage was not found to influence axial stiffness or compressive strength of RC or R/HyFRC column elements, as the strength gain of the concrete materials throughout the experiment had a more meaningful impact on overall strength in the columns. In HS, experiments,

column stiffness was measured for all three degrees of freedom. While there was a slight difference in measured stiffness for corroded versus noncorroded columns, this would need to be tested in a stiffer test frame for the influence of corrosion on stiffness to be more clearly discerned. Corrosion of reinforcing steel reduced both its strength and ductility, with ductility experiencing a larger reduction.

Hybrid simulation has the potential to improve our understanding of the seismic performance of reinforced concrete bridges with corrosion damaged components, though great care must be given to the creation of a stiff test frame. Flexibility in the testing frame in the research presented led to a large reduction in the measured stiffness of the experimental specimen when compared to its theoretical stiffness. This caused the propagation of error that reduced the sensitivity of the HS to differences between experimental specimens. This loss in resolution prevented the ability to distinguish between experimental specimens with and without corrosion damage and/or fiber reinforcement. Backlash in the horizontal actuator contributed to this error during stiffness measurement and was reduced through the introduction of a prestressing rod end that clamps onto the pin and a modified clevis with shims and set screws to remove the small gap between the pin and the clevis. This fix was effective at removing the zero-slope plateau when the actuator switch from tension to compression, though there still was a change in slope as the force changed signs. Figure 6 - 1 compares the HS curve with the pure analytical simulation of the nonlinear bridge model and zooms in on the origin to compare the initial stiffness of the HS system with that of the pure analytical model.
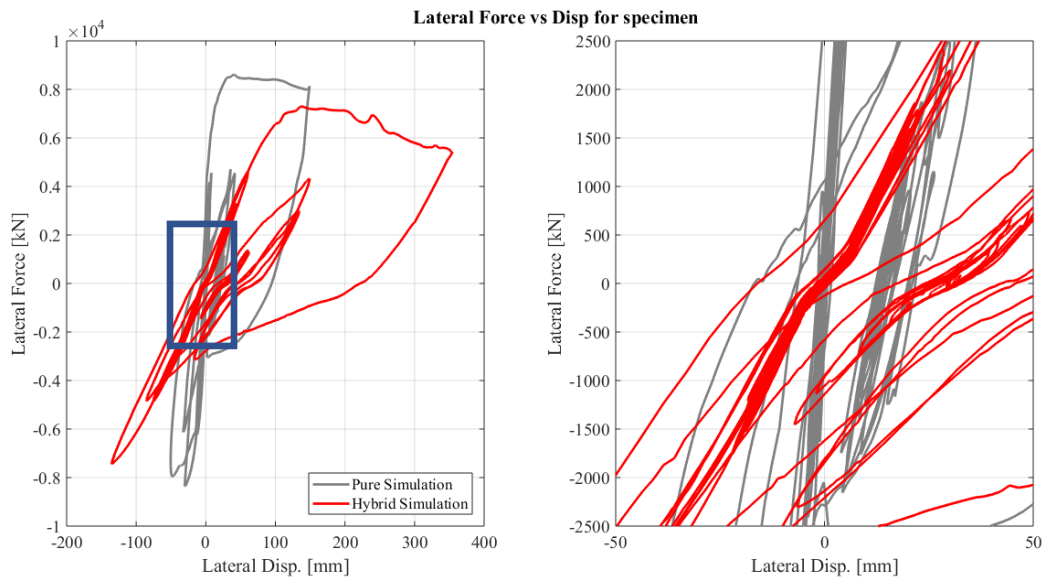

Figure 6 - 1: Lateral force versus displacement for HS and nonlinear analytical simulation.

In addition to the remaining backlash in the system, which occurs around the origin, the large difference in stiffness between HS and the pure simulation led to a more extreme lateral response of the structure. The stiffness coefficients of the experimental specimen in the test frame were shown to only be a small portion of the expected values in Chapter 4. Since the flexibility of the loading frame governed the stiffness response, it follows that it should also govern the behavior of the HS, which was observed in Chapter 5, as it was impossible to distinguish between corroded vs

uncorroded or fiber-reinforced vs non fiber-reinforced. In order to improve this test setup, measures must be taken to computationally compensate for backlash in the system and flexibility of the testing frame. This additional calibration will allow for the resolution required to see changes in seismic behavior due to different damage states or due to the introduction of fiber reinforcement.

References

Almusallam, AA. 2001. "Effect of Degree of Corrosion on the Properties of Reinforcing Steel Bars." *Construction and Building Materials* 15 (8): 361–68.

ACI Committee 222R-01. 2001. "Protections of Metals in Concrete Against Corrosion." American Concrete Institute, Farmington Hills, MI. 2001.

Alonso, C, C Andrade, and JM Diez. 1998. "Factors Controlling Cracking of Concrete Affected by Reinforcement Corrosion." *Materials and Structures* 31: 435–41.

Andrade, C, and C Alonso. 1996. "Corrosion Rate Monitoring in the Laboratory and On-Site." *Construction and Building Materials* 10 (5): 315–28.

Andrade, C, C Alonso, and FJ Molina. 1993. "Cover Cracking as a Function of Bar Corrosion: Part I-Experimental Test." *Materials and Structures* 26: 453–64.

Angst, U, B Elsener, CK Larsen, and O Vennesland. 2009. "Critical Chloride Content in Reinforced Concrete - A Review." *Cement and Concrete Research* 39 (12): 1122–38.

Apostolopoulos, CA, and VG Papadakis. 2008. "Consequences of Steel Corrosion on the Ductility Properties of Reinforcement Bar." *Construction and Building Materials 22* (2008): 2316-2324.

American Society of Civil Engineers. 2017. "2013 Report card for America's infrastructure." American Society of Civil Engineers, 2017.

ASTM Standard A706. 2016. "Standard Specification for Deformed and Plain Low-Allow Steel Bars for Concrete Reinforcement." ASTM International, West Conshohocken, PA, 2016.

ASTM Standard C876. 2015. "Standard Test Method for Corrosion Potentials of Uncoated Reinforcing Steel in Concrete." ASTM International, West Conshohocken, PA, 2015.

ASTM Standard G1-03. 2017. "Standard Practice for Preparing, Cleaning and Evaluating Corrosion Test Specimens." ASTM International, West Conshohocken, PA, 2017.

Banthia, N and A Bhargava. 2007. "Permeability of Stressed Concrete and Role of Fiber Reinforcement." *ACI Materials Journal* 104 (1): 70–76.

Bažant, ZP. 1979. "Physical Model for Steel Corrosion in Concrete Sea Structures-Theory." *Journal of the Structural Division* 105.

Berrocal, CG, I Löfgren, K Lundgren, and L Tang. 2015. "Corrosion Initiation in Cracked Fibre Reinforced Concrete: Influence of Crack Width, Fibre Type and Loading Conditions." *Corrosion Science* 98: 128–39.

Blunt, J, and CP Ostertag. 2009. "Performance-Based Approach for the Design of a Deflection Hardened Hybrid Fiber-Reinforced Concrete." *Journal of Engineering Mechanics* 135 (9): 978–86.

Blunt, JD, and CP Ostertag. 2009. "Deflection Hardening and Workability of Hybrid Fiber Composites." *ACI Materials Journal* 106 (3): 265–72.

Bonelli, A, and OS Bursi. 2004. "Generalized-α Methods for Seismic Structural Testing." *Earthquake Engineering and Structural Dynamics* 33 (10): 1067–1102.

Cairns, J, GA Plizzari, Y Du, DW Law, and C Franzoni. 2005. "Mechanical Properties of Corrosion-Damaged Reinforcement." *ACI Materials Journal* 102-M29 (102): 256–64.

Caré, S, and A Raharinaivo. 2007. "Influence of Impressed Current on the Initiation of Damage in Reinforced Mortar Due to Corrosion of Embedded Steel." *Cement and Concrete Research* 37 (12): 1598–1612.

Chae, Y, J Lee, M Park, and CY Kim. 2018. "Real-Time Hybrid Simulation for an RC Bridge Pier Subjected to Both Horizontal and Vertical Ground Motions." *Earthquake Engineering and Structural Dynamics* 47 (7): 1673–79.

Chung, J, and GM Hulbert. 2019. "A Time Integration Algorithm for Structural Dynamics With Improved Numercial Dissipation: The Generalized-α Method" 6 (1993).

Chopra, AK. *Dynamics of Structures: Theory and Applications to Earthquake Engineering*. Hoboken, NJ: Pearson, 2017.

Costa, A, and J Appleton. 1999. "Chloride Penetration into Concrete in Marine Environment." *Materials and Structures* 32: 354–59.

Dermitzakis, SN, and SA Mahin. 1985. "Development of Substructuring Techniques for On-Line Computer Controlled Seismic Performance Testing." *Earthquake Engineering Research Center* 4 (UCB/EERC-85/04): 170 pp.

Du, YG, LA Clark, and AHC Chan. 2005. "Residual Capacity of Corroded Reinforcing Bars." *Magazine of Concrete Research* 57 (3): 135–47.

El Maaddawy, TA and KA Soudki. 2003. "Effectiveness of Impressed Current Technique to Simulate Corrosion of Steel Reinforcement in Concrete." *Journal of Materials in Civil Engineering* 15 (1): 41–47.

Elsener, B, M Molina, and H Böhni. 1993. "The Electrochemical Removal of Chlorides from Reinforced Concrete." *Corrosion Science* 35 (5–8): 1563–70.

Ezeldin, AS, and PN Balaguru. 1993. "Normal and high-strength Fiber-Reinforced Concrete under Compression" *ASCE Journal of Civil Engineering Materials* 4 (170): 415–29.

Fajardo, G, G Escadeillas, and G Arliguie. 2006. "Electrochemical Chloride Extraction (ECE) from Steel-Reinforced Concrete Specimens Contaminated by 'Artificial' Sea-Water." *Corrosion Science* 48 (1): 110–25.

fib. 2006. "Bulletin 34 - Model Code for Service Life Design." International Federation for Structural Concrete (*fib*). Lausanne, Switzerland. 2006.

Fang, C, K Lundgren, L Chen, and C Zhu. 2004. "Corrosion Influence on Bond in Reinforced Concrete." *Cement and Concrete Research* 34 (11): 2159–67.

Francois, R, and JC Maso. 1988. "Effect of Damage in Reinforced Concrete on Carbonation or Chloride Penetration." *Cement and Concrete Research* 18 (6): 961–70.

Glass, GK, and NR Buenfeld. 1997. "The Presentation of the Chloride Threshold Level for Corrosion of Steel in Concrete." *Corrosion Science* 39 (5): 1001–13.

Gonzalez, JA, JS Algaba, and C Andrade. 1980. "Corrosion of Reinforcing Bars in Carbonated Concrete." *British Corrosion Journal* 15 (3): 135–39.

Hay, R, and CP Ostertag. 2019. "Influence of Transverse Cracks and Interfacial Damage on Corrosion of Steel in Concrete with and without Fiber Hybridization." *Corrosion Science* 153 (June): 213–24.

Hong, K, and RD Hooton. 1999. "Effects of Cyclic Chloride Exposure on Penetration of Concrete Cover." *Cement and Concrete Research* 29 (9): 1379–86.

Ishii, K, H Seki, T Fukute, and K Ikawa. 1998. "Cathodic Protection for Prestressed Concrete Structures." *Construction and Building Materials* 12 (2–3): 125–32.

Jaffer, SJ, and CM Hansson. 2008. "The Influence of Cracks on Chloride-Induced Corrosion of Steel in Ordinary Portland Cement and High Performance Concretes Subjected to Different Loading Conditions." *Corrosion Science* 50 (12): 3343–55.

Jen, G, and CP Ostertag. 2016. "Experimental Observations of Self-Consolidated Hybrid Fiber Reinforced Concrete (SC-HyFRC) on Corrosion Damage Reduction." *Construction and Building Materials* 105 (February): 262–68.

Kaviani, Peyman. 2011. "Performance-Based Seismic Assessment of Skewed Bridges." University of California, Irvine. PhD Dissertation.

Koch GH, M Brongers, NG Thompson, YP Virmani, and JH Payer. 2001. "Corrosion costs and preventive strategies in the United States. " Report FHWA-RD-01-156. Office of Infrastructure Research and Development. McLean, VA. 773 pp.

Koch GH, J Varney, N Thompson , O Moghissi, M Gould, and J Payer. 2016. "International Measures of Prevention, Application, and Economics of Corrosion Technologies Study. " National Association of Corrosion Engineers (NACE). Houston, TX. 216 pp.

Lee, C, JF Bonacci, MDA Thomas, M Maalej, S Khajehpour, N Hearn, S Pantazopoulou, and S Sheikh. 2000. "Accelerated Corrosion and Repair of Reinforced Concrete Columns Using Carbon Fibre Reinforced Polymer Sheets." *Canadian Journal of Structural Engineering* 27: 941–48.

Liu, Y and RE Weyers. 1998. "Modeling the Time to Corrosion Cracking in Chloride Contaminated Reinforced Concrete Structures." *ACI Materials Journal* 95 (6): 675–80.

Mahin, Stephen A, and Pui-shum B Shing. 1985. "Pseudodynamic Method for Seismic Testing." *ASCE Journal of Structural Engineering* I (7): 1482–1503.

Mander, J.B., M.J.N. Priestley, and R. Park. 1988. "Theoretical Stress-Strain Model for Confined Concrete." *ASCE Journal of Structural Engineering* 114 (8): 1804–26.

Markeset, G, and M Kioumarsi. 2017. "Need for Further Development in Service Life Modelling of Concrete Structures in Chloride Environment." *Procedia Engineering* 171: 549–56.

McKenna, F, GL Fenves, MH Scott. 2000. Open System for Earthquake Engineering Simulation (OpenSEES).

Meda, A, S Mostosi, Z Rinaldi, and P Riva. 2015. "Corroded RC Columns Repair and Strengthening with High Performance Fiber Reinforced Concrete Jacket." *Materials and Structures* 49 (5): 1967–78.

Mehta, PK, and PJM Monteiro. *Concrete: Microstructure, Properties, and Materials*. New York: McGrawHill, 2014.

Mercan, O, and J Ricles. 2007. "Stability and Accuracy Analysis of Outer Loop Dynamics in Real-Time Pseudodynamic Testing of SDOF Systems." *Earthquake Engineering & Structural Dynamics* 36: 1523–43.

Mercan, O, and J Ricles. 2008. "Stability Analysis for Real-Time Pseudodynamic and Hybrid Pseudodynamic testing with multiple sources of delay." *Earthquake Engineering & Structural Dynamics* 36: 1523–43.

Maalej, M and VC Li. 1994. "Flexural/Tensile-Strength Ratio in Engineered Cementitious Composites." *Journal of Materials in Civil Engineering,* 6 (4): 513–28.

Molina, FJ, C Alonso, and C Andrade. 1993. "Cover Cracking as a Function of Rebar Corrosion: Part 2-Numerical Model." *Materials and Structures* 26 (9): 532–48.

Mosalam, KM, and S Günay. 2013. "Hybrid Simulations: Theory, Applications, and Future Directions." *Advanced Materials Research* 639–640 (1): 67–95.

Naaman, AE, and HW Reinhardt. 2006. "Proposed Classification of HPFRC Composites Based on Their Tensile Response." *Materials and Structures/Materiaux et Constructions* 39 (289): 547–55.
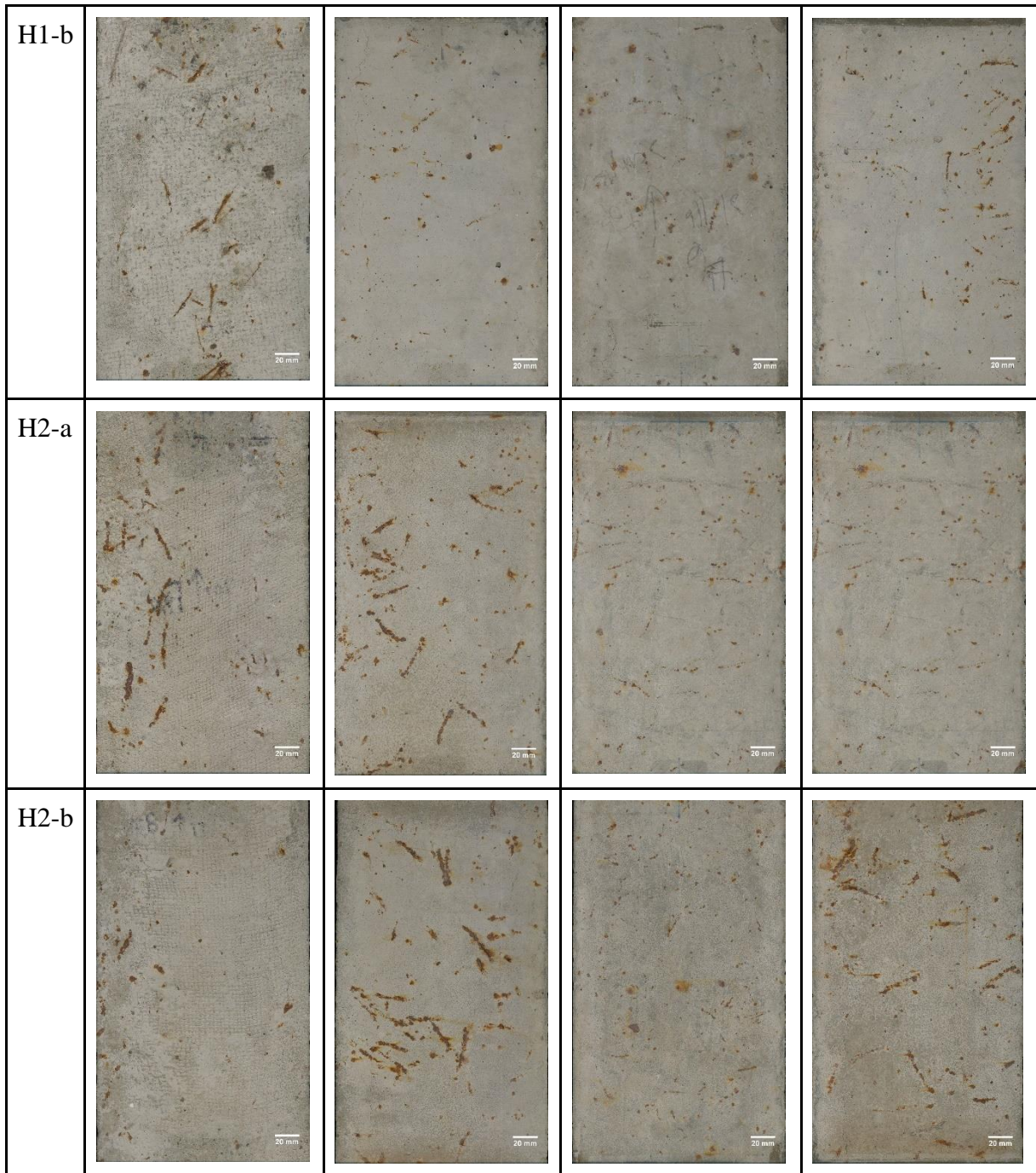
Nagayama, M, and M Cohen. 1963. "The Anodic Oxidation of Iron in a Neutral Solution." *Journal of The Electrochemical Society* 110 (6): 670.

Nataraja, M.C., N. Dhang, and A.P. Gupta. 1999. "Stress–Strain Curves for Steel-Fiber Reinforced Concrete under Compression." *Cement and Concrete Composites* 21 (5–6): 383–90.

National Bridge Inventory. 2018. FHWA. McLean, VA. Web. Accessed 6/15/19.

Nguyen, W, JF Duncan, TM Devine, and CP Ostertag. 2018. "Electrochemical Polarization and Impedance of Reinforced Concrete and Hybrid Fiber-Reinforced Concrete under Cracked Matrix Conditions." *Electrochimica Acta* 271: 319–36.

Nguyen, W, JF Duncan, G Jen, and CP Ostertag. 2018. "Influence of Matrix Cracking and Hybrid Fiber Reinforcement on the Corrosion Initiation and Propagation Behaviors of Reinforced Concrete." *Corrosion Science* 140: 168–81.

Nygaard, PV, and MR Geiker. 2005. "A Method for Measuring the Chloride Threshold Level Required to Initiate Reinforcement Corrosion in Concrete." *Materials and Structures/Materiaux et Constructions* 38 (278): 489–94.

Okada, T, and Seki, M 1977. "A simulation of earthquake response of reinforced concrete buildings." Proc, 6th World Conf. on Earthquake Engrg., New Dehli, India, Vol. 9, 25-30.

Okada, K, K Kobayashi, and T Miyagawa. 1988. "Influence of Longitudinal Cracking Due to Reinforcement Corrosion on Characteristics of Reinforced Concrete Members." *ACI Structural Journal* (85): 134–40.

Panagiotou, M, W Trono, G Jen, P Kumar, and CP Ostertag. 2015. "Experimental Seismic Response of Hybrid Fiber-Reinforced Concrete Bridge Columns with Novel Longitudinal Reinforcement Detailing." *Journal of Bridge Engineering* 20 (7). https://doi.org/10.1061/(ASCE)BE.1943-5592.0000684.

Pantazopoulou, SJ, JF Bonacci, S Sheikh, MDA Thomas, and N Hearn. 2001. "Repair of Corrosion Damaged Columns with FRP Wraps." *Journal of Composites for Construction* 5(1): 3–11.

Pourbaix, M. *Atlas of electrochemical equilibria in aqueous solutions*. National Association of Corrosion Engineers, Houston, TX. 1974.

Poursaee, A, and CM Hansson. 2009. "Potential Pitfalls in Assessing Chloride-Induced Corrosion of Steel in Concrete." *Cement and Concrete Research* 39 (5): 391–400.

Puzzanghera, J. Dec. 2, 2018. "Rebuilding crumbling infrastructure has bipartisan support. But who gets to pay for it? " Los Angeles Times. Web. Accessed 6/15/19.

Rapoport, J, CM Aldea, SP Shah, B Ankenman, and AF Karr. 2001. "Permeability of Cracked Steel Fiber-Reinforced Concrete." *ASCE Journal of Materials in Civil Engineering* 14 (115): 355–58.

Rodriguez, J, LM Ortega, and J Casal. 1997. "Load Carrying Capacity of Concrete Structures with Corroded Reinforcement." *Construction and Building Materials* 11 (4): 239–48.

Şahmaran, M, and IÖ Yaman. 2008. "Influence of Transverse Crack Width on Reinforcement Corrosion Initiation and Propagation in Mortar Beams." *Canadian Journal of Civil Engineering* 35 (3): 236–45.

Šavija, B, M Luković, J Pacheco, and E Schlangen. 2013. "Cracking of the Concrete Cover Due to Reinforcement Corrosion: A Two-Dimensional Lattice Model Study." *Construction and Building Materials* 44: 626–38.

Schellenberg, A, HK Kim, Y Takahashi, GL Fenves and SA Mahin. 2009. Open Framework for Experimental Setup and Control (OpenFRESCO).

Shao, X, AM Reinhorn, and MV Sivaselvan. 2011. "Real-Time Hybrid Simulation Using Shake Tables and Dynamic Actuators." *Journal of Structural Engineering* 137 (7): 748–60.

Stern, M, and AL Geary. 1957. "Electrochemical Polarization." *Journal of The Electrochemical Society* 104 (9): 559.

Stojadinovic, B, G Mosqueda, and SA Mahin. 2006. "Event-Driven Control System for Geographically Distributed Hybrid Simulation." *Journal of Structural Engineering* 132 (1): 68–77.

Takanashi, K., Udagawa, K., Seki, M., Okada, T., and Tanaka, H., "Non- linear Earthquake Response Analysis of Structures by a Computer-Actuator On-Line System," Bulletin of Earthquake Resistant Structure Research Center, No. 8, Institute of Industrial Science, University of Tokyo, Tokyo, Japan, 1975.

Takanashi, K, K Udagawa, and H Tanaka, (1978). "Earthquake response analysis of steel frames by computer-actuator on-line system." Proc, 5th Japan Earthquake Engrg. Symp., 1321-1328.

Tapan, M, and RS Aboutaha. 2011. "Effect of Steel Corrosion and Loss of Concrete Cover on Strength of Deteriorated RC Columns." *Construction and Building Materials* 25 (5): 2596–2603.

Terzic, V, and B Stojadinovic. 2014. "Hybrid Simulation of Bridge Response to Three-Dimensional Earthquake Excitation Followed by Truck Load." *Journal of Structural Engineering (United States)* 140 (8): 1–11.

Thewalt, CR, and SA Mahin. 1987. "Hybrid Solution Techniques for Generalized Pseudodynamic Testing." *Earthquake Engineering Research Center* 9 (UCB/EERC-87/09): 133 pp.

Turgay, T, Z Polat, HO Koksal, B Doran, and C Karakoç. 2010. "Compressive Behavior of Large-Scale Square Reinforced Concrete Columns Confined with Carbon Fiber Reinforced Polymer Jackets." *Materials and Design* 31 (1): 357–64.

Tuutti, K. 1982. Corrosion of steek in concrete. Swedish Cement and Concrete Research Institute. Stockholm.

van der Wegen, G, K Van Breugel, and RB Polder. 2012. "Guideline for Service Life Design of Structural Concrete with Regard to Chloride Induced Corrosion - the Approach in the Netherlands." *2nd International Symposium on Service Life Design for Infrastructure* 57 (3): 265–72.

Vorster, MC, JP Merrigan, RW Lewis, and RE Weyers. 1992. "Techniques for Concrete Removal and Bar Cleaning on Bridge Rehabilitation Projects." *National Research Council, Strategic Highway Research Program Technical Report, SHRP-S*, 336.

Wang, K, DC Jansen, SP Shah, and AF Karr. 1997. "Permeability Study of Cracked Concrete." *Cement and Concrete Research* 27 (3): 381–93.

Wilson, K, M Jawed, and V Ngala. 2013. "The Selection and Use of Cathodic Protection Systems for the Repair of Reinforced Concrete Structures." *Construction and Building Materials* 39: 19–25.

Yi, CK, and CP Ostertag. 2005. "Mechanical Approach in Mitigating Alkali-Silica Reaction." *Cement and Concrete Research* 35 (1): 67–75.

Yuan, Y, Y Ji, and SP Shah. 2007. "Comparison of Two Accelerated Corrosion Techniques for Concrete Structures." *ACI Structural Journal* 104 (3): 344–47.

Appendix A

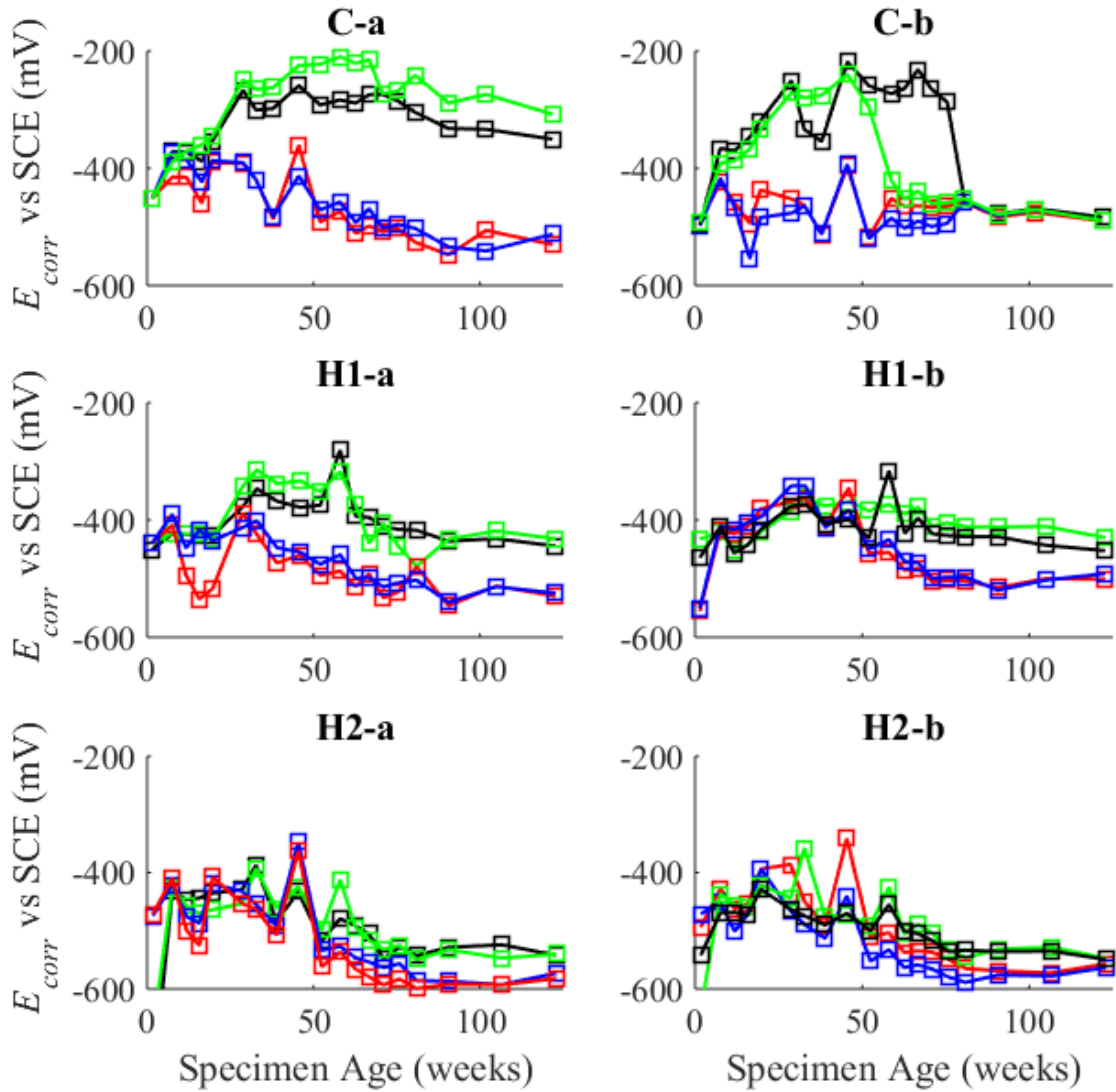**A-1: Individual Column Surfaces at Conclusion of Corrosion Exposure.**

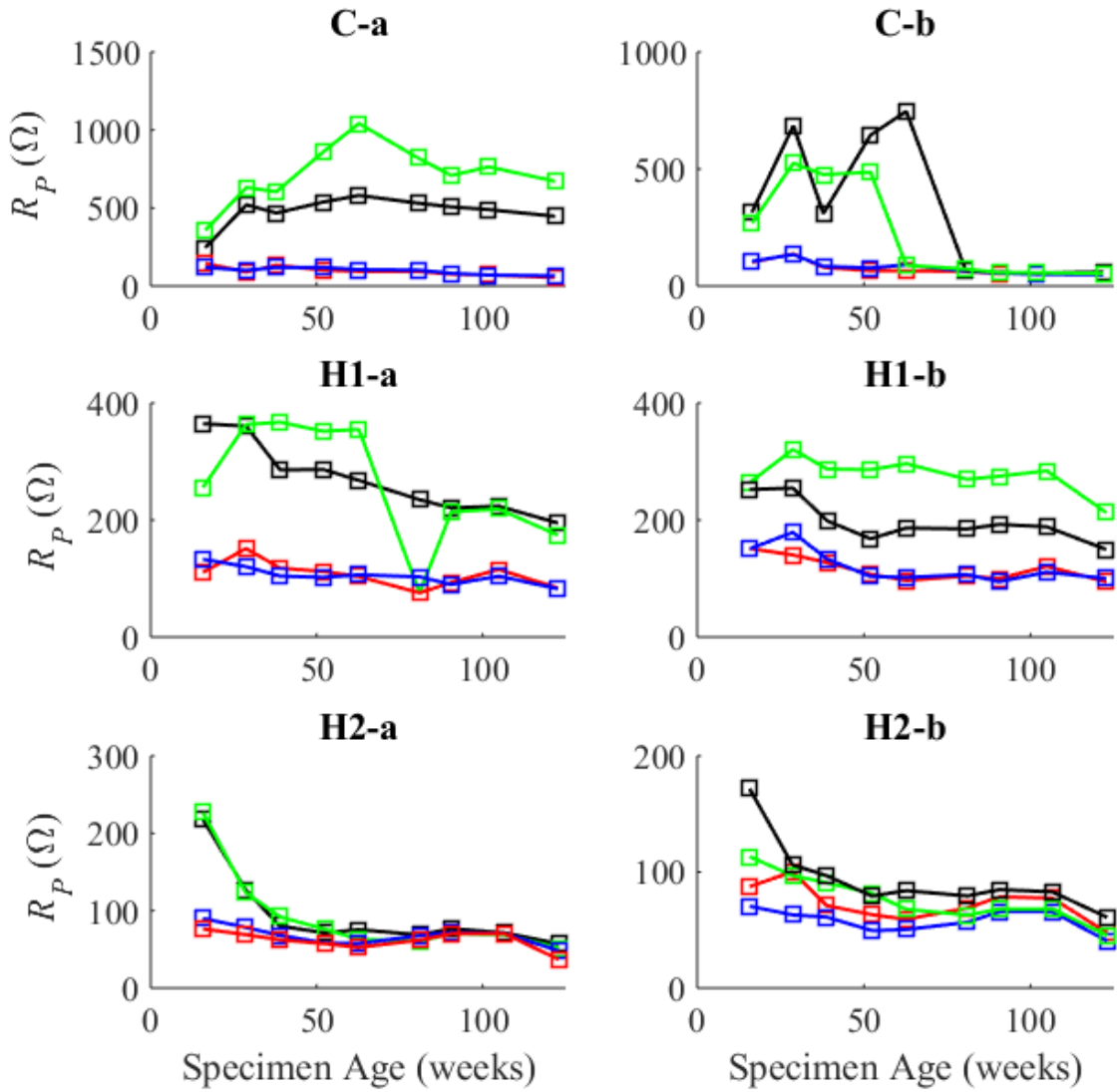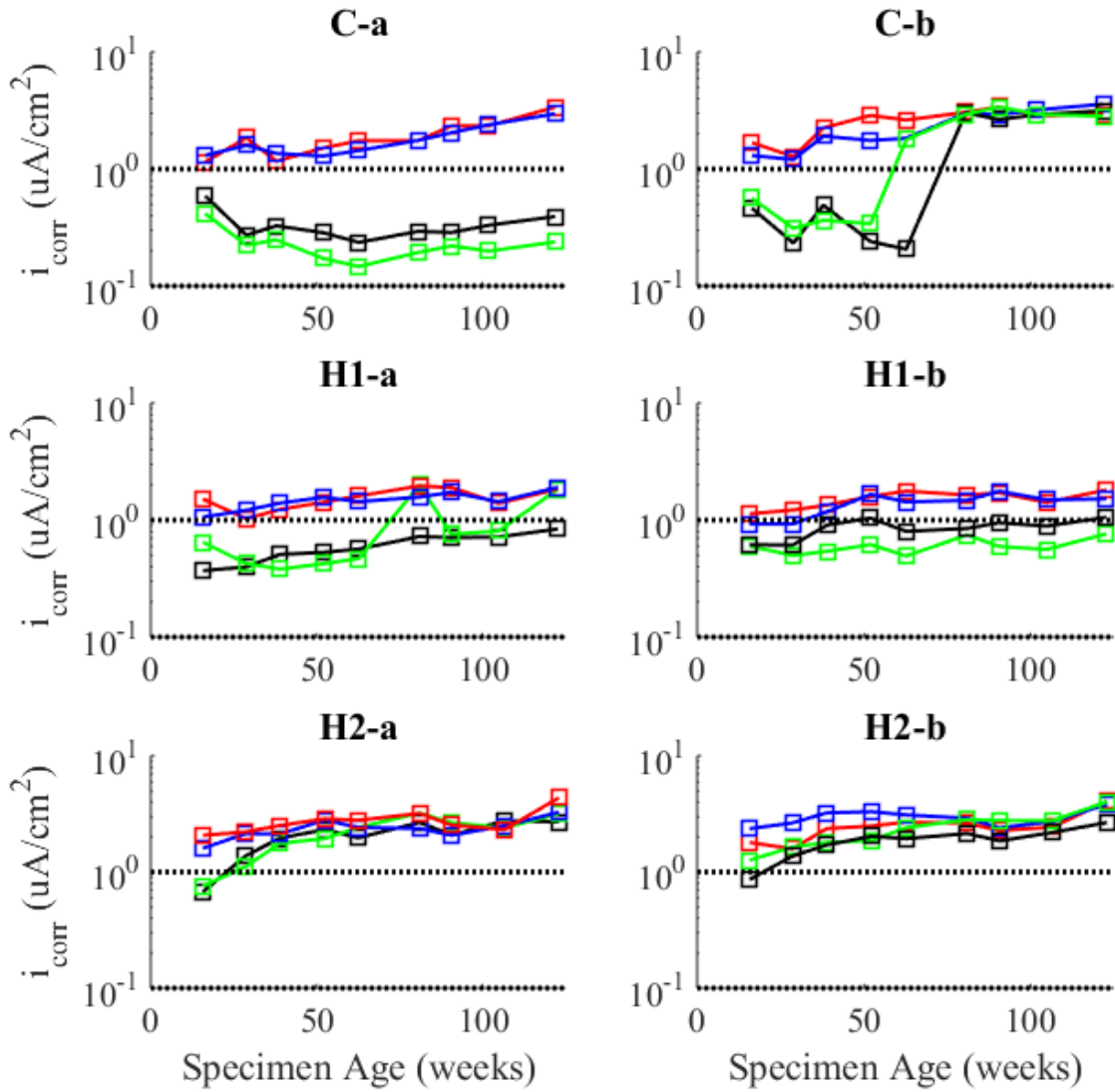|	A - Top Surface	B- Lateral Surface	C - Bottom Surface	D- Lateral Surface
C-a				
C-b				
H1-a				

A-2: Corrosion Behavior of Individual Rebars

Blue and red lines represent bars at 'top' surface, black and green lines represent bars at 'bottom' surface.
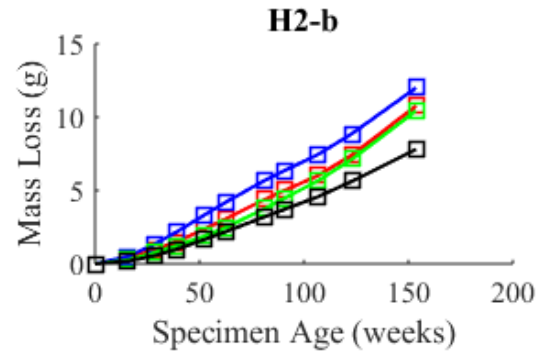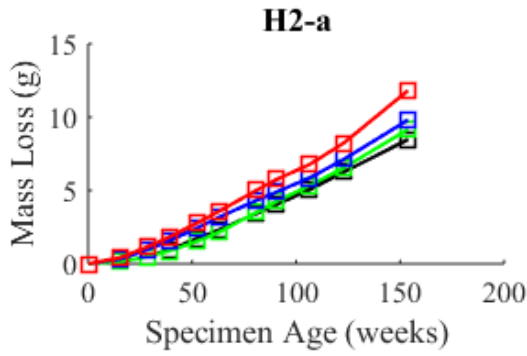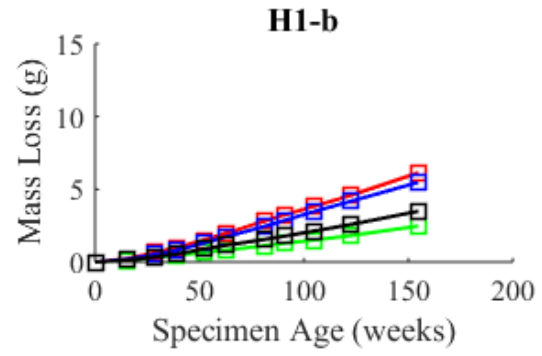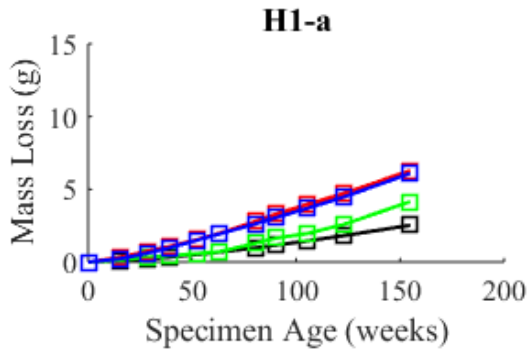
Corrosion Potential
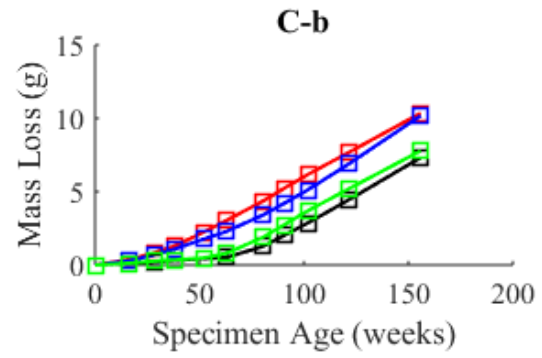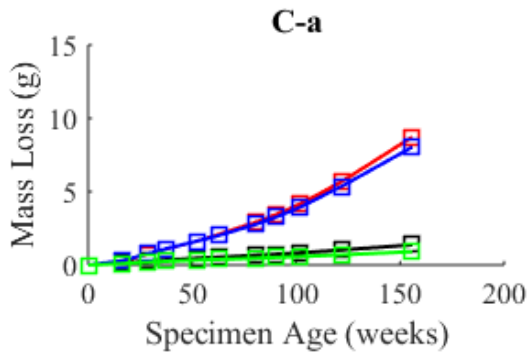
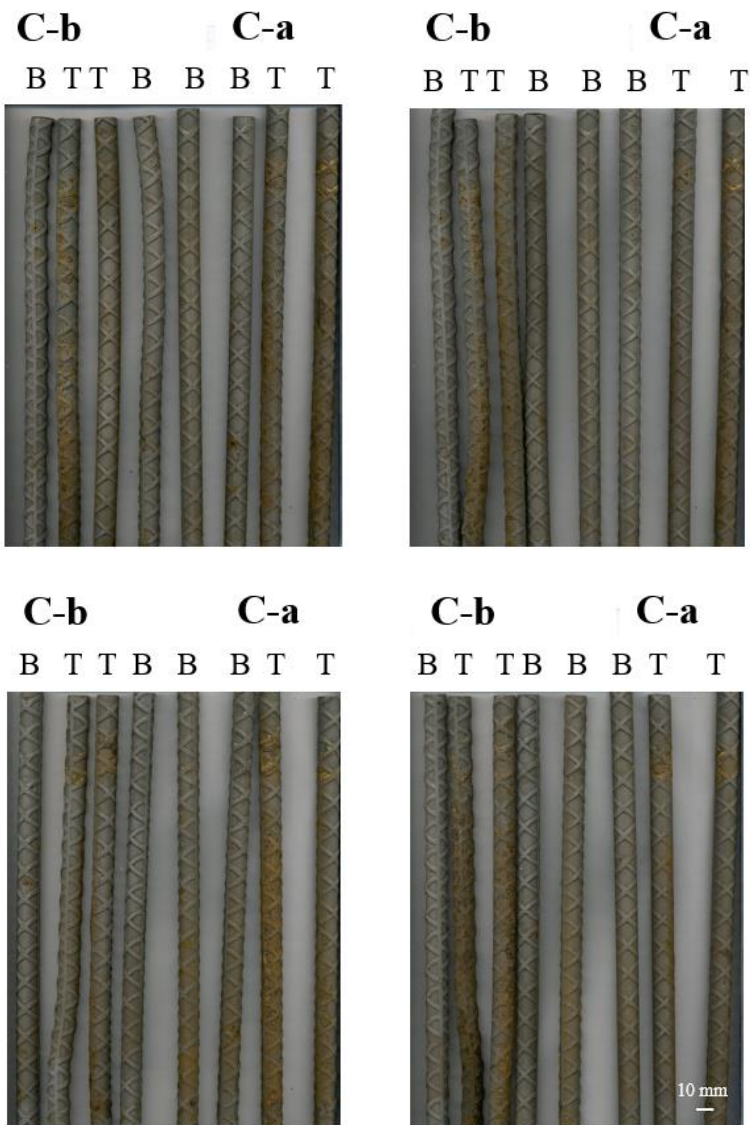**A-3: Scans of Individual Rebars**
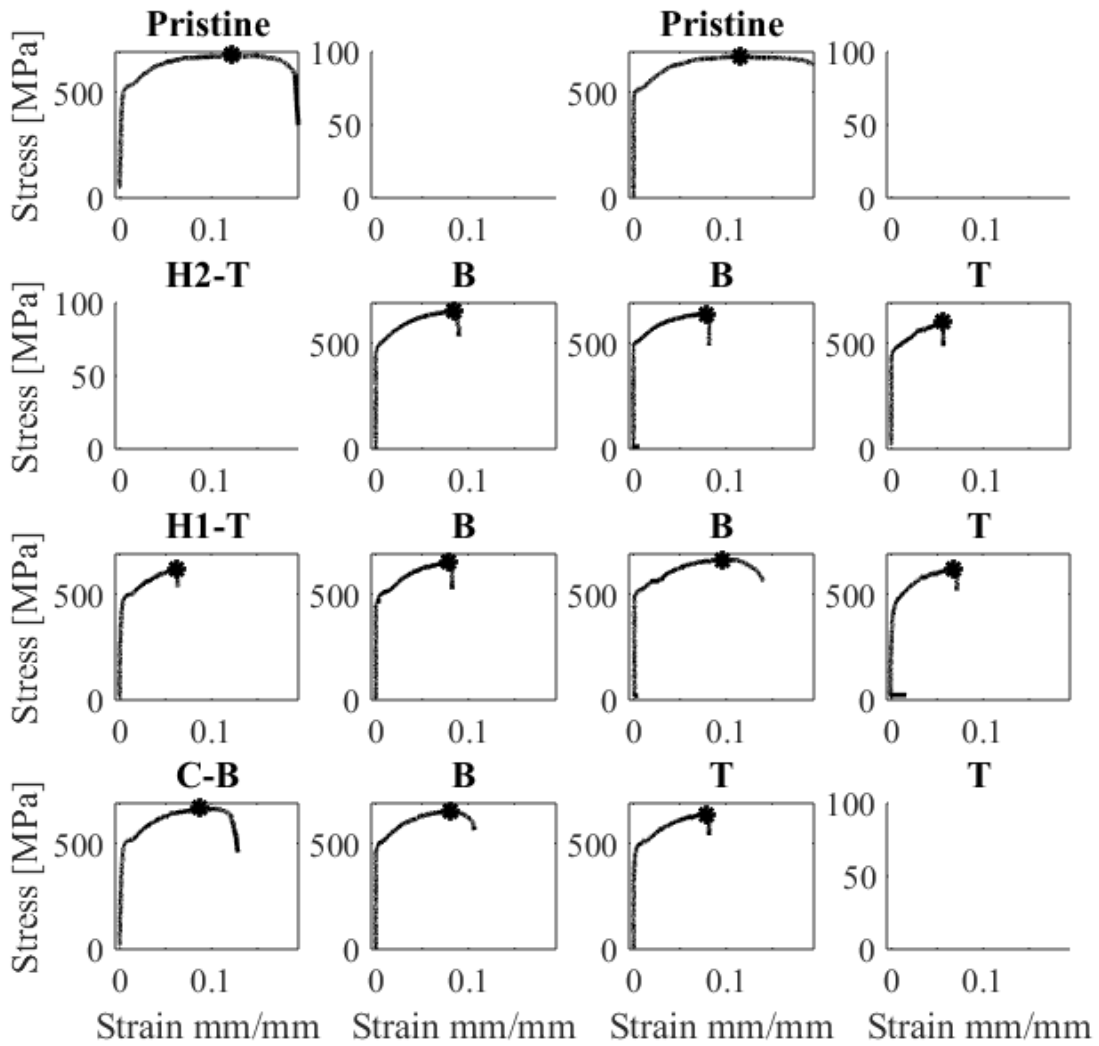
T – 'Top' Bar
B – 'Bottom' Bar
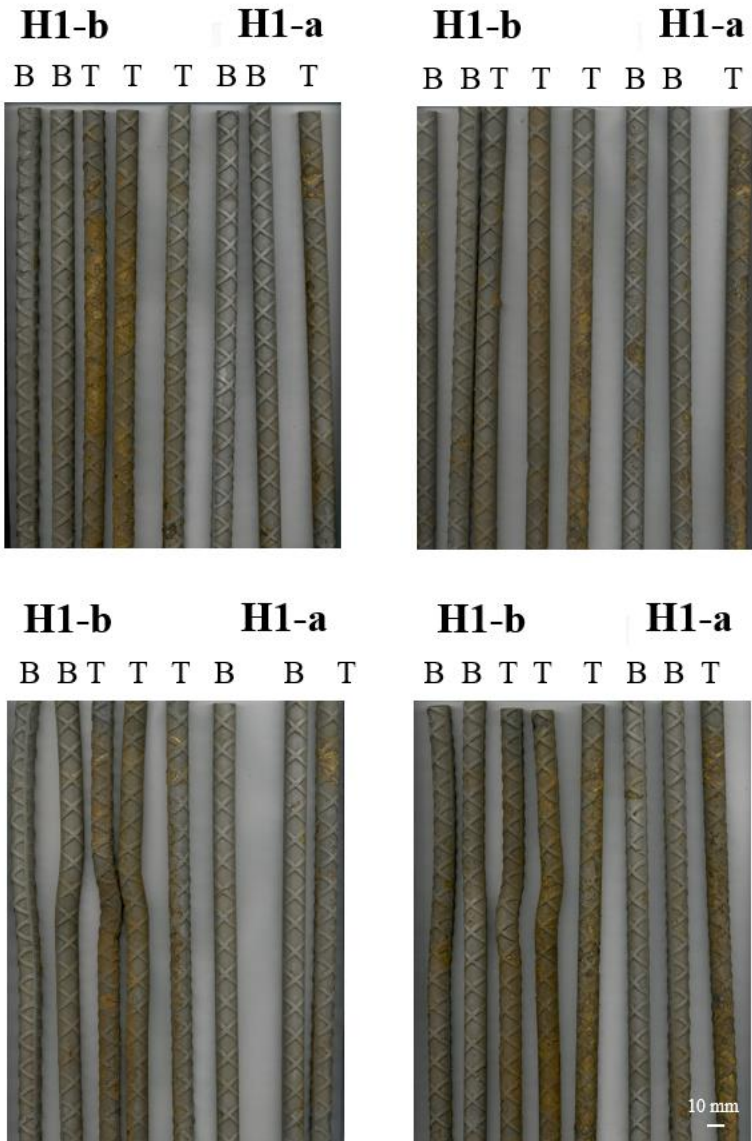
C Specimens

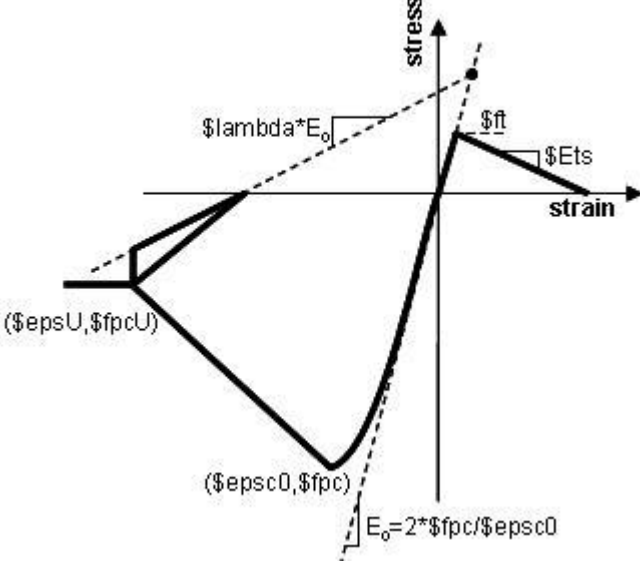**A-4: Tensile Testing Data of Individual Rebars**

Appendix B

B-1: Select Properties of Bridge Prototype (Sourced from Kaviani 2010)

Parameters	Value/ Description
General bridge description	Ordinary standard single-column bent bridge with 2 spans
Total length of bridge (L_{Total})	220.4 ft (67.2 m)
Number of spans and length of each deck span	2 spans: 108.58 ft (33.105 m) and 111.82 ft (34.095 m)
Total deck width (W_{deck})	27.13 ft (8.27 m)
Deck depth (d_d)	4.64 ft (1.415 m)
Deck cross-sectional geometry	A= 97.546 ft^2 (9.067 m^2); J= 341.442 ft^4 (2.954 m^4); I_x= 180.328 ft^4 (1.558 m^4); I_y= 3797.9 ft^4 (32.81 m^4); A_{vx}= 18.92 ft^2 (1.759 m^2); A_{vy}= 27.584 ft^4 (2.564 m^2); S_x= 83.35 ft^3 (2.362 m^3); Z_x= 115.143 ft^3 (3.263 m^3); S_y= 279.97 ft^3 (7.934 m^3); Z_y= 521.832 ft^3 (14.788 m^3)
Number and clear height of each column bent (H_{col})	1 column: 19.68 ft (6 m)
Column diameter (D_c)	5.51 ft (1.68 m)
Deck centroid ($D_{c.g.}$)	2.48 ft (0.756 m)
Length of cap beam to centrioid of column bent (L_{cap})	-------------
Cap beam dimension ($B_{cap}xd_d$)	------------
Location and size of expansion joints	No expansion joints specified
Support details for boundary conditions	Fixed foundations
Concrete material properties for concrete of superstructure (f'_c, E_c)	Elastic deck: f'_c= 5 ksi (34.5 MPa); E_c=4030.5 ksi (27.8E3 MPa)
Concrete and reinforcing material properties of column bents	Concrete: f'_c= 5 ksi (34.5 MPa); Steel: ASTM A706.
Reinforcement details of column bent cross section	Longitudinal reinforcement: 44#11 (bundles of 2), ρ_l=2% Transverse reinforcement: Spiral. #6 @3.34"
Abutment general geometry	Simplified abutment model
Number and properties of abutment bearing pads	4 elastomeric bearing pads used per abutment

B-2: Material Properties of Bridge Column Model (Sourced from Kaviani 2010).

Concrete Properties

	Cover Material	Core Material
 Concrete02 Material Model	fpc: -34.5 MPa epsc0 -0.0028 fpcU 0 epsU -0.005 lambda 0.1 ft 3.45 MPa Ets -1725	fpc -44.8 MPa epsc0 -0.0036 fpcU -41.4 MPa epsU -0.025 lambda 0.1 ft 4.48 MPa Ets -2248

(Image sourced from http://opensees.berkeley.edu/wiki/index.php/Concrete02_Material_--_Linear_Tension_Softening on 08/15/2019)

Reinforcing Steel Properties

Steel02

Fy   469 MPa
Es   200 GPa
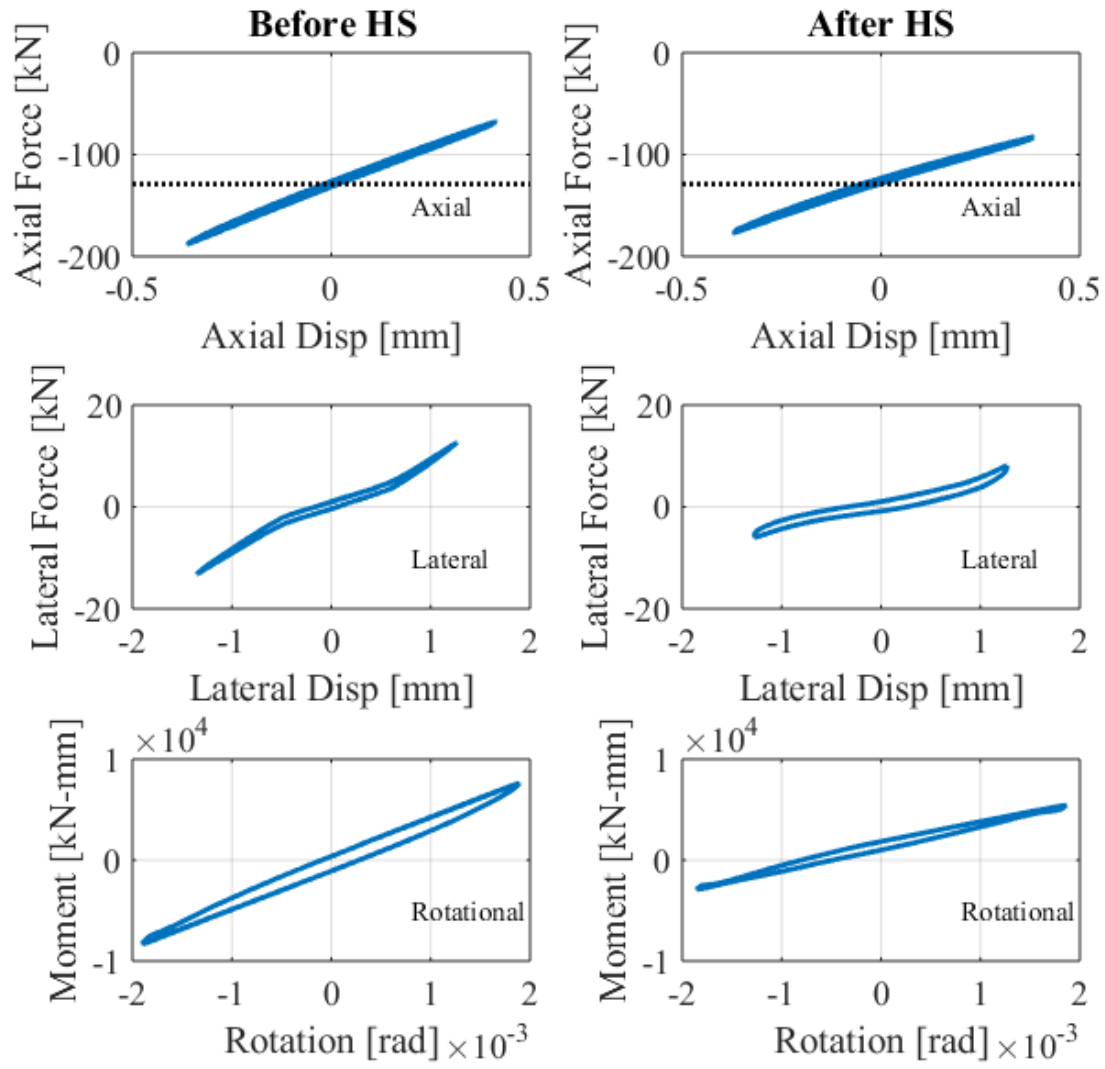Bs   0.01
R0   18.0
cR1 0.925
cR2 0.15

Appendix C

C-1 Mix Design for UHPFRC Endcaps

Mix proportions for UHPFRC endcap materials [per 1 m³].

	UHPFRC
Cement [kg]	862
Fly Ash Class F [kg]	84
Undensified Silica Fume [kg]	121
Coarse aggregate [kg]	412
Fine aggregate [kg]	619
Batched water [kg]	235
PVA fibers [vol. %]	0.5
Super-plasticizer [fl oz/cwt]	15
Water-binder ratio	0.22
f'_c [MPa]	84

C-2 Stiffness Determination Plots

C-u

C-c